Opto-electrical simulations of perovskite/c-Si tandem solar cells

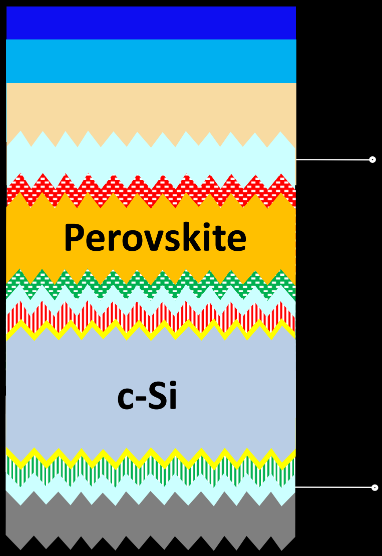

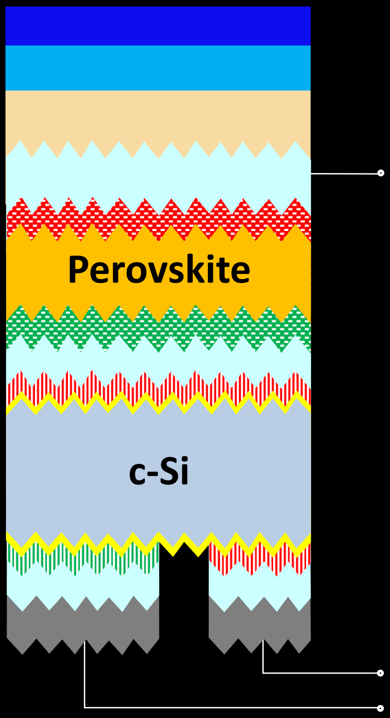

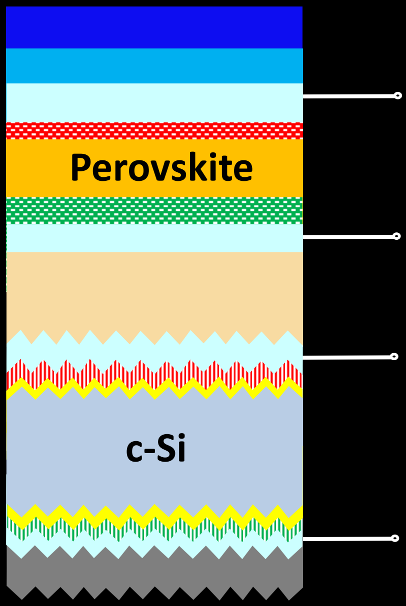

Indra Syifai

TU Delft Delft University of Technology

Master of Science Thesis

Opto-electrical simulations of perovskite/c-Si tandem solar cells

by

Indra Syifai

In partial fulfilment of the requirements for the degree of

Master of Science
In Sustainable Energy Technology

at the Delft University of Technology
to be defended publicly on November 05th, 2020 at 14:00 PM.

Student number:	4779150		
Project duration:	February 24th, 2020 – November 05th,2020		
Thesis committee	Dr.ir. Olindo Isabella	TU Delft, ESE - PVMD	Head of PVMD Group, Main supervisor
	Dr. ir. Rudi Santbergen	TU Delft, ESE - PVMD	Supervisor
	Dr. Paul A. Procel Moya	TU Delft, ESE - PVMD	Daily supervisor
	Manvika Singh	TU Delft, ESE - PVMD	Daily supervisor
	Dr. S. W. H. Eijt	TU Delft, TNW - RID	External committee member

TU Delft Delft University of Technology

lpdp lembaga pengelola dana pendidikan

Abstract

Due to the high-efficiency potential over 40%, the two-terminal (2T) perovskite/c-Si tandem solar cell becomes a desirable and promising candidate for solar cells. The photovoltaic materials and devices (PVMD) group in TU Delft has developed the c-Si solar cell using poly-SiO$_x$ as carrier-selective passivating contacts. The utilization of poly-SiO$_x$ as carrier selective passivating contacts is relatively new and very interesting to be analyzed as its bandgap can be varied by changing its oxygen content. This can be used in the solar cell to increase the *Jsc*.

In this work, the 2T perovskite/c-Si tandem solar cells' optimization has been conducted by means of optical and electrical simulations. Optical simulations of the 2T, 3T and 4T perovskite/c-Si tandem solar cells in GenPro4 are presented. The main objective is to show the new type of bottom cell's optical performance in the 2T, 3T, and 4T tandem solar cell. Furthermore, the two-terminal (2T) perovskite/c-Si tandem solar cell's electrical modeling framework with the new type of the bottom cell has been developed. In this model, the optical generation profile from GenPro4 was successfully imported into the semiconductor simulations software called Sentaurus TCAD. The perovskite and c-Si solar cells have been optimized separately. The perovskite solar cell optimization was conducted by changing parameters such as contact resistance, surface recombination velocity and thickness of each layer. This leads to the increase in the perovskite solar cell efficiency from 15.83% to 21.50%. This top cell was combined with a c-Si bottom cell with an efficiency of 25% to form a two-terminal (2T) tandem solar cell. The two-terminal (2T) perovskite/c-Si was further optimized by optimizing the tunnel recombination junction. The optimization of TRJ was done by varying the doping concentration of indium tin oxide (ITO) and spiro-OMeTAD, respectively. As a result, the 33.70% efficiency of the two-terminal (2T) perovskite/c-Si tandem solar cell was obtained.

Keywords: 2T perovskite/c-Si tandem solar cell, carrier-selective passivating contacts, GenPro4, Sentaurus TCAD, opto-electrical modelling framework, contact resistance, surface recombination velocity, thickness optimization, tunnel recombination junction.

Acknowledgment

Praise due to Allah SWT, the Almighty, for all his graces so that I can continue my Master's education at one of the best engineering universities in the world, TU Delft.

I would like to express my deepest gratitude to Dr. Olindo Isabella as the main supervisor. Thank you for your guidance and meaningful feedback. Thank you for letting me join the PVMD group. I met a lot of great people in this group. I got a lot of knowledge in photovoltaics, especially about tandem solar cells. My deepest and sincere gratitude also I give to my supervisor, Dr. ir. Rudi Santbergen and Dr. Paul A. Procel Moya. Thank you so much for your time, guidance, patience, knowledge that has been spent while guiding me. I am really thankful to meet great people like you. Nine months of working on this thesis is still not enough to absorb your knowledge. My deepest appreciation also goes to Manvika Singh as my daily supervisor. I am very fortunate to be a student of your guidance. Thank you very much for all the time, energy, knowledge that has been shared with me. I will definitely miss the discussions we have had so far. I hope you are successful in completing your Ph.D.

My greatest appreciation also give to the LPDP as my scholarship funder. Thank you for fulfilling my dream of studying at TU Delft. I would like to thank PT. Wijaya Karya (Persero) Tbk and the power plant and energy department which have always supported and allowed me to continue my master's education.

Mom and dad, thank you for all the warmth that has been given. I dedicate this to you. My shalihah, kind-hearted woman, Firas Sabila Nurdini. Thank you for always accompanying me. I love you. Fakhri, my younger brother, thank you for looking after mom and dad while I'm away. Chase your dream! You can do it!

I would like to also express my thanks to all families in Tuwel, Lampung and Cirebon. Mother and father-in-law, thank you for all your support. Hopefully, the knowledge that I got can be useful for people in my country, Indonesia.
Man jadda wa jada!

Indra Syifai
November, 2020

Contents

Contents

Abstract ..... **iii**
Acknowledgement ..... **iv**
List of Figures ..... **vii**
List of Tables ..... **ix**
List of Symbols ..... **x**
List of Abbreviations ..... **xii**

1. Introduction **13**
- 1.1. Background 13
- 1.2. Tandem solar cell 14
  - 1.2.1. Advantages of the tandem solar cell over the single-junction solar cell 14
  - 1.2.2. Types of the tandem based on the number of terminal connection 14
- 1.3. Semiconductor materials 17
  - 1.3.1. Crystalline silicon (c-Si) 17
  - 1.3.2. Perovskite 17
- 1.4. Silicon heterojunction (SHJ) 19
- 1.5. Present status of the 2T, 3T and 4T perovskite/c-Si tandem solar cells 19
- 1.6. Carrier selective passivating contacts 21
  - 1.6.1. Carrier selective contacts 21
  - 1.6.2. Surface passivation 21
- 1.7. Tunnel recombination junction 23
  - 1.7.1. The example of tunnel recombination junction 24
  - 1.7.2. The Fermi energy 25
- 1.8. Carrier transport phenomena 25
  - 1.8.1. Drift 25
  - 1.8.2. Diffusion 26
- 1.9. Carrier generation and recombination 26
  - 1.9.1. Direct recombination 26
  - 1.9.2. Shockley-Read-Hall recombination 27
  - 1.9.3. Auger recombination 28
  - 1.9.4. Surface recombination 28
- 1.10. Simulation software 29
  - 1.10.1. Optical simulation using GenPro4 29
  - 1.10.2. Electrical simulations 30
- 1.11. Objective and research question 31
- 1.12. Outline 32

2. Optical Simulations **33**

2.1. Tandem Structure 33
    2.1.1. 2T perovskite/c-Si tandem solar cells structure 33
    2.1.2. 3T perovskite/c-Si tandem solar cells structure 34
    2.1.3. 4T perovskite/c-Si tandem solar cells structure 35
2.2. Input Parameters 36
2.3. Method 38
2.4. Results 38
    2.4.1. 2T perovskite/c-Si tandem solar cells 39
    2.4.2. 3T perovskite/c-Si tandem solar cells 41
    2.4.3. 4T perovskite/c-Si tandem solar cells 42
2.5. Discussion 43
2.6. Conclusion 45
3. Optimization of the perovskite solar cell 48
5.1. Introduction 48
3.2. Model and parameters 49
3.3. Comparison with experimental data 50
3.4. Optimized parameters 51
3.5. Result and discussion 51
    3.5.1. Contact resistance optimization 51
    3.5.2. Surface recombination velocity optimization 52
    3.5.3. Thickness optimization 52
3.6. Conclusion 58
4. Optimization of the tunnel recombination junction 60
4.1. Summary of the perovskite and c-Si after optimization 60
4.2. Modelling framework of the 2T perovskite/c-Si tandem solar cells 60
4.3. The result of 2T tandem (before optimizing the TRJ) 61
4.4. Optimization parameters 62
4.5. Results and discussions 62
    4.5.1. Optimization the TRJ by changing the TCO doping 63
    4.5.2. Optimization the TRJ by changing the HTL doping 65
    4.5.3. 2T perovskite/c-Si tandem output 66
4.6. Conclusions 66
5. Conclusions and Outlook 67
5.1. Conclusions 67
5.2. Outlook 68
References 69

List of Figures

Figure 1. 1. Energy resources of the world. Adapted from [3]. 13
Figure 1. 2. Two-terminal (2T) monolithic stack. Adapted from [10]. 15
Figure 1. 3. Two-terminal (2T) mechanically-stacked. Adapted from [10]. 15
Figure 1. 4. Three-terminal (3T) tandem solar cell. Adapted from [14]. 15
Figure 1. 5. Four-terminal (4T) mechanically-stacked. Adapted from [16]. 16
Figure 1. 6. Silicon heterojunction solar cell structure. Adapted from [32]. 19
Figure 1. 7 (a). The GaAsPN/Si tandem solar cells structure, (b) Simulated band diagram of GaP (n)/Si (p) tunnel junctions. Adapted from [53]. 24
Figure 1. 8. The difference between the local and non-local tunneling models. Adapted from [54]. 24
Figure 1. 9. Auger recombination illustration with (a) two electrons; and (b) two holes. Adapted from [56]. 28
Figure 1. 10. Dangling bonds on c-Si surface. Adapted from [7] 29
Figure 1. 11. Device simulation process flow using Sentaurus Device. Adapted from [55]. 31

Figure 2. 1. The 2T perovskite/c-Si tandem solar cells structure. (a) Non encapsulated, (b) Encapsulated by glass and EVA. 34
Figure 2. 2. The 3T perovskite/c-Si tandem solar cells structure. (a) Non encapsulated, (b) Encapsulated by glass and EVA. 35
Figure 2. 3. The 4T perovskite/c-Si tandem solar cells structure encapsulated by glass 36
Figure 2. 4. Optical properties used for the top cells. (a) refractive index n, (b) extinction coefficient k. 36
Figure 2. 5. Optical properties of the bottom cells used. (a) refractive index n, (b) extinction coefficient k. 37
Figure 2. 6. Absorptance and reflectance of current matched 2T perovskite/c-Si tandem solar cells using poly-SiO$_x$ as CSPCs. (a). before thickness optimization, (b) after thickness optimization and (c) encapsulated by glass. 39
Figure 2.7. Absorptance and reflectance of current matched 3T perovskite/c-Si tandem solar cells using poly-SiO$_x$ as CSPCs. (a). before thickness optimization, (b) after thickness optimization and (c) encapsulated by the glass. 41
Figure 2. 8. Absorptance and reflectance of current matched 4T perovskite/c-Si tandem solar cells using poly-SiO$_x$ as CSPCs. 43
Figure 2.9. The J_{PH} (mA/cm^2) of fully textured 2T and 3T perovskite/c-Si tandem solar cells before thickness optimization. 43
Figure 2.10. The J_{PH} (mA/cm^2) of fully textured 2T and 3T perovskite/c-Si tandem solar cells after thickness optimization. 44
Figure 2.11. The J_{PH} (mA/cm^2) of 2T, 3T and 4T perovskite/c-Si tandem solar cells after encapsulated by glass. 45

Figure 3.1. Optimization process flow of 2T perovskite/c-Si tandem solar cell 48
Figure 3.2 Simulated structure of the top cell. 49
Figure 3.3. The comparison of experimental J-V with simulated J-V 50
Figure 3.4. The effect of contact resistance on fill factor by varying the front and back contact resistance using the same value. 51
Figure 3. 5. The effect of surface recombination velocity on (a) J_{SC} (mA/cm^2), (b) V_{OC} (V), (c) FF (%) and (d) H (%) 52
Figure 3. 6. The effect of perovskite thickness on J_{PH} (mA/cm^2), JSC (mA/cm^2) and $J_{\text{TOTAL RECOMBINATION}}$ (mA/cm^2). 53
Figure 3. 7. The influence of perovskite thickness on recombination current densities. 54
Figure 3. 8. The effect of perovskite thickness on (a) V_{OC} (V), and (b) FF (%) 55
Figure 3. 9. The effect of FTO thickness on (a) J_{SC} (mA/cm^2), (b) V_{OC} (V), (c) FF (%) and (d) H (%) 56
Figure 3. 10. The effect of ETL thickness on (a) J_{SC} (mA/cm^2), (b) V_{OC} (V), (c) FF (%) and (d) H (%) 57

Figure 3. 11. The effect of HTL thickness on (a) J_{sc} (mA/cm^2), (b) V_{oc} (V), (c) FF (%) and (d) H (%) 58
Figure 3. 12. Summary of the parameters of the top cell before optimization and after optimization 58

Figure 4. 1. Simulation steps of the 2T perovskite/c-Si tandem solar cells 61
Figure 4. 2 (a) Band diagram of the 2T perovskite/c-Si tandem solar cells before optimizing the TRJ; (b) A closer view of the TRJ area 62
Figure 4. 3. Effect of the TCO doping to the PV parameters; (a) on J_{sc}, (b), on V_{oc}, (c) on *FF* and (d) on H 63
Figure 4. 4. (a) Band diagram of the 2T perovskite/c-Si tandem with TCO doping concentration of 9.10^{19} cm^{-3}; (b) Showing perfect band alignment between E_{FN} and E_{FP}... 64
Figure 4.5. Band diagram of the 2T perovskite/c-Si tandem with TCO doping concentration of 9E20 cm^{-3}; (b) Showing misalignment indicated by purple arrow 64
Figure 4. 6. Effect of the HTL doping to the PV parameters; (a) on J_{sc}, (b), on V_{oc}, (c) on *FF* and (d) on H 65
Figure 4. 7. The J-V curves and optimum output parameters of the 2T perovskite/c-Si 66

List of Tables

TABLE 1. 1. THE POWER POTENTIAL OF EACH ENERGY TECHNOLOGY AND THE CURRENT POWER DELIVERED AS ELECTRICITY.14
TABLE 1. 2. PROS AND CONS OF 2T, 3T AND 4T TANDEM SOLAR CELL, REF [10] [15]. 16
TABLE 1. 3. (A) A PORTION OF THE PERIODIC TABLE; (B) A LIST OF SOME SEMICONDUCTOR MATERIALS. ADAPTED FROM [17]. 17
TABLE 1. 4. SUMMARY OF THE PRESENT STATUS OF THE 2T, 3T AND 4T PEROVSKITE/C-SI TANDEM SOLAR CELLS [34] [35] [36]. 19

TABLE 2. 1. THE LAYER THICKNESSES OF THE TANDEM SOLAR CELLS. 38
TABLE 2. 2. THE DESCRIPTION OF THE ABSORPTANCE VS WAVELENGTH GRAPH 39
TABLE 2. 3. THE SUMMARY OF OPTICAL SIMULATIONS OF 2T AND 3T PEROVSKITE/C-SI TANDEM SOLAR CELLS BEFORE THICKNESS OPTIMIZATION. 46
TABLE 2. 4. THE SUMMARY OF OPTICAL SIMULATIONS OF 2T AND 3T PEROVSKITE/C-SI TANDEM SOLAR CELLS AFTER THICKNESS OPTIMIZATION. 46
TABLE 2. 5. THE SUMMARY OF OPTICAL SIMULATIONS OF 2T, 3T AND 4T PEROVSKITE/C-SI TANDEM SOLAR CELLS AFTER THICKNESS OPTIMIZATION AND ENCAPSULATION. 46

TABLE 3.1. SIMULATION PARAMETERS OF THE TOP CELL [67] 49
TABLE 3. 2. SUMMARY OF THE PHYSICS MODELS USED FOR ELECTRICAL SIMULATIONS 50
TABLE 3.3. THE COMPARISON OF TOP CELL PERFORMANCE PARAMETERS FROM THE EXPERIMENT [67] AND SIMULATIONS 50

TABLE 4. 1. THE OUTPUT PARAMETERS OF THE OPTIMIZED PEROVSKITE AND C-SI 60
TABLE 4. 2. SIMULATION PARAMETERS OF THE 2T PEROVSKITE/C-SI TANDEM SOLAR CELLS 61
TABLE 4. 3. THE OUTPUT PARAMETERS OF THE 2T TANDEM BEFORE OPTIMIZING THE TRJ 61
TABLE 4. 4. SUMMARY OF THE OPTIMUM DOPING CONCENTRATION OF THE TCO AND HTL 66

List of Symbols

Latin Symbols

c_d	Direct recombination coefficient
c_n	Electron capture coefficient
D_n	Electron diffusion coefficient
D_p	Hole diffusion coefficient
E_f	Fermi energy
E_{fn}	Quasi Fermi energy of electrons
E_{fp}	Quasi Fermi energy of holes
FF	Fill factor
h	Planck constant
J	Current density
J_{Auger}	Auger recombination current density
$J_{diffusion}$	Total diffusion current density
J_{drift}	Total drift current density
J_o	Saturation current density
J_{ph}	Implied photo-current density
$J_{radiative}$	Radiative recombination current density
J_{sc}	Short circuit current density
J_{SRH}	SRH recombination current density
K_B	Boltzmann constant
m_n^*	Effective mass of the electrons

m_p^*	Effective mass of the holes
n	Electron density
n	Refractive index (real part)
N_c	Conduction band densities
n_i	Intrinsic carrier concentrations
NsT	Surface trap density,
Nt	Trap density
N_v	Valence band densities
p	Hole density, cm^{-3}
p_o	Equilibrium hole concentration
p_s	Hole concentration at the surface
q	Elementary charge
R_{Aug}	Auger recombination rate
R_d	Direct recombination
R_{SRH}	Shockley-Read-Hall recombination rate
S_r	Surface recombination velocity
T	Temperature
v_{dn}	Average drift velocities for electrons
v_{dp}	Average drift velocities for holes
V_{oc}	Open circuit voltage
v_{th}	Thermal velocity

Greek Symbols

ξ	Electric field
μ_n	Electron mobility
μ_p	Hole mobility
∇_n	Electron density gradient
∇_n	Hole density gradient
Δn	Excess carrier of electron
Δp	Excess carrier of hole
σ_p	Capture cross-section for holes
σ_n	Capture cross-section for electrons
η	Efficiency
κ	Refractive index (imaginary part)
ϵ	Relative Permitivity
ϵ_0	Relative Permitivity in vacuo
λ	Wavelength
χ	Electron affinity

List of Abbreviations

TCO	Transparent Conductive Oxide
IBC	Interdigitated Back Contact
CVD	Chemical Vapor Deposition
PCE	Power Conversion Efficiency
SHJ	Silicon Heterojunction
PVD	Physical Vapor Deposition
FSF	Front Surface Field
BSF	Back Surface Field
CSPCs	Carrier-Selective Passivating Contacts
EQE	External Quantum Efficiency
TRJ	Tunnel Recombination Junction
NLM	Non Local Mesh
TCAD	Technology Computer-Aided Design
SWB	Sentaurus Workbench
SDE	Sentaurus structure editor
EVA	Ethylene-Vinyl Acetate
ITO	Indium Tin Oxide
FTO	Fluorine-doped Tin Oxide
MPP	Maximum Power Point
ETL	Electron Transporting Layer
HTL	Hole Transporting Layer
SRV	Surface Recombination Velocity

1. Introduction

1.1. Background

Solar energy is one of the most promising renewable energy sources [1] [2]. It is very abundant [2] [3]. As can be seen in Figure 1. 1, the amount of energy our planet receives from the sun can meet more than 3000 times the current global energy needs [3]. Solar energy is also the cleanest renewable energy source, it does not produce greenhouse gas emissions like fossil fuels [1]. Solar energy can also be generated anywhere, as long as there is sunlight. This characteristic makes solar energy become easier to be installed in rural areas than other types of energy such as wind energy, coal, nuclear, etc. Solar energy also can give us a chance to become prosumer, so the people can consume, control and also sell the electricity back to the grid [4] [5]. The falling price of the solar panel is also expected to increase the use of solar energy in the world [6].

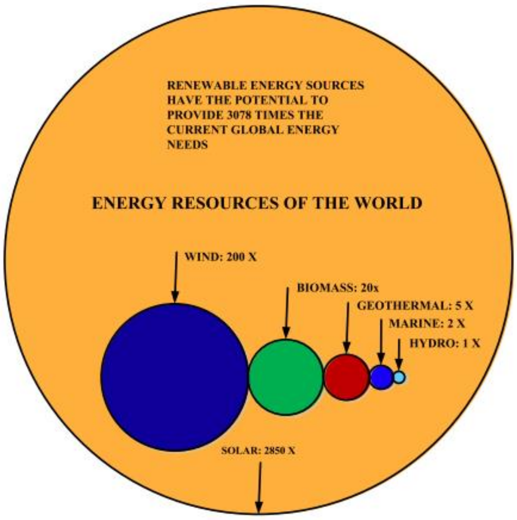

Figure 1. 1. Energy resources of the world. Adapted from [3].

Based on data in Table 1.1, the amount of energy that can potentially be produced from solar energy is very high, i.e., 56,940,000 TWh for solar PV and 40,296,000 TWh for concentrated solar power (CSP). Nevertheless, utilization is still very small [3]. Until 2020, the global electricity generation for solar PV is only 332 TWh or 0.00058% of the total solar energy potential, whereas for the CSP the utilization of this energy by 2020 is only 50 TWh or 0.00012%. The low utilization can be occurred because of many aspects, one of them is from the technological aspect. The device could not convert the solar energy into electricity optimally yet. Until now, the solar panels on the market have an average efficiency of 15-20%. That means, from the total solar energy received, 80-85% is still wasted. This losses 50% comes from spectral mismatch [7]. It contributes greatly to the losses because of the inability of the absorber to accommodate all incoming spectral, thus many models are continuously developed to increase the efficiency of solar cells, one of them is tandem configuration.

Table 1. 1. The power potential of each energy technology and the current power delivered as electricity.

Energy Technology	Energy potential worldwide [8]	Global electricity generation in 2020 [3]	
	TWh	TWh	%
Hydro	16,644	4,513	27.11
Wind	14,892,000	1,272	0.0085
Geothermal	394,200	131	0.0332
Solar PV	56,940,000	332	0.00058
Concentrating solar power	40,296,000	50	0.00012

1.2. Tandem solar cell

Tandem solar cell is the type of solar cell that combines two absorbers with different energy bandgaps in one stack [9]. This technique is one of the ways to increase the efficiency of solar cells. The basic principle of tandem solar cells is optimizing the spectrum by splitting the spectrum and placing an absorber that works optimally in the range of that spectrum [9]. Absorber with higher bandgap energy will occupy the top layer, and absorb the high energy photons [10]. The bottom cell with lower bandgap energy will absorb the low energy photons [10]. This configuration allows a larger portion of the light energy to be converted into electricity by reducing thermalization losses.

1.2.1. Advantages of the tandem solar cell over the single-junction solar cell

The single-junction solar cell is the most widely used solar-cell type on the market today. Recently, silicon and GaAs as the common absorber material, have achieved an efficiency record of 26.7% and 28.9%. Based on the Shockley-Queisser limit, this value has approached the maximum efficiency value for a single-junction solar cell, which is 33.16% for an absorber with a bandgap of 1.34 eV or 29.4% for solar cells with silicon as the absorber [11][[12]].

Therefore, another method is needed to maximize the use of solar energy. Tandem solar cell is the answer to overcome the barrier efficiency of a single junction. By combining several semiconductor materials with different energy bandgap, it allows the utilization of solar energy optimally.

1.2.2. Types of the tandem based on the number of terminal connection

Based on the number of terminal connections, tandem solar cells are divided into 3 types i.e. two-terminal (2T) tandem solar cell, three-terminal (3T) tandem solar cell and four-terminal (4T) tandem solar cell [10].

Two-terminal (2T) tandem solar cell

Based on the number of the transparent conductive oxide (TCO) two-terminal (2T) tandem solar cells can be divided into two forms, i.e. two-terminal (2T) monolithic stack and two-terminal (2T) mechanically-stacked [10].

Two-terminal (2T) monolithic stack

Two absorbers are monolithically stacked on top of another with a single transparent conductive layer [10]. The recombination or tunneling layer is formed between the two absorbers. This tandem is the most attractive and has been widely used in the market because of the ease of fabrication and its commercial viability [10]. The only disadvantage is the current matching issue i.e. the performance of the tandem solar cell is limited by the absorber with the lowest current [10] [13].

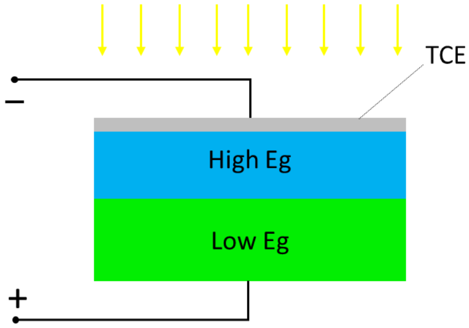

Figure 1. 2. Two-terminal (2T) monolithic stack. Adapted from [10].

Two-terminal (2T) mechanically-stacked

The device consists of two absorbers stacked separately but they are serially connected with the two terminal outputs [10]. The transparent conductive layer is also placed on the top and bottom cells. This type has some advantages such as does not require interfacial tunneling and also the current matching [10]. Nevertheless, as can be seen in Figure 1. 3, this configuration needs extra TCO layers which leads to strenuous optical losses [10].

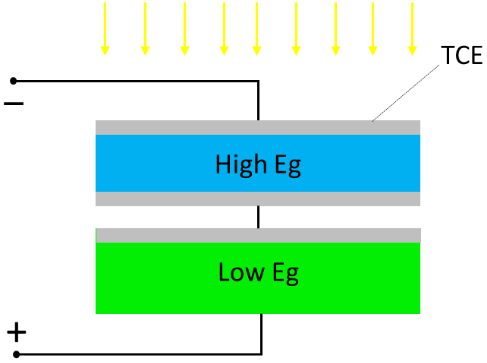

Figure 1. 3. Two-terminal (2T) mechanically-stacked. Adapted from [10].

Three-terminal (3T) tandem solar cell

3T tandem solar cell structure is quite similar with the 2T tandem. The main difference is the use of the interdigitated back contact (IBC) cell as the bottom cell structure. The 3T tandem configuration are shown in Figure 1. 4 below.

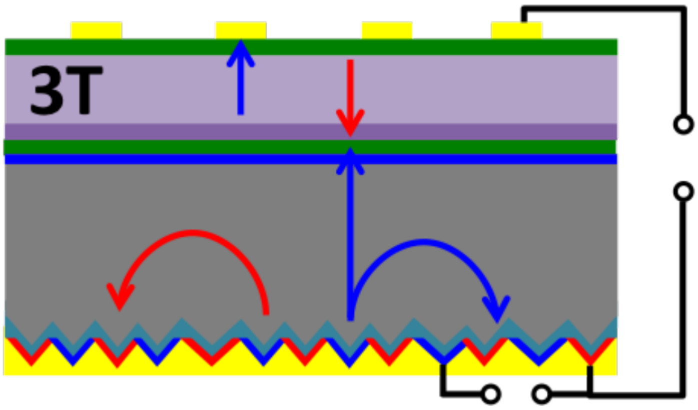

Figure 1. 4. Three-terminal (3T) tandem solar cell. Adapted from [14].

The carrier extraction and collection process are quite similar to the 2T tandem. In the case of the *np-np* configuration, the holes from the top cell are recombined with the electron from the bottom cell. The electrons in the top cell are collected in the front contact, whereas the holes from the bottom cell are collected in the rear contact. The difference of the 3T is the ability to extract the excess current in the bottom cell using the second back contact of the IBC cell. It makes the device less sensitive to the current matching [14].

Four-terminal (4T) tandem solar cell

As can be seen from Figure 1. 5, each cell has two terminals so that the electrical output can be generated independently [15]. The top cell has to be semi-transparent type so it does not deter the transmission light to the bottom cell [10].

This 4T mechanically stacked configuration allows a significant increase in solar cell performance [10]. As can be seen in Figure 1. 5, the 4T tandem solar cell requires more complex substrates, layers, interconnection, and processing steps. Moreover, the use of many TCO layers also reduces the price competitiveness of this tandem. The TCO layer is the most critical component in the performance and manufacturing perspective. One TCO layer requires expensive costs through sputtering or CVD equipment. TCO layer creates an inherent trade-off between optical and series resistance losses which causes a decrease in the overall efficiency of the PV module by 10-25% [10].

Therefore, it is still very difficult to imagine the production of competitive large-scale modules using tandem 4T technology [10].

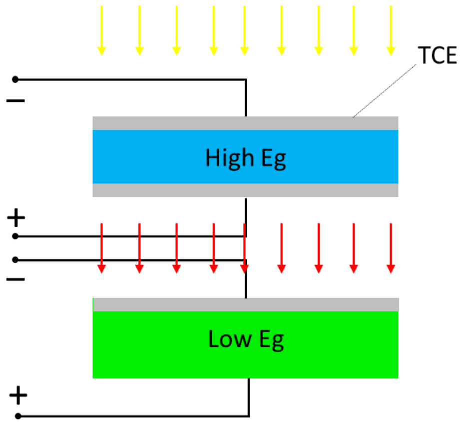

Figure 1. 5. Four-terminal (4T) mechanically-stacked. Adapted from [16].

The following is a summary of some advantages and disadvantages of each type of tandem solar cell.

Table 1. 2. Pros and cons of 2T, 3T and 4T tandem solar cell, ref [10] [15].

2T Tandem Solar Cells		3T Tandem Solar Cells		4T Tandem Solar Cells	
Pros	Cons	Pros	Cons	Pros	Cons
- At the optimum bandgap, 2T has the same performance with 4T	- Current matching condition	- The intermediate terminal adds another degree of freedom of electrical connection which relaxes the circuit from the current matching issue	- Until now, this model is more convenient for research purposes - The 3T configuration has the lowest maximum efficiency compared to the 2T and 4T configuration	- Each cells operates independently	- It is still impractical for large scale manufacturing - The processing steps are more complicated

1.3. Semiconductor materials

Semiconductors are a group of materials having conductivities between metals and insulators. Semiconductors can be classified into two types, i.e. the elemental semiconductor materials and the compound semiconductor materials. The elemental semiconductor materials are the materials belonging to group IV of the periodic table, whereas the compound semiconductor materials are the materials which formed mostly from the combinations of group III and group V elements of the periodic table [17].

Table 1. 3. (a) A portion of the periodic table; (b) A list of some semiconductor materials. Adapted from [17].

III	IV	V
5 **B** Boron	6 **C** Carbon	
13 **Al** Aluminum	14 **Si** Silicon	15 **P** Phosphorus
31 **Ga** Gallium	32 **Ge** Germanium	33 **As** Arsenic
49 **In** Indium		51 **Sb** Antimony

(a)

Elemental semiconductors	
Si	Silicon
Ge	Germanium
Compound semiconductors	
AlP	Aluminum phosphide
AlAs	Aluminum arsenide
GaP	Gallium phosphide
GaAs	Gallium arsenide
InP	Indium phosphide

(b)

Table 1. 3 (a) shows some elements of group III, group IV and group V in which the more common semiconductors are found. A more complex semiconductor made by the combination of Group III, group IV, group V, and another group elements is also possible such as perovskite structure ($CH_3NH_3Pb_{3-x}Cl_x$). Table 1. 3 (b) shows some examples of the elemental and compound semiconductors. The compound semiconductors can also be formed by more than two elements, for example, gallium indium phosphide (GaInP).

1.3.1. Crystalline silicon (c-Si)

Crystalline silicon is silicon in the crystalline form. It is being one of the most widely researched semiconductor materials for more than 30 years [18]. It also still dominant in the market share of PV technology which accounted for around 95% of the total production in 2019 [19]. It belongs to the first generation of solar cells, often referred to as conventional, traditional, or wafer-based solar cells [20]. Crystalline silicon has so many advantages such as abundance in nature (about 25% of the earth's crust is silicon) [18]. It is classified as a non-toxic material, so it is suitable for development of green technology. It can remain stable for 20 years [18]. Crystalline silicon is high energy efficiency [18]. At present, the highest efficiency of the single junction crystalline silicon solar cell has reached 26.7% with the theoretical limit of the efficiency being 29.4% [12].

1.3.2. Perovskite

In this section, a brief description of perovskite is shown. The background of using perovskite as the top cell for the 2T tandem solar cell that used for the simulation is also explained.

Perovskite is a natural mineral [21] [22]. It was first discovered as a calcium titanate compound (CaTiO3) by German mineralogist Gustav Rose in 1839 [20] [23] [24] [25]. The mineral was named perovskite as a tribute to the Russian mineralogist Lev Perovski (1792-1856) [21] [22]. Later on, the compounds with the same crystal structure as CaTiO3 are categorized into perovskite material. Perovskite is currently classified as an emerging thin-film technology, which means that this material is still under development and has not been commercialized yet [20].

Perovskite has so many advantages, including relatively earth-abundant, low-cost synthesis, lead-free, stable in thermodynamic, high PCE, high V_{oc}, J_{sc}, and *FF*, large cell area, defect tolerant, suitable bandgaps ≈ 1.5 eV, etc [26]. From the economic side, perovskite also can be produced at a low cost and in efficient way [22]. So, that is why perovskite becomes the most promising alternative material to be developed. Perovskite that is commonly used today, is $MAPBI_3$. In this project, another type of perovskite is introduced. $MAPBI_{3-x}Cl_x$ will be used as an absorber in the top cell. This material has several advantages compared to the perovskite material commonly used today ($MAPBI_3$), such as enhance device stability, better charge collection efficiency, and reproducibility [27] [28]. Besides, Cl in these structures plays an important role in improving film morphology and increasing grain boundaries of perovskite crystal, which enhances short-circuit current [28].

The following is a timeline of various types of solar cell perovskite from the first time it was published by Miyasaka et al. in 2009 with an efficiency of 3.8% until 2017, which was recorded to have achieved an efficiency of 22.1% by the Ulsan National Institute of Science and Technology (UNIST) [22]. It can be seen that the development of the efficiency graph is increasing. Moreover, in 2018, perovskite efficiency has reached 23.3% and is the highest efficiency for perovskite solar cells. Theoretically, perovskite can reach power conversion efficiency (PCE) up to 30% [29].

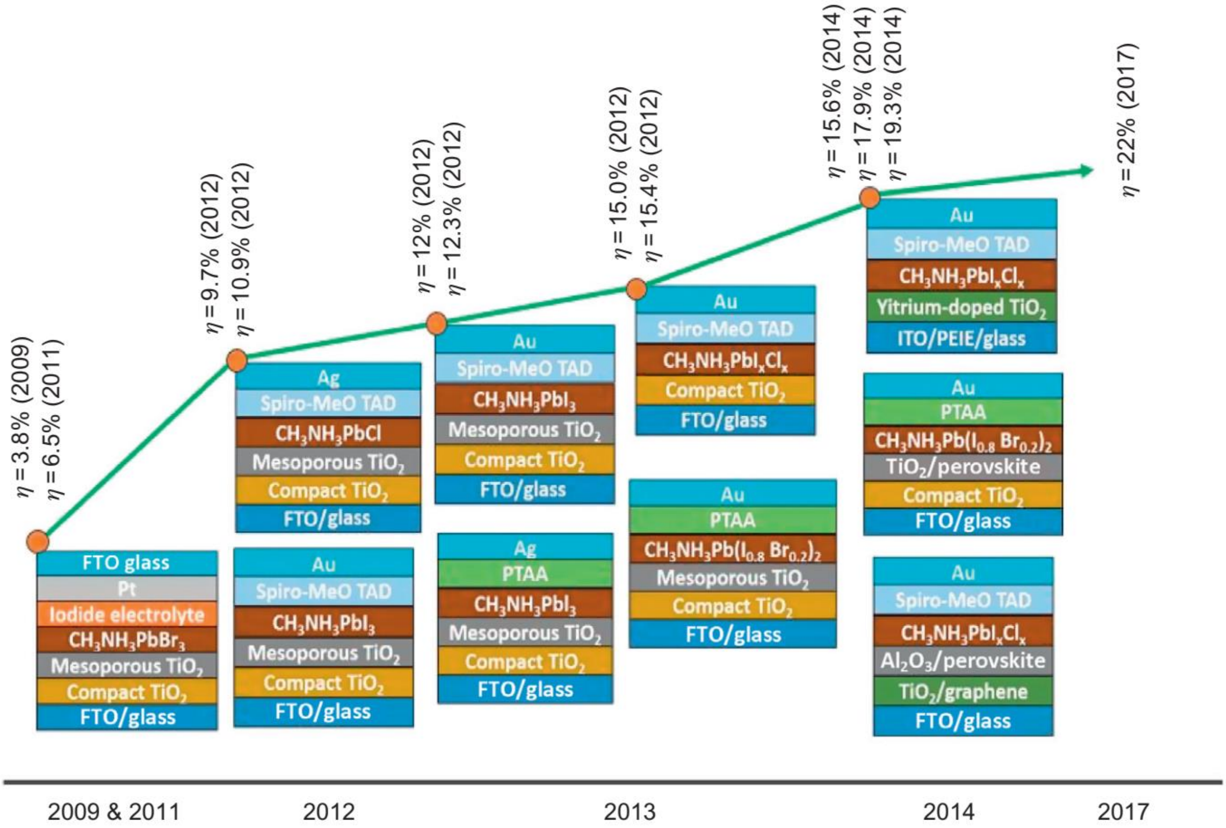

Figure 1.1. Timeline of various perovskite solar cells. Adapted from [22].

The main challenge for the perovskite now is the instability of the material [26]. It is still unstable when in contact with moisture [26]. This behavior makes a barrier to commercialization. To overcome this problem, future research should focus more on the following actions, i.e., enhancing the intrinsic stability of the perovskite absorber layer, proper geometry design, and finding durable coating material that protects the cell from moisture [25].

1.4. Silicon heterojunction (SHJ)

Silicon heterojunction (SHJ) is currently become most widely used as a bottom cell for perovskite/silicon-based tandem solar cells [30]. SHJ solar cells become a hot topic within the crystalline silicon PV as it can achieve record-efficiency energy conversion up to 26.6% [31]. The structure of the silicon-based heterojunction is shown in Figure 1. 6.

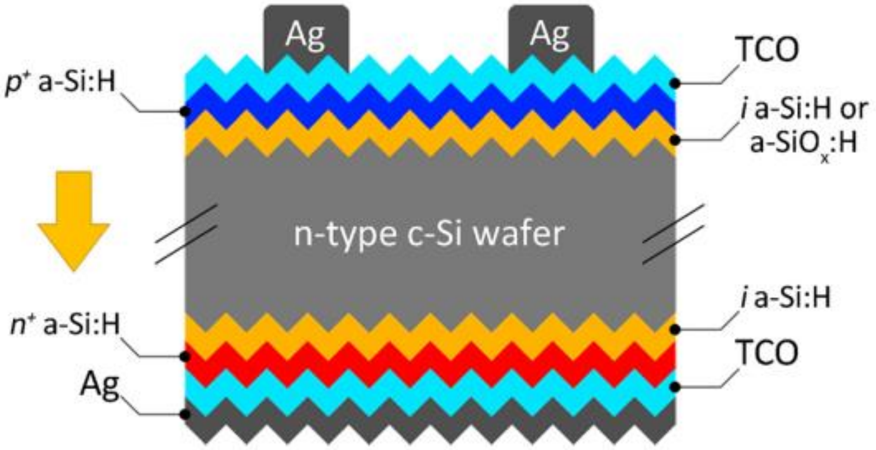

Figure 1. 6. Silicon heterojunction solar cell structure. Adapted from [32].

SHJ has several advantages, including good surface passivation ability with the use of a thin-film silicon amorphous buffer layer that separates the bulk from highly recombinative metallic contacts, the manufacturing process uses low temperature (<300 °C), thereby reducing device production costs, and also an excellent temperature coefficient of -0.23%/°C. This value is lower than the temperature coefficient value of the homojunction silicon technology, which is -0.45%/°C (standard homojunction) [33].

1.5. Present status of the 2T, 3T and 4T perovskite/c-Si tandem solar cells

In this section, the present status of the 2T, 3T and 4T perovskite/c-Si tandem solar cells are summarized.

Table 1. 4. Summary of the present status of the 2T, 3T and 4T perovskite/c-Si tandem solar cells [34] [35] [36].

Author	Published (Y/M)	Area (cm^2)	*Jsc* (mA/cm^2)	*Voc* (V)	FF (%)	PCE (%)
			2T			
HZB	2020/01	1.06				29.1
Kohnen	2019/05	0.77	19.2	1.77	76.6	26.0
Kohnen	2019/05	0.77	17.8	1.77	78.6	25.0
Nogay	2019/03	1.43	19.5	1.74	74.7	25.4
Mazzarella	2019/02	1.10	19.0	1.79	74.6	25.4
Chen	2019/01	0.42	17.8	1.80	79.4	25.4
Oxford PV	2018/12	1.03	19.8	1.80	78.7	28.0
Jost	2018/10	0.77	18.5	1.76	78.5	25.5
Bush	2018/08	1.00	18.4	1.77	77	25.0
F. Sahli	2018/06	1.42	19.5	1.79	73.2	25.5
Zheng	2018	0.16	16.2	1.74	78	21.8
Y.L.Wu	2017	1	17.6	1.75	73.8	22.5
K.A. Bush	2017	1	15.3	1.73	79	18
F. Sahli	2017	0.25	16.8	1.75	77.5	22

Werner	2016	1.43	15.3	1.64	64.8	16
Mailoa	2015	1	11.5	1.85	75	13.7
S. Albrecht	2015	0.16	14	1.79	79.5	18.1
3T						
Tockhorn	2020/01	0.78	Pero: 17.4 IBC: 14.4	1.117 0.600	63.5 64.2	12.3 5.5 ∑ 17.8
4T						
Rohatgi	2020/03	P: 0.1 Si: 4	Pero: 20.6 n-TOPCon Si cell: 16.6	1.100 0.675	78.9 79.6	17.8 8.9 ∑ 26.7
Duong	2020/01	P: 0.21 IBC: 4	Pero: 18.0 IBC: 19.6	1.202 0.697	78.5 78.0	17.0 10.7 ∑ 27.7
Duong	2020/01	P: 1 PERL: 1	Pero: 17.5 PERL:18.6	1.205 0.675	76.3 80.4	16.1 10.1 ∑ 26.2
Wang	2019/		Pero: 19.8 HIT: 15.6	1.156 0.698	79.9 80.1	18.3 8.7 ∑ 27.0
Jaysankar	2019/		Pero: 15.4 IBC: 24.1	1.220 0.678	73.4 81.2	13.8 13.3 ∑ 27.1
Quiroz	2018/		Pero: 21.0 PERL: 17.7	1.098 0.674	74.1 80.1	17.1 9.6 ∑ 26.7
Duong	2017/		Pero: 19.4 IBC: 18.8	1.120 0.690	73.0 80.0	16.0 10.4 ∑ 26.4
Werner	2016/		Pero: 20.1 HIT: 16.0	1.070 0.693	75.5 79.5	16.4 8.8 ∑ 25.2

Table 1. 4 the latest and the highest perovskite-based tandem cell for 2T, 3T and 4T. Until 2020, the highest efficiency of the 2T, 3T and 4T perovskite/c-Si tandem solar cells are 29.1%, 17.8%, and 27.7%, respectively.

The highest efficiency of 2T perovskite/c-Si tandem solar cells has been achieved by Helmholtz-Zentrum Berlin (HZB). Only general information can be obtained because the journal regarding it has not been published yet. Practically, the 2T tandem perovskite/c-Si solar cells can reach about 35% efficiency and theoretically, it can be increased until 45% efficiency under standard test conditions (AM1.5G, 1kW /m^2, 25 °C) [37]. Until now, to surpass above the 30% efficiency, there are still many challenges, such as the recombination layers that should be compatible with minimal voltage and optical losses, controlling the light within the device including transparency of top electrode, reduction in reflection, and increased the perovskite's cell stability [38].

For the 3T perovskite/c-Si tandem solar cells, only a few pieces of information can be obtained regarding the experimental of these tandem configurations. The latest experiment was conducted by Tockhorn et al. They were fabricated 0.78 cm^2 of 3T perovskite/Si tandem solar cell with 17.8% efficiency [39]. The highest efficiency of 4T perovskite/c-Si until now is achieved by Duong et al. from Australian National University with 27.7% efficiency [40].

1.6. Carrier selective passivating contacts

Carrier selective passivating contacts are basically thin films deposited on the silicon wafer and have a function as a carrier selective and surface passivation.

1.6.1. Carrier selective contacts

Carrier selective contact has become an essential part of the solar cell. It acts like a filter that allows only one carrier type, either only electrons or hole, to pass through the contact while blocking the other one [41].

The idea of the carrier-selective concept is based on obtaining a high degree of carrier selectivity [41]. To achieve that, the doping concentration needs to be increased significantly, but the increasing of the doping concentration inside the absorber will raise the level of intrinsic charge carrier recombination, i.e., Auger recombination, which it does not expect to happen. To avoid these recombinations and reduce the process complexity, the carrier-selective contact is separated from the absorber [41].

1.6.2. Surface passivation

A brief description of surface passivation and also five passivation techniques are given.

Surface passivation is a method to reduce the defect density by placing a thin layer of suitable material over the semiconductor surface [7]. The thin layer will act as a valence electrons donor so that the covalent bonds on the semiconductor surface will be formed and the surface trap density (*NsT*) will be reduced [7]. The density of the surface trap (*NsT*) needs to be lower, so the carrier lifetimes will be higher, leading to higher efficiency cells [7].

Surface passivation can be achieved using five different techniques, i.e., deposition of dielectric film, chemical methods, field effect passivation, high-low junction and p-n junction [42].

Depositing of dielectric films

The most widely used of surface passivation technique in crystalline silicon solar cells [42]. Various of deposition methods such as chemical vapor deposition (CVD), physical vapor deposition (PVD) and thermal oxidation are used to deposit dielectric material such as SiNx, TiO_2 and Al_2O_3 [43].

Chemical methods

The chemical methods are the passivation technique that works by involving the oxidation process [42]. First, the solar cells will undergo a standard cleaning then dipped into a liquid solution such as H_2SO_4, HF or HNO_3. After that it will be heated for a specific duration. After the chemical passivation process is successful, the effective lifetime of minority carriers will be improved [42].

Field effect passivation

Field-effect passivation is a technique for reducing surface recombination by using electric field effect [42]. This technique is highly stable and can drive out a certain type of carrier, which can lower the surface recombination in a certain area [42].

High-low junction

This technique also uses the electric field effect for reducing recombination [42]. The working principle of this technique is the diffusion of high carriers density of the front surface field (FSF) and back surface field (BSF) to either front or back layers to achieve passivation. That is possible if the carrier density of the bulk of the solar cells is lower than the carrier density of FSF and *BSF* [42].

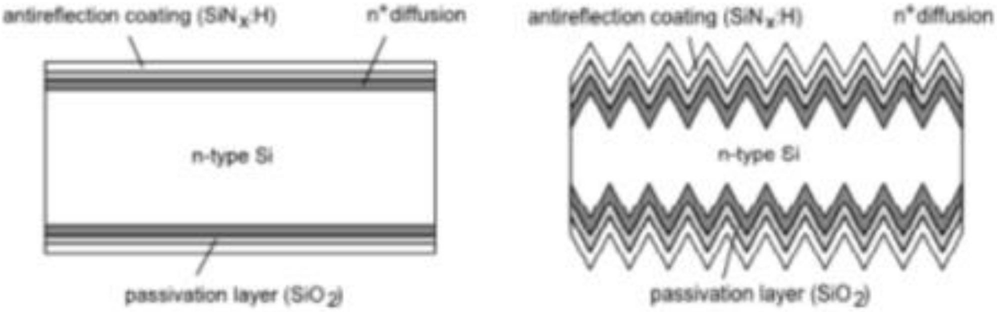

Figure 1.2. Solar cell with diffused FSF and BSF. Left: Flat type solar cell. Right: Textured solar cell. Adapted from [42].

p-n junction

The working principle of p-n junction passivation is similar to the high-low junction passivation. The small difference is the inclusion of *n* and *p*-type dopant atoms [42]. A combination of *n* and *p* doped atoms results in a shift of Fermi energy levels, which produces a higher energy barrier compared with high-low junction passivation. A high energy barrier leads to better passivation of the solar cell. This technique is used in high-efficiency solar cells, such as PERL solar cells [42].

Good carrier-selective passivating contacts are the materials that can provide excellent passivation, high carrier selectivity and also low contact resistivity [41].

The following are some materials that have been used as a carrier-selective passivating contacts.

Poly-Si

Poly-Si has been widely used as a carrier-selective passivating contacts (CSPCs) [44] [45] [46]. The implied V_{oc} of 721(692) mV for *n*-type(*p*-type) had been reported using poly-Si as CSPCs [44]. The fill factor of 75.2% has been achieved on a front textured IBC solar cell using poly-Si as passivating contacts, which denotes good carrier transportation between poly-Si and c-Si through the junction of the solar cell [44]. Nevertheless, the 250 nm of poly-Si used in solar cells has significant free carrier absorption, which reduces the performance of the solar cells [47] [48].

Poly-SiO_x

Poly-SiO_x is a further development of poly-Si in terms of carrier-selective passivating contacts [47]. It is a promising material due to the extremely high passivation quality that has been achieved [47]. Poly-SiO_x is the enhancement of poly-Si as a passivation material. When forming a poly-SiO_x, the oxygen content was optimized, so the free carrier absorption is minimal. The implied V_{oc} can reach up to 740 (700) mV for *n*-type (*p*-type) poly-SiO_x [47]. Based on G. Yang et al.'s experiment, the solar cell had a fill factor of 83.5%, which indicates that the carrier transport to the junction is successfully efficient [47].

Poly-SiC_x

Poly-SiC_x has been validated as a promising passivating contacts in the high-efficiency solar cells [49]. The efficiency of 20.17% has been achieved by using this material [50]. High passivating quality of poly-SiC_x depends on the following factors, i.e., doping ratio R of carbon [methane flow (sccm)/silane flow (sccm)] and the annealing temperature [50]. The higher level of both factors is essential to achieve a high carrier lifetime [50].

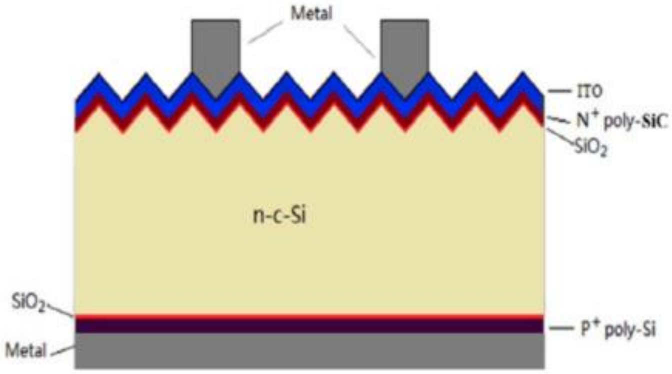

Figure 1.3. The example of passivation contact structure using poly-SiCx/poly-Si on the top/rear side of the solar cell. Adapted from [50].

Figure 1.3 shows an example of the solar cell structure that uses carrier-selective passivating contacts (CSPCs). As shown in Figure 1.3, (*n*) poly-SiC$_x$/SiO$_2$ has a role as a CSPCs at the solar cell's front contact, whereas (*p*) poly-Si/SiO$_2$, which also acts as a CSPCs is placed at the rear contact of the solar cell.

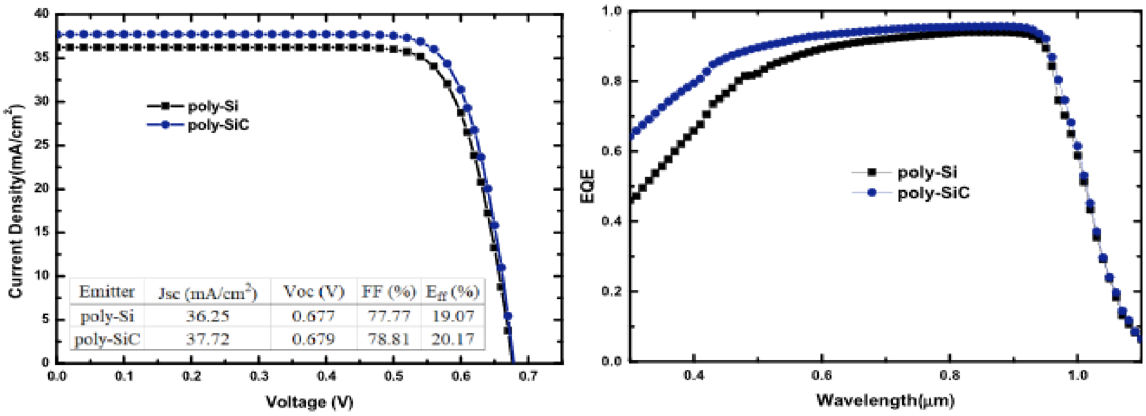

Emitter	Jsc (mA/cm^2)	Voc (V)	FF (%)	E$_{ff}$ (%)
poly-Si	36.25	0.677	77.77	19.07
poly-SiC	37.72	0.679	78.81	20.17

Figure 1.4. Left: The comparation of I-V curve of solar cells using poly-Si and poly-SiCx as the front contacts. Right: The comparison of external quantum efficiency (EQE) curve of the solar cell. Adapted from [50].

Figure 1.4 compares the performance of poly-Si and poly-SiC$_x$ as the passivating contacts at the front side of the solar cells. The thickness of both poly-Si and poly-SiC$_x$ is 15 nm, respectively. The performance properties of the solar cells, such as saturation current density (J_{sc}), open-circuit voltage (V_{oc}), fill factor (FF) and efficiency (η), are shown. As can be seen in Figure 1.4, poly-SiC$_x$ achieved a higher value in all parameters than poly-Si. This phenomenon happened due to the higher parasitic absorption of poly-Si at the front contact of the solar cells [50].

For the EQE, in the short-wavelength area, poly-SiC$_x$ also achieved a higher EQE than poly-Si. Based on those data, poly-SiC$_x$ contact has a better performance than poly-Si when they are placed at the front side of the solar cells.

1.7. Tunnel recombination junction

Tunnel recombination junction (TRJ) is an interlayer that connects two subcells in the solar cell structure [51]. TRJ has an important role in optimizing the performance of the tandem solar cells [51] [52]. TRJ has a function to provide enough recombination. If not, the light will induce dipole due to the accumulation of the trapped electrons or trapped holes, which would make the electric field on top and bottom cell getting weaker. Afterward, it will degenerate the performance of the tandem solar cell [51].

1.7.1. The example of tunnel recombination junction

Figure 1. 7 (a) and (b) show the structure of the GaAsPN/Si tandem solar cells and the simulated band diagram of GaP (n) and Si (p) tunnel junctions, respectively.

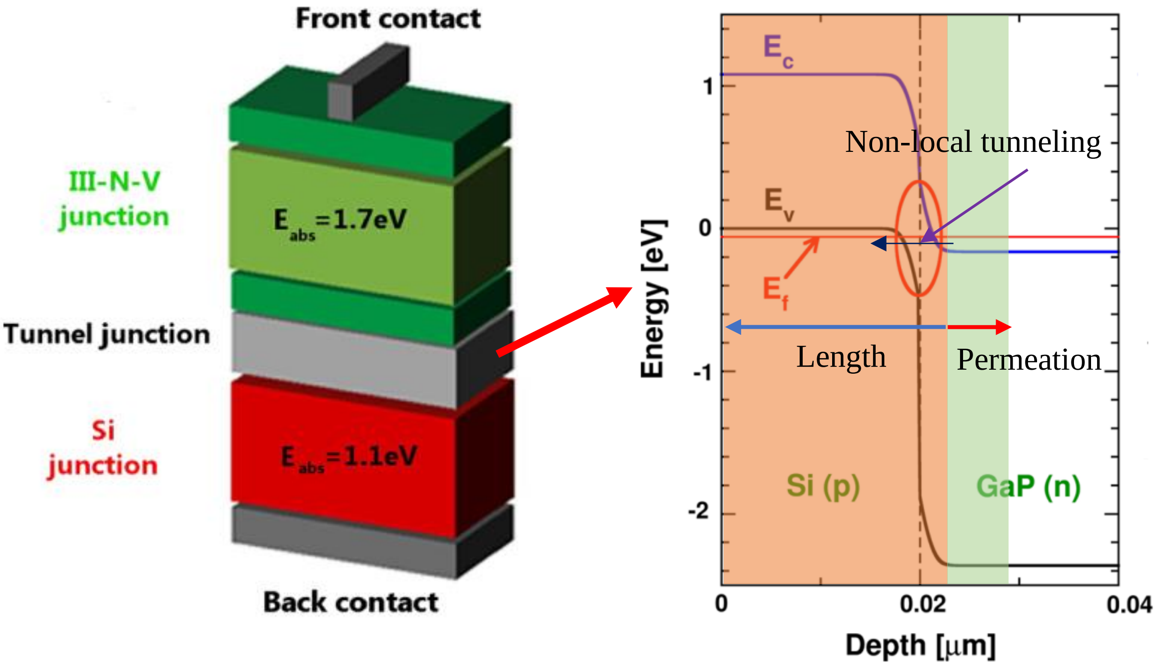

(a) (b)

Figure 1. 7 (a). The GaAsPN/Si tandem solar cells structure, (b) Simulated band diagram of GaP (n)/Si (p) tunnel junctions. Adapted from [53].

The red circle is shown in Figure 1. 7 (b) represents the depleted region. When the doping concentration of Si (*p*) and GaP (*n*) is high, the depleted region becomes thinner and an electron can penetrate the barrier, as indicated by the black arrow. This process is called tunneling. Tunneling can be divided into two different approaches, i.e., local and non-local tunneling [54].

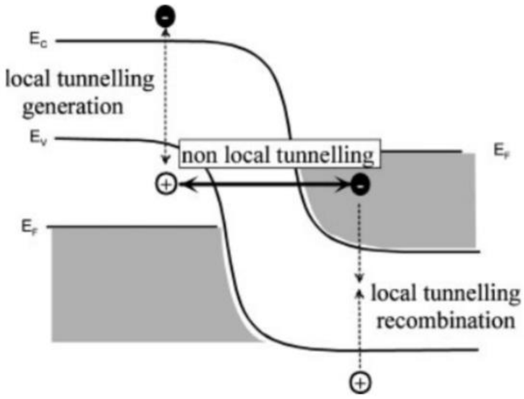

Figure 1. 8. The difference between the local and non-local tunneling models. Adapted from [54].

In local tunneling, no real carrier transport through a barrier occurs, while in non-local tunneling, carriers are transporting through a barrier. In non-local tunneling, the recombination of electrons and holes are occurring at different positions [54]. In this thesis work, the non-local tunneling is modeled by using a band to band tunneling. Band to band tunneling is one of the fundamental tunneling mechanism in such *pn*-junctions. For the band to band tunneling, the tunneling process is directly happening from band to band. To implement band to band tunneling, non-local mesh (NLM) should be created. Sentaurus TCAD, as electrical simulation software, facilitates the implementation of non-local tunneling in the model by using

NLM. As shown in Figure 1. 7 (b), the length and permeation terms are introduced. Length value specifies the maximum distance of the vertex to the reference surface, whereas permeation specifies the extended length of non-local lines, across the reference surface, toward the opposite direction of the length parameter [55].

1.7.2. The Fermi energy

Fermi energy (E_F) is the electrochemical potential of the electron in the material. It represents the averaged energy of electrons in material. The Fermi energy is a temperature-dependent quantity. It can also be called the Fermi level. The relation of the Fermi energy and the charge carriers are as follows

$$n = N_c \exp(\frac{E_F - E_C}{k_B T}) \text{ for } E_C - E_F \geq 3k_B T \tag{1}$$

$$p = N_V \exp(\frac{E_V - E_F}{k_B T}) \text{ for } E_F - E_V \geq 3k_B T \tag{2}$$

where E_C is the minimum reachable conduction-band energy, E_V is the maximum reachable valence-band energy, k_BT is the thermal energy, N_C and N_V are the effective densities of the conduction band states and the valence band states, respectively. N_C and N_V are defined as follows.

$$N_C = 2\,(\frac{2\pi m_n^* k_B T}{h^2})^{\frac{3}{2}} \text{ and } N_V = 2\,(\frac{2\pi m_p^* k_B T}{h^2})^{\frac{3}{2}} \tag{3}$$

where m_n^* and m_p^* are the effective mass of the electrons and holes, respectively and h is the Planck constant.

1.8. Carrier transport phenomena

The carrier transport phenomena are fundamental for determining the current-voltage characteristic of semiconductor devices. In this section, two basic transport mechanisms in a semiconductor, i.e., drift and diffusion, are explained.

1.8.1. Drift

Drift is the charged particle movement due to an electric field. In an electric field, the positively charged holes will be accelerated in the same direction of the electric field, whereas the negatively charged electrons will go in the opposite direction. The carrier acceleration is often disturbed because of two conditions. The first is a collision with the thermally vibrating lattice atoms and second is with ionized impurity atoms. The resulting motion of the charge carriers can be expressed by the average drift velocities (v). The average drift velocities for electrons (v_{dn}) and holes (v_{dp}), in the case of low electric fields, can be expressed as

$$v_{dn} = -\mu_n \xi \tag{4}$$

$$v_{dp} = -\mu_p \xi \tag{5}$$

where μ is the proportionality factor called mobility. It is an important parameter of the semiconductor, which describes how good a particle will move due to an electric field. By multiplying the average drift velocities of each carrier type with elementary charge and its concentrations, the electron and hole drift current density can be obtained. The formulas are shown as follows

$$J_{n,drift} = -qnv_{dn} = qn\mu_n \xi \tag{6}$$

$$J_{p,drift} = qpv_{dp} = qp\mu_p \xi \tag{7}$$

The electron drift current densities become positive (the same direction as the electric field) due to the negative charge of an electron. By combining equation (6) and (7), the total drift current can be expressed as follows

$$J_{drift} = q(p\mu_p + n\mu_n)\xi \tag{8}$$

1.8.2. Diffusion

The second mechanism, in addition to drift, that can lead a current in a semiconductor is diffusion. It is a process whereby particles flow from high concentration region to low concentration region as an effect of random thermal motion. In the diffusion transport mechanism, the particles do not need to be charged to be involved in the diffusion process. The driving force comes from the gradient in the particle concentration. The current as a result of diffusion is proportional to the gradient in particle concentration. The formula of the electron and hole diffusion current densities can be formed as follows

$$J_{n,diff} = qD_n\nabla_n \tag{9}$$

$$J_{p,diff} = -qD_p\nabla_p \tag{10}$$

where q is the elementary charge, D_n and D_p are the electron and hole diffusion coefficients, respectively and ∇_n and ∇_p are the electron and hole density gradients, respectively. Combining equation (9) and (10) will lead to the total diffusion current formula as follows

$$J_{diffusion} = q(D_n\nabla_n - D_p\nabla_p) \tag{11}$$

The total current density (J) is the sum of the total drift current (J_{drift}) and total diffusion current ($J_{diffusion}$).

$$\begin{aligned} J &= J_{drift} + J_{diffusion} \\ &= q(p\mu_p + n\mu_n)\xi \; + q(D_n\nabla_n - D_p\nabla_p) \end{aligned} \tag{12}$$

1.9. Carrier generation and recombination

In this section, the definition of generation and recombination will be explained. The different types of recombination are also explained in detail.

Generation is a process whereby electrons and holes are created, whereas recombination is a process whereby electrons and holes are eliminated. The generation process that happens from bandgap to bandgap is called *direct* generation. This process happens in direct bandgap materials whereby there is no change of momentum needed for electrons to excite into the conduction band. This process is mostly radiative, i.e., the electron-hole pair is generated due to absorbed photons and a photon is emitted if electron-hole pairs recombine directly.

The recombination plays an important role in the solar cells' performance, such as: reducing the current that can be collected and utilized from the solar cells and affecting the solar cell voltage, which leads to influence the energy conversion efficiency of the solar cells. The recombination mechanism can be divided into several types, i.e., direct recombination, Shockley-Read-hall recombination, Auger recombination and Surface recombination.

1.9.1. Direct recombination

Direct recombination mainly happens in direct bandgap semiconductors. The generated excess carrier concentrations (Δn) and (Δp) with

$$n = n_o + \Delta n \text{ and } \mathrm{p} = p_o + \Delta p \tag{13}$$

can be decreased due to recombination of charge carriers (R). In steady state, the direct recombination (R_d) is given by

$$R_d = c_d(np - {n_i}^2) \tag{14}$$

where c_d is the direct recombination coefficient, n and p are the electron and hole concentrations, respectively and n_i is the intrinsic carrier concentrations. If the semiconductor is assumed under low-level injection, for the *n*-type and *p*-type semiconductor, the recombination rate formula can be expressed as

$$R_d \approx c_d n_0(p - p_0) = \frac{p - p_0}{\tau_{pd}} \tag{15}$$

$$R_d \approx c_d p_0(n - n_0) = \frac{n - n_0}{\tau_{nd}} \tag{16}$$

respectively. The lifetime of minority holes and minority electrons are given by

$$\tau_{pd} = \frac{1}{c_d n_0} \tag{17}$$

$$\tau_{nd} = \frac{1}{c_d p_0} \tag{18}$$

where n_o and p_o are the equilibrium concentrations.

1.9.2. Shockley-Read-Hall recombination

Shockley-Read-Hall (SRH) recombination is the type of recombination process when the recombination of electrons and holes does not happen directly from bandgap to bandgap but facilitated by the lattice defects. In the center of the recombination, there is an allowed energy level within the forbidden gap called trap states. It can trap free charge carriers and lead to very effective recombination. The SRH recombination rate formula is expressed as follows

$$R_{SRH} = \upsilon_{th}\sigma N_T \frac{np - n_i^2}{n + p + 2n_i \cosh(\frac{E_T - E_{Fi}}{k_B T})} \tag{19}$$

Where υ_{th} is the thermal velocity, σ is the capture cross-sections, N_T is the trap density, n and p are the electron and hole concentrations, n_i is the intrinsic carrier concentrations, E_T is the trap energy, E_{Fi} is the Fermi energy level in the intrinsic material, k_BT is the thermal energy at 300 K. For the *n*-type semiconductor at low injection rate, $n \approx n_o$, where n_o is the electron concentration under thermal equilibrium and under the assumption of $n >> p$, the formula of the R_{SRH} become

$$R_{SRH} = \upsilon_{th}\sigma N_T \frac{p - p_0}{1 + 2\frac{n_i}{n_0}\cosh(\frac{E_T - E_{Fi}}{k_B T})} = c_p N_T(p - p_o) = \frac{p - p_0}{\tau_{p,SRH}} \tag{20}$$

where c_p is the hole capture coefficient and $\tau_{p,SRH}$ is the lifetime of holes in an *n*-type semiconductor. For the *p*-type semiconductor at a low injection rate, the formula can be expressed as follows

$$R_{SRH} = v_{th}\sigma N_T \frac{n-n_0}{1+2\frac{n_i}{p_0}\cosh(\frac{E_T-E_{Fi}}{k_BT})} = c_nN_T(n-n_o) = \frac{n-n_0}{\tau_{n,SRH}} \tag{21}$$

where c_n is the electron capture coefficient and $\tau_{n,SRH}$ is the lifetime of electrons in an *p*-type semiconductor.
The relation of the lifetime of holes (electrons) with the holes (electrons) capture coefficient are shown as follows

$$\tau_{p,SRH} = \frac{1}{c_pN_T} \text{ and } \tau_{n,SRH} = \frac{1}{c_nN_T} \tag{22}$$

The equations (25) show that the lifetime of minority carriers due to SRH recombination is inversely proportional to the trap density. Therefore, it is important to keep the trap density low to have a good semiconductor.

1.9.3. Auger recombination

Auger recombination is important in indirect semiconductors. It is a three particle process as shown in Figure 1. 9.

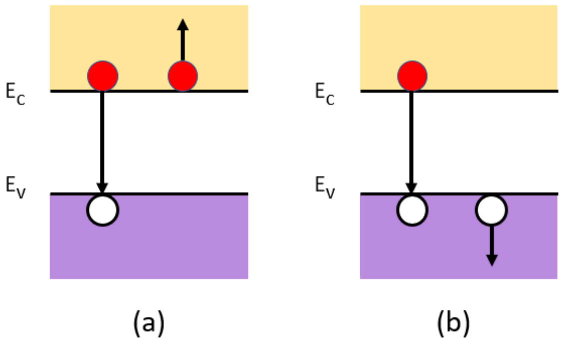

Figure 1. 9. Auger recombination illustration with (a) two electrons; and (b) two holes. Adapted from [56].

The Auger recombination rate (R_{Aug}) strongly depends on the charge carriers. As it is a three particle process, the recombination rate for electron-electro hole (*eeh*) and electron-hole-hole (*ehh*) process are expressed as

$$R_{eeh} = C_nn^2p \tag{23}$$

$$R_{ehh} = C_pnp^2 \tag{24}$$

respectively, where C_n and C_p are the proportionality constant which strongly depend on temperature . R_{eeh} is dominant when the electrons become the majority charge carrier, whereas R_{ehh} is dominant when the holes become the majority charge carriers. R_{Aug} can be obtained by adding the equation (23) and (24).

$$R_{Aug} = R_{eeh} + R_{ehh} = C_nn^2p + C_pnp^2 \tag{25}$$

1.9.4. Surface recombination

Surface recombination is one of the recombination mechanism that needs to be minimized because It will reduce the current that can be collected and utilized from the solar cell. Surface recombination occurs due to the presence of many valence electrons on the silicon surface that cannot find a partner to form a covalent bond. That condition will create defect which is so-called dangling bond as can be seen in the Figure 1. 10 below [7].

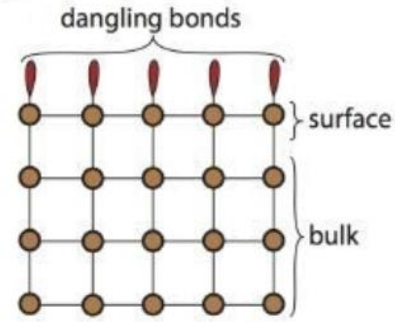

Figure 1. 10. Dangling bonds on c-Si surface. Adapted from [7]

Due to those dangling bonds, many trap states are built within the bandgap. Those trap states will capture the electrons from the conduction band. These trapped electrons will attract the holes and consequently lead to form a which so-called *Shockley – read – Hall* (SRH) recombination [7].
The surface recombination rate (R_s) for n-type semiconductors can be approximated using the following equation:

$$R_s \approx S_r \left(p_s - p_0\right) \tag{26}$$

where:
S_r is the surface recombination velocity, [cm/s].
p_s is the hole concentration at the surface.
p_0 is the equilibrium hole concentration.

Surface recombination velocity is used to specify the number of carriers recombining on the surface per unit area per unit time per unit volume of excess bulk carriers. It can be expressed as:

$$S_r = v_{th}\, \sigma_p\, N_{sT} \tag{27}$$

where:
v_{th} is the thermal velocity, [cm/s].
σ_p is the capture cross-section for holes, [cm^2].
N_{sT} is the surface trap density, [cm^{-2}].

For p-type semiconductor, σ_p, p_s and p_0 should be replaced with σ_n, n_s and n_0, respectively [7].

1.10. Simulation software

In this section, a brief description of the simulation software that have been used while executing the simulations of solar cells is given.

Optical simulations have been conducted using GenPro4 and for electrical simulations Sentaurus TCAD has been used.

1.10.1. Optical simulation using GenPro4

Optical simulation is an important step when designing a solar cell [57]. It provides a detailed understanding of the cells' optical properties, such as reflection and parasitic absorption losses. To have a high quality of solar cells, reflection and parasitic absorption need to be as low as possible.

GenPro4 is a Matlab-based program developed at Delft University of technology, which provides the reflectance, absorptance of each layer and also transmittance as a function of wavelength [58]. GenPro4 has been approved to simulate a wide range of wafer-based and thin-film solar cells [58]. Now it also has been commercially available to the photovoltaics society. Not only optical properties, but GenPro4 can also simulate textured surfaces in solar cells [58].

1.10.2. Electrical simulations

In this section, the importance of doing electrical simulations and a brief description of the electrical simulations software is given.

Electrical simulation are playing an important role in solar cell design. It replicates the behaviour of an actual electronic device or circuit then reveals the performance parameter of the solar cell, such as: fill factor, short circuit current density (J_{sc}) and open-circuit voltage (V_{oc}) [59].

Sentaurus is one of the products of Synopsis Corp which simulates the production, operation and reliability of the semiconductor devices [60]. It provides an important insight into semiconductor devices' behaviour, which can lead to new device concepts [60]. Sentaurus can be divided into four specialized areas, i.e., process simulation, structure editing, framework and device and interconnect simulation [60]. The detailed of the Sentaurus TCAD suite can be seen in the following figure.

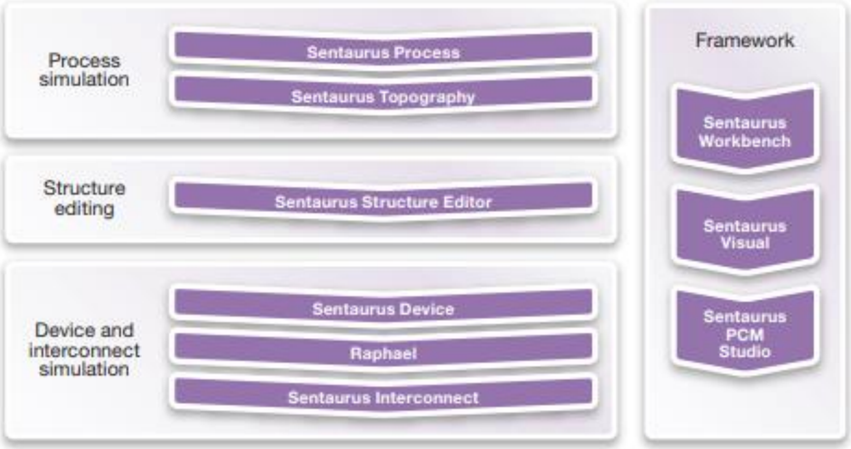

Figure 1.5. Sentaurus TCAD suite. Adapted from [60].

Figure 1. 5 shows the various tools included in the TCAD Sentaurus. In this thesis work, some of the tools from Sentaurus TCAD that are used for electrical simulations are the Sentaurus workbench (SWB), Sentaurus structure editor (SDE), Sentaurus Mesh (SNMesh), MatPar, Sentaurus device (SDevice), and Sentaurus Visual.

Sentaurus Workbench (SWB)

Sentaurus workbench is a synopsys framework designed to facilitate the use of tools from Sentaurus TCAD. SWB makes it easy for users to input system commands for handling data files. The advantage of using SWB is the possibility to run various simulation group automatically. By using SWB, users can integrate various Sentaurus TCAD tools into one framework [61].

Sentaurus structure editor (SDE)

Sentaurus structure editor is used to edit and generate device structures in either a 2D or 3D form. The device can be generated or edited interactively or by using a script. SDE supports various things such as generating model geometry, define contact regions, add the doping profile, define local refinements, etc [62].

Sentaurus Mesh (SNMesh)

Sentaurus Mesh is a tool from Sentaurus TCAD which functions to produce finite-element meshes used in semiconductor device simulations, process simulations and electromagnetic simulations. SNMesh has three mesh generation engines, i.e., an axis-aligned mesh generator, an offsetting mesh generator and a tensor-product mesh generator [63].

MatPar

MatPar is one of the Sentaurus TCAD tools that has various functions, including organize model parameters in hierarchical material parameter database, generates material parameter files to be used in device simulations, generate region-wise, material-wise, and interface-wise pre-processes parameter files, and also it can combine the global parameter database and local parameter database which is defined by the user [64].

Sentaurus Device

Sentaurus Device is used to simulate numerically electrical behavior from the semiconductor device. The physical models of the devices used for the simulation are inputted through this tool. Typical tool flow for a device simulation using SDevice is shown in Figure 1. 11 below.

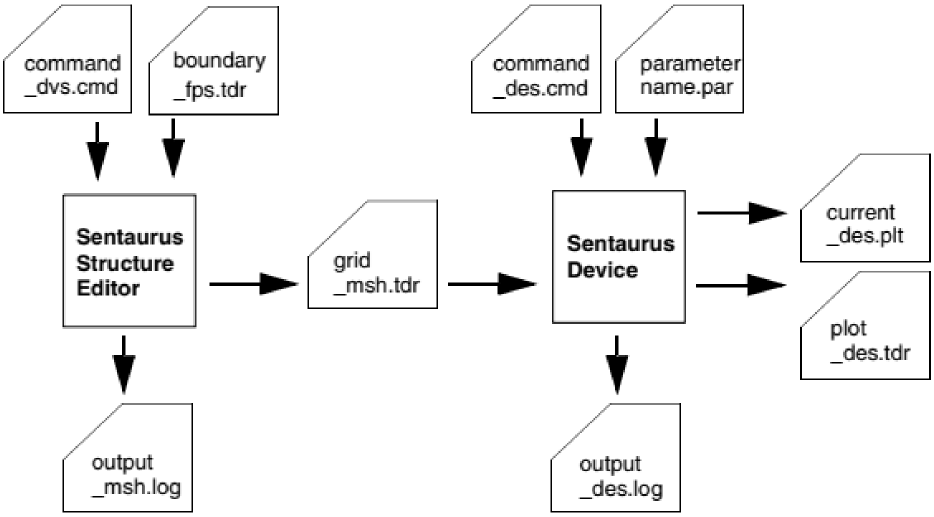

Figure 1. 11. Device simulation process flow using Sentaurus Device. Adapted from [55].

Sentaurus Visual

Sentaurus Visual is used to visualize the output of the simulation in 2D and 3D. Sentaurus visual can also be used to extract simulation data on SDevice. In this thesis work, the electrical output parameters such as J_{sc}, V_{oc}, *FF* and η are extracted using SVisual [65].

1.11. Objective and research question

The main objective of this master thesis is to optimize perovskite/c-Si tandem solar cells in which the bottom cell uses the novel carrier selective passivating contacts materials poly-Si, poly-SiO$_x$ and poly-SiC$_x$. The main research questions in this thesis are:

1. What is the optimum and realistic implied photo-current density generated by the 2T, 3T and 4T perovskite/c-Si tandem solar cells structure using the novel carrier selective passivating contacts materials (poly-Si, poly-SiO$_x$ and poly-SiC$_x$)? What are the optical losses due to these novel materials?
2. What are the optimum parameters and efficiency of the top cell (perovskite solar cell)? The parameters optimized are contact resistance, surface recombination velocity and the thickness of

each layer. These optimized parameters are used in the simulations of 2T tandem solar cells. The optimized parameters of the bottom cell have been taken from other work.

3. What is the optimum tunnel recombination junction used in the 2T perovskite/c-Si tandem solar cells? In this case, the optimized parameter is the doping of the tunnel recombination junction layers.

1.12. Outline

This thesis consists of five chapters. Chapter 2 explains the optical simulations in detail. Starting from the required input parameters, the steps of work, the output generated from optical simulation, and analysis of the generation profile produced. Chapter 3 explains the optimization of the perovskite solar cells used as the top cell in the 2T tandem. The electrical simulations of the 2T perovskite/c-Si tandem solar cells and optimization of the tunnel recombination junction are explained in Chapter 4. Finally, chapter 5 presents the summaries of the works and the recommendations for further research.

2. Optical Simulations

This chapter is aimed to answer the first research goals introduced in subchapter 1.10 which was "How much the optimum and realistic implied photo-current density generated by the 2T, 3T and 4T perovskite/c-Si tandem solar cells and also the optical losses of CSPCs in each optimum structure?" to answer the main research questions, the main research questions are divided into three sub-questions, i.e., "How much the implied photo-current density produced by the 2T, 3T and 4T tandem perovskite/c-Si using the novel carrier selective passivating contacts materials (poly-Si, poly-SiO_x and poly-SiC_x)?", "How much the implied photo-current density of the 2T, 3T and 4T tandem perovskite/c-Si after the thickness optimization?" and "How much the implied photo-current density generated by adding an encapsulation material to the tandem structure?" First, the tandem structure of each configuration will be presented in subchapter 2.1, the input parameters such as *n* and *k* data which were used and the thickness of each layer are presented in subchapter 2.2, the method to calculate the implied photo-current density is explained in section 2.3, the optical simulation results are presented in section 2.4, the discussion related the results are shown in section 2.5 and the conclusions are presented in section 2.6.

2.1. Tandem Structure

In this section, the structures of the 2T, 3T and 4T perovskite/c-Si tandem solar cells used in optical simulations are explained.

2.1.1. 2T perovskite/c-Si tandem solar cells structure

In this report, as can be seen in Figure 2. 1, the 2T perovskite/c-Si tandem solar cell consists of two structures, i.e., non encapsulated and encapsulated by glass and EVA. The non-encapsulated structure is divided into two types, i.e., before thickness optimization and after thickness optimization. The thickness of the top cell has been optimized both optically in GenPro4 and electrically in Sentaurus TCAD. The purpose of these two structures is to know how much the highest J_{ph} can be achieved and how much the optimum and realistic J_{ph} can be generated using this tandem structure.

The top cell of the tandem is adapted from [66] [67]. It consists of the fluorine-doped tin oxide (SnO_2), the electron transporting layer (TiO_2), mixed halide perovskite ($CH_3NH_3PBI_{3-x}Cl_x$) as the absorber layer, and hole transporting layer (spiro-OMeTAD). This top cell structure has several advantages over the commonly used perovskite ($MAPBI_3$) such as better charge collection efficiency and reproducibility [27]. To increase the amount of light absorbed in the absorber, MgF_2 as an anti-reflective coating is added. The bottom cell is currently being developed in TU Delft. It uses high carrier-selective passivating materials such as poly-SiO_x and poly-SiC_x. The top cell and bottom cell are connected optical and electrically by ITO. ITO acts as the tunnel recombination junction. The detail of the structure can be seen in Figure 2. 1. The encapsulated materials such as glass and EVA are added into the structure. Glass is very important to be added because it has some major functions such as transmit the incident solar radiation to the absorber with minimum loss and protect the PV module from the environment [68]. The ethylene-vinyl acetate (EVA) also plays an important role such as: protect the solar cells from environmental damage, mechanical protection and electrical insulation [69]. The detail of the thickness of each layer is explained in section 2.2.

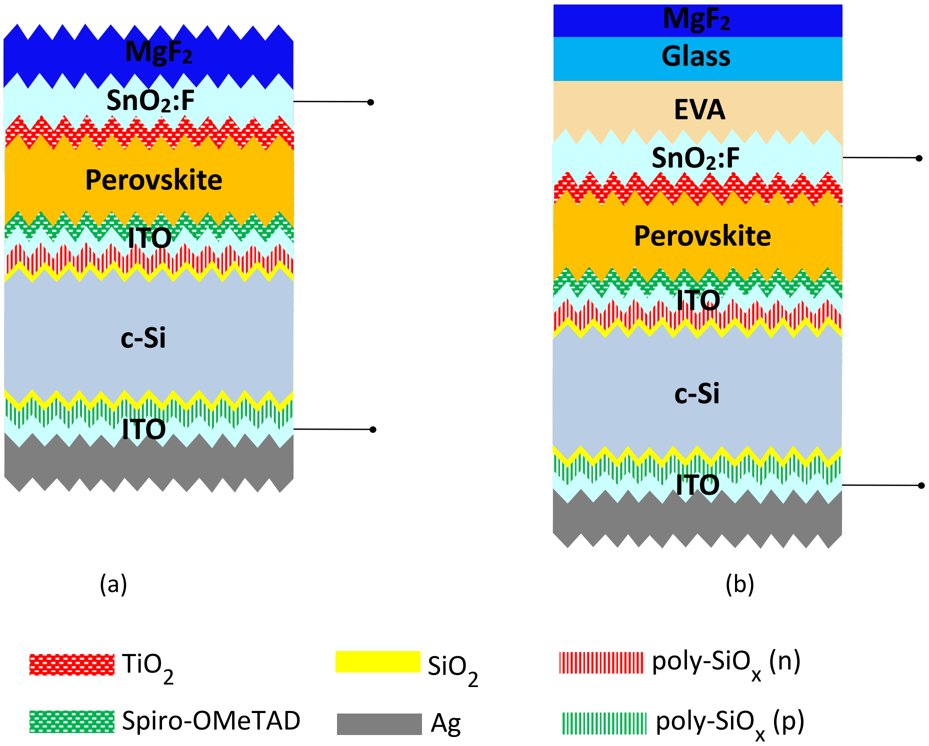

Figure 2. 1. The 2T perovskite/c-Si tandem solar cells structure. (a) Non encapsulated, (b) Encapsulated by glass and EVA.

2.1.2. 3T perovskite/c-Si tandem solar cells structure

The structure of 3T perovskite/c-Si tandem solar cells using different carrier-selective passivating contacts can be seen in Figure 2. 2. Figure 2. 2 (a) shows the 3T tandem structure without encapsulation, whereas in Figure 2. 2 (b) the structures of 3T are encapsulated by glass and EVA. The optical simulations were done for three scenarios. The first and second scenarios are the optical simulations for the non-encapsulated structure before and after thickness optimization. The third scenario is optical simulations after optimizing the thickness and adding an encapsulation material.

The top cell of the 3T perovskite/c-Si tandem is using the same reference as the 2T and 4T perovskite/c-Si tandem. The bottom cell is an interdigitated back contact (IBC) Si device using poly-Si, poly-SiC$_x$ and poly-SiO$_x$ as carrier-selective passivating contacts.

The 3T configuration can be run either in 2T configuration or utilize the second back contact to extract excess current. It is the reason that the choice of perovskite thickness in 3T configuration is more relaxed and does not need current matching [70]. The current of this structure can be extracted in two ways. First, the current is extracted between the front *n*-type contact and the back *p*-type contact. Second, it can also be extracted between the back *n*-type and *p*-type contact [70].

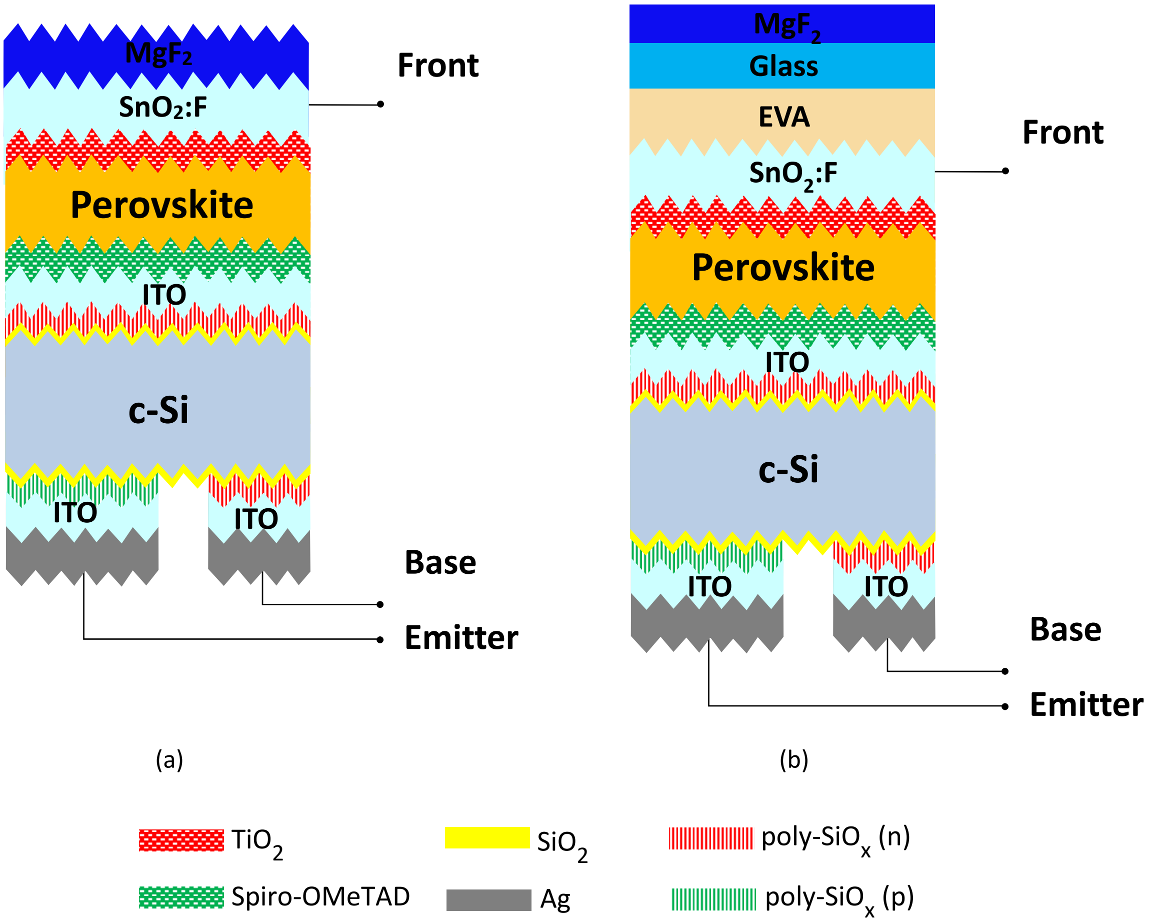

Figure 2. 2. The 3T perovskite/c-Si tandem solar cells structure. (a) Non encapsulated, (b) Encapsulated by glass and EVA

2.1.3. 4T perovskite/c-Si tandem solar cells structure

The structure of the 4T perovskite/c-Si tandem is shown in Figure 2. 3. This structure is quite different from 2T and 3T. First, because each cell in the 4T configuration acts as an individual cell, so it has more ITO layers. The additional ITO layers are placed at the rear side of the top cell and on the bottom cell's front layers, respectively. The ITO is a conductive material and highly transparent. It has been commonly used as TCO layers [71]. It helps the charge carriers travel to the contacts. The side effect of the higher number of the ITO layers is the increase of the parasitic absorption losses. The fabrication of ITO is also still expensive, so that is one of the reasons why 4T configuration is still difficult to penetrate into the market. The production steps are more complex and the production cost is also high. It makes the price of the module is not competitive yet. As can be seen in Figure 2. 3, the tandem structure is flat-textured. Right now, the flat surface of the top cell for 4T configuration is the most possible and realistic way to do [72] [73] [74] [34] [75]. Based on the 4T tandem paper's research, the glass is also put on top of the surface.

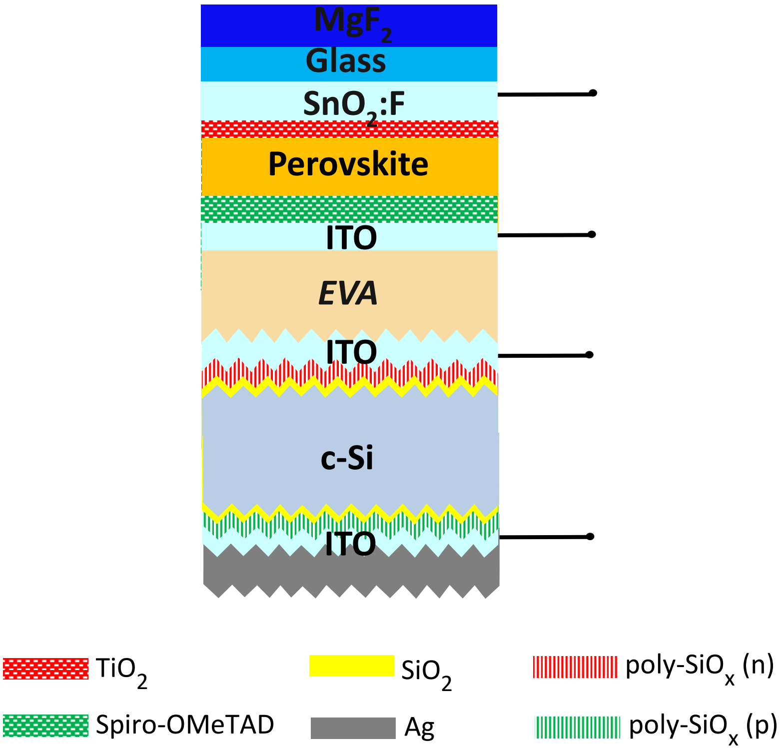

Figure 2. 3. The 4T perovskite/c-Si tandem solar cells structure encapsulated by glass

2.2. Input Parameters

In this section, the input parameters needed to have the accurate optical simulation results are explained.

GenPro4 needs two main parameters to conduct the simulations. First is the optical properties data i.e. refractive index (*n*) and extinction coefficient (*k*) of all layers. Second is the thickness of each layer. The *n* and *k* data from the tandem structure can be seen in Figure 2. 4 and Figure 2. 5.

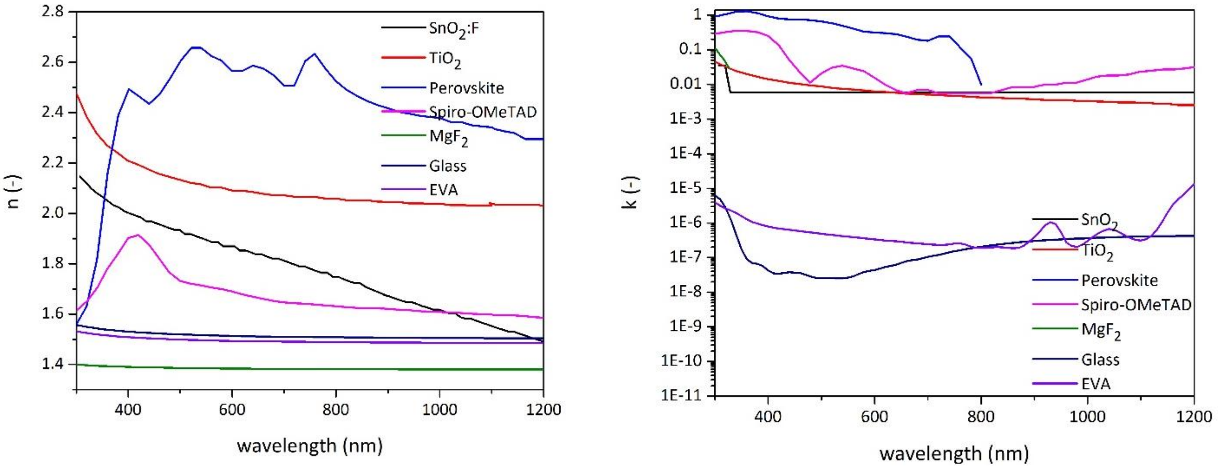

(a) (b)

Figure 2. 4. Optical properties used for the top cells. (a) refractive index n, (b) extinction coefficient k.

Figure 2. 4 (a) and (b) show the refractive index and extinction coefficient of the top cell structure, respectively. These *n* and *k* are obtained from the paper published by Alnuaimi et al [67]. It consists of the SnO_2:F as the FTO layer indicated by the black line, TiO_2 as the electron transporting material indicated by the red line, perovskite as the absorber indicated by the blue line and spiro-OMeTAD as the hole transporting material indicated as the pink line. As can be seen in Figure 2. 4 (a), SnO_2:F has a different refractive index ranging from 2.1 to 1.5 in the wavelength range of 300 to 1200 nm. The extinction

coefficient (*k*) of the SnO_2:F is very low. TiO_2 has a refractive index of around 2.1 and is highly transparent. The extinction coefficient of the TiO_2 is also not too different from the SnO_2:F. The perovskite has a refractive index that varies between 1.5 and 2.7. As can be seen from Figure 2. 4 (b), the extinction coefficient of the perovskite is very high up to 1.3 at the wavelength of 380 nm but it is become zero starting from the wavelength of 800 nm. So that is why photons are highly absorbed by the perovskite at the wavelength of 300 to 800 nm, but it absorbed much less for larger wavelengths. The spiro-OMeTAD has a lower refractive index of around 1.65. Its extinction coefficient is high at the wavelength of 300 nm to 480 nm.

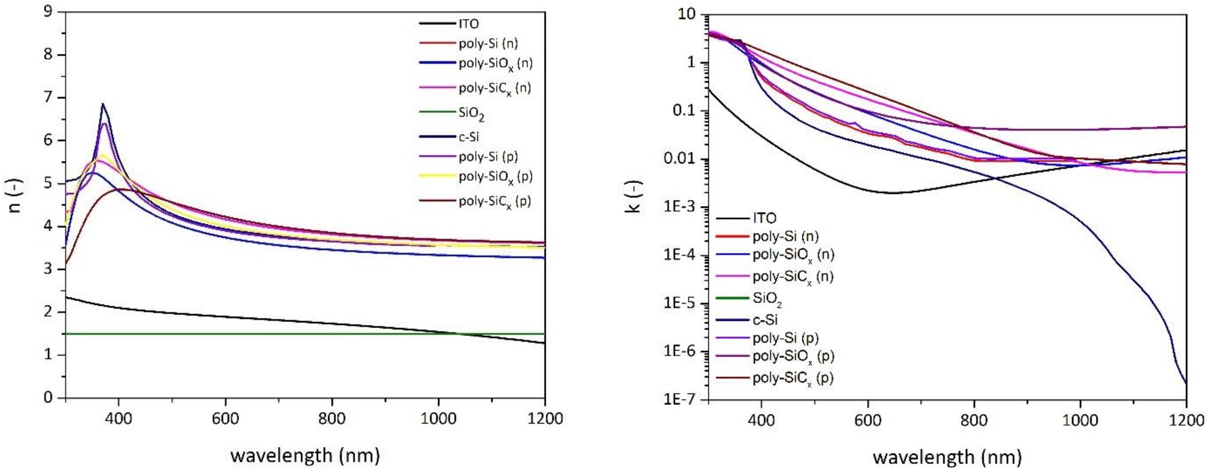

(a) (b)

Figure 2. 5. Optical properties of the bottom cells used. (a) refractive index n, (b) extinction coefficient k.

Figure 2. 5 (a) and (b) show the refractive index (n) and extinction coefficient (*k*) of the bottom cell. The bottom cell consists of the ITO indicated by the black line, poly-Si (*n*)/poly-SiO_x (*n*)/ poly-SiC_x(*n*) as the passivating materials are indicated by the red, dark blue and pink line, respectively. SiO_2 is indicated by the green line. The crystalline silicon as the absorber is indicated by the dark blue line. There are also poly-Si (*p*)/poly-SiO_x (*p*)/ poly-SiC_x(*p*) indicated by a purple, yellow and brown line, respectively. As can be seen from Figure 2. 5 (a), SiO_2 has the lowest refractive index value among others. ITO has a refractive index of around 1.8. Its value is not too different from SiO_2. Other than these layers, the refractive index value is very high, ranging from 3 to 6.8. These materials are highly transparent. From Figure 2. 5 (b), it shows that most of the materials are highly absorbing up to 800 nm of wavelength.

The second main parameter to be inputted in GenPro4 is the thickness of each material. Table 2. 1 shows the detailed thickness of each layer. The thickness is divided into three categories i.e. non-optimized, after optimized and encapsulated by the glass. The thickness of the top cell which is SnO_2:F, TiO_2, perovskite and spiro-OMeTAD are obtained from the paper published by Alnuaimi et al [67]. These values are inputted into the non-optimized column. However, the perovskite thickness is subject to be adjusted to get the current matching, so the perovskite thickness is not included in the table. The layer thickness optimization is only done for the top cell, for the bottom cell the values are kept the same. The optimum thickness value of each layer was obtained by using optical and electrical simulations. The detail of the optimization of the top cell electrically is explained in Chapter 3. For the glass, the 3 mm layer thickness as the optimum value was used [68]. The EVA used as the encapsulated material has 300 µm thickness as the common thickness used for the encapsulation [76]. For the 4T tandem configurations, the EVA is also needed to bond the top and bottom cells. The thickness of the EVA is 30 µm [77].

Table 2. 1. The layer thicknesses of the tandem solar cells.

Layers	Thickness of each layer (nm)		
	Non optimized	After optimized	Encapsulated by glass
MgF_2	90	90	90
Glass (mm)	-	-	3
EVA $_{front}$ (µm)	-	-	300
SnO_2:F	650	220	220
TiO_2	50	45	45
Spiro-OMeTAD	350	50	50
ITO	75	75	75
EVA $_{int}$ (µm)	-	-	30
poly-Si (*n*)	30	30	30
poly-SiO_x (*n*)	30	30	30
poly-SiC_x (*n*)	30	30	30
SiO_2	1	1	1
c-Si (µm)	280	280	280
poly-Si (*p*)	30	30	30
poly-SiO_x (*p*)	30	30	30
poly-SiC_x (*p*)	30	30	30
ITO rear side	120	120	120
Ag (µm)	3	3	3

2.3. Method

In this section, the method of calculating the implied photo-current density (J_{ph}) is explained.

The absorption profiles were simulated using GenPro4. GenPro4 is a MATLAB-based program developed at Delft University of Technology [58]. It is an advanced optical model that combines wave optics and ray optics in a more flexible way [78]. From the absorption profiles of each layer, the implied photo-current density (J_{ph}) is calculated by using this formula:

$$J_{ph,i} = -q \int_{300\ nm}^{1200\ nm} Ai(\lambda)\Phi(\lambda)d\lambda \qquad (28)$$

Where q is the elementary charge, A_i is the absorption spectrum of i-th layer, Φ is the photon flux according to the AM1.5G solar spectrum and λ represents the wavelength. The maximum implied photo-current density for the top and bottom cells are calculated by using the absorption of the perovskite and c-Si layers, respectively.

2.4. Results

In this section, optical simulation results of the 2T, 3T and 4T perovskite/c-Si tandem solar cells are shown. Each configuration (2T, 3T and 4T) has three different results, i.e., before thickness optimization, after thickness optimization and encapsulated by the glass. The optical simulation results shown here are only for the tandem structure using poly-SiO_x as CSPCs. Meanwhile, for the tandem using poly-Si and poly-SiC_x as the CSPCs, the J_{ph} of the absorbers and optical losses of the CSPCs in each tandem structure will be presented in the conclusion session.

2.4.1. 2T perovskite/c-Si tandem solar cells

Figure 2. 6 (a), (b) and (c) are the optical simulation results for the fully textured 2T perovskite/c-Si tandem solar cells.

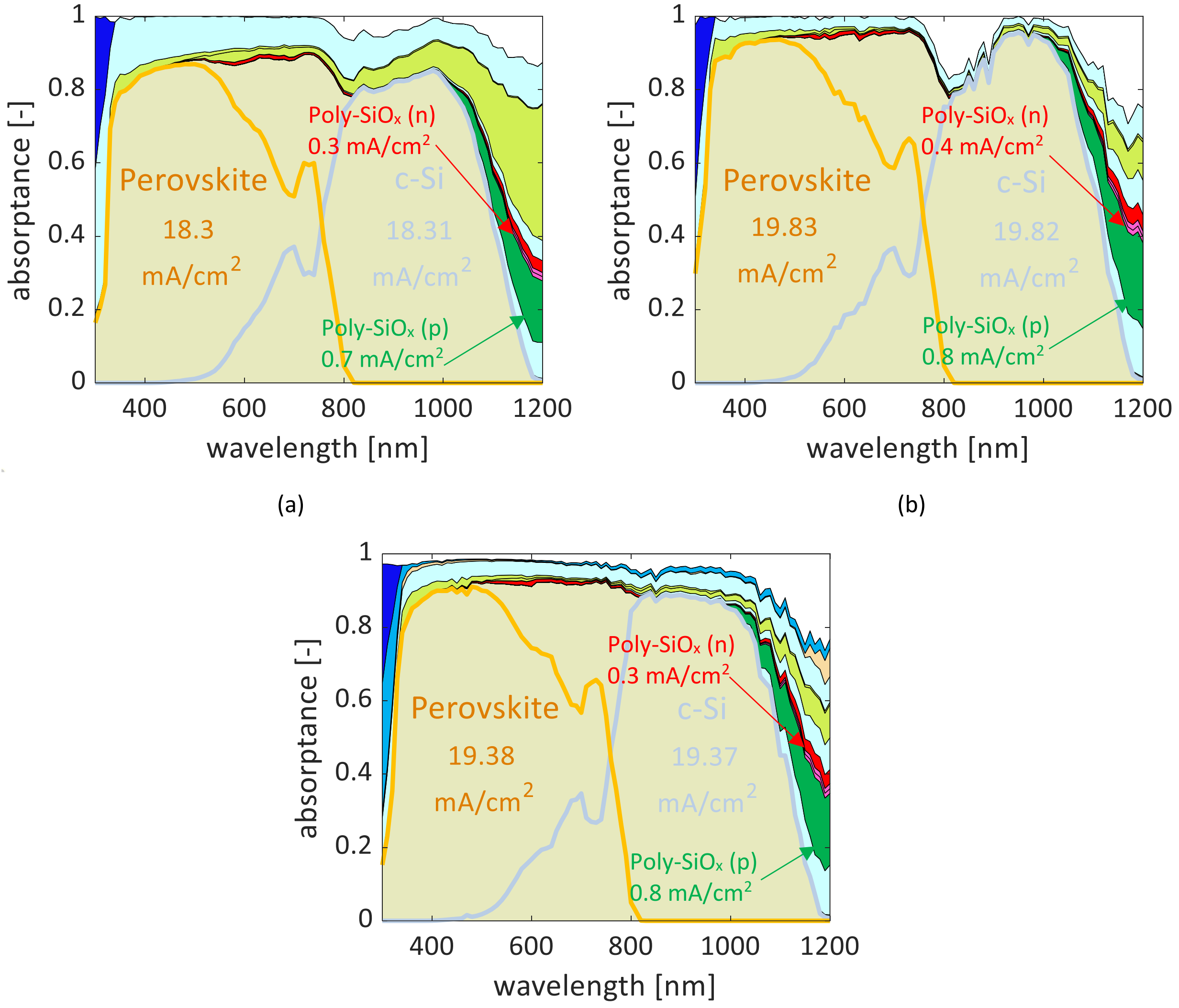

(a)

(b)

(c)

Figure 2. 6. Absorptance and reflectance of current matched 2T perovskite/c-Si tandem solar cells using poly-SiO$_x$ as CSPCs. (a). before thickness optimization, (b) after thickness optimization and (c) encapsulated by glass.

The description of the graph can be seen in Table 2. 2 below.

Table 2. 2. The description of the absorptance vs wavelength graph

Color of the area	Description
White	Total reflectance
Light beige	The absorptance that can be utilized from the absorber layers
Orange	Absorptance of the perovskite
Light grey	Absorptance of the c-Si
Dark blue	Parasitic absorptance in MgF_2
Light blue	Parasitic absorptance in ITO
Yellow	Parasitic absorptance in TiO_2
Light Green	Parasitic absorptance in Spiro-OMeTAD
Red	Parasitic absorptance in poly-SiO$_x$ (n)
Dark green	Parasitic absorptance in poly-SiO$_x$ (p)

Those graphs show the absorptance of each layer at a wavelength from 300 nm to 1200 nm. The absorption in the SiO_2 layer is so small, so it is not visible in the figure. The total losses can be obtained by adding the reflection losses and the total parasitic absorption losses.

Figure 2. 6 (a) shows the absorptances versus wavelength for the 2T perovskite/c-Si tandem solar cells before thickness optimization. Figure 2. 6 (b) shows the optical simulation result of the tandem structure after optimizing the layer thickness. Figure 2. 6 (c) is the optical simulation result of the tandem structure after adding a glass as an encapsulation material to make the tandem more realistic.

As can be seen in Figure 2. 6 (a), before the thickness of each layer being optimized, the parasitic absorption losses were very high. The SnO_2:F (indicated by light blue area) absorbs very high photons which lead to the parasitic absorption losses of 4.2 mA/cm^2. The second-largest loss happened in the Spiro-OMeTAD. It has parasitic absorption losses of 2.6 mA/cm^2. The reflection losses become the third place as it contributes to 1.1 mA/cm^2 (11.11% of the total losses). The interesting parts i.e. the poly-SiO_x (*n*) and (*p*) contribute the parasitic absorption losses of 0.3 mA/cm^2 (3.4% of the total parasitic absorption losses) and 0.7 mA/cm^2 (7.1% of the total parasitic absorption losses), respectively. Perovskite thickness of 224 nm was needed to achieve the current matching. As can be seen in Figure 2. 6 (a), it shows that the tandem structure can produce 18.30 mA/cm^2 of implied photo-current density. The J_{ph} result is higher because the two strategies of increasing the absorptance had been applied, i.e. adding MgF_2 as anti-reflection losses to reduce the reflection losses of the front interfaces and making the tandem structure fully textured. Based on the optical simulations, by adding an anti-reflective coating such as MgF_2, the J_{ph} can be increased by 6.7%.

Figure 2. 6 (b), the thickness of the top cell of the tandem was optimized. The optimum thickness of each layer can be seen in Table 2. 1. As can be seen in the figure, the parasitic absorption losses are much reduced. By changing the thickness of SnO_2:F from 650 nm to 220 nm, the parasitic absorption loss is decreasing from 4.2 mA/cm^2 to 1.6 mA/cm^2 (reduced by 61.9%). For the spiro-OMeTAD, as indicated by the light green area, by changing the thickness from 350 nm to 50 nm, the parasitic absorption losses are decreasing from 2.6 mA/cm^2 to 0.5 mA/cm^2 (reduced by 80.8%). The thickness of the bottom cells is kept the same, so the parasitic absorption losses of each layer of the bottom cells remain the same. The perovskite thickness of 217 nm is needed to get the current matching. It is 7 nm thinner than the perovskite layer in the tandem structure before thickness optimization. The implied photo-current density of the tandem after current matching is 19.82 mA/cm^2. It is increased by 8.3% after thickness optimization. As shown in Figure 2. 6 (b), by optimizing the FTO layer, photons' absorptance in the perovskite layer at a wavelength of 350 nm to 650 nm is increasing. The absorptance of c-Si at a wavelength of 810 nm to 1050 nm is also increasing by optimizing the SnO_2:F and spiro-OMeTAD layers. However, the thickness optimization of the tandem structure also leads to the increase of the reflection losses, especially at the interface between the perovskite and c-Si and at the rear side. The increasing of the reflection losses due to the number of photons that were originally absorbed by the coatings as parasitic absorption losses are being reflected back into the air.

Figure 2. 6 (a) and (b) show the optical simulation results of the 2T perovskite/c-Si tandem solar cells before and after thickness optimization. Nevertheless, those values are not realistic enough because, in reality, the module needs to be encapsulated [68] [69]. The encapsulation is needed to prevent the module from environmental damage. So to make it realistic, the tandem is encapsulated by glass and EVA. EVA is used to join the tandem structure to the glass. It is also used to protect the PV materials from the environment and mechanical damage [69]. The optical simulation results are shown in Figure 2. 6 (c).

The azure coloured area indicated the parasitic absorptance losses of the glass. The beige coloured area represents the parasitic absorption losses of the EVA. The parasitic absorptance values of these two layers are 0.5 mA/cm^2 and 0.2 mA/cm^2, respectively. By encapsulated the tandem with the glass and EVA, there is an increase in the absorptance in perovskite and c-Si at the wavelength of 740 nm to 940 nm. The implied photo-current density of this structure after the current matching is 19.37 mA/cm^2. The encapsulation leads to the decreasing of the J_{ph} by 2.3%. The total reflection losses by implementing the glass and EVA on the tandem structure is 2.1 mA/cm^2 (26.9% of the total losses). The total parasitic absorption losses of this structure are 5.7 mA/cm^2. The highest parasitic absorption losses are occurred in the SnO_2:F layer with 2 mA/cm^2 (35.1% of the total parasitic absorption losses). The poly-SiO_x (*n* and *p*) have the parasitic absorption value of 0.3 mA/cm^2 (5.3% of the total parasitic absorption losses) and 0.8 mA/cm^2 (14.04% of the total parasitic absorption losses), respectively. The perovskite layer thickness of 194 nm is needed to get the current matching. If it is compared with the result published by Fsahli et al. (19.5 mA/cm^2), the implied photo-current density of 19.37 mA/cm^2 produced by this tandem structure is a very good result for the 2T perovskite/c-Si tandem solar cells, but it should be underlined that this result is only from the optical perspective [79]. The electrical simulations are needed to get the J_{sc}, V_{oc}, *FF* and η, after that the results can be fairly compared.

2.4.2. 3T perovskite/c-Si tandem solar cells

In this subsection, the optical simulation results of the 3T perovskite/c-Si tandem solar cells are explained. The simulations have the following purposes: First, to know how much the J_{ph} can be produced from the 3T perovskite/c-Si tandem structure using the new bottom cell structure; second, to minimize the optical losses of the tandem structure by optimizing the layer thickness and the third, to have the realistic tandem structure by encapsulated it with glass. The optical simulations results of the 3T perovskite/c-Si tandem solar cells are shown in Figure 2.7 below.

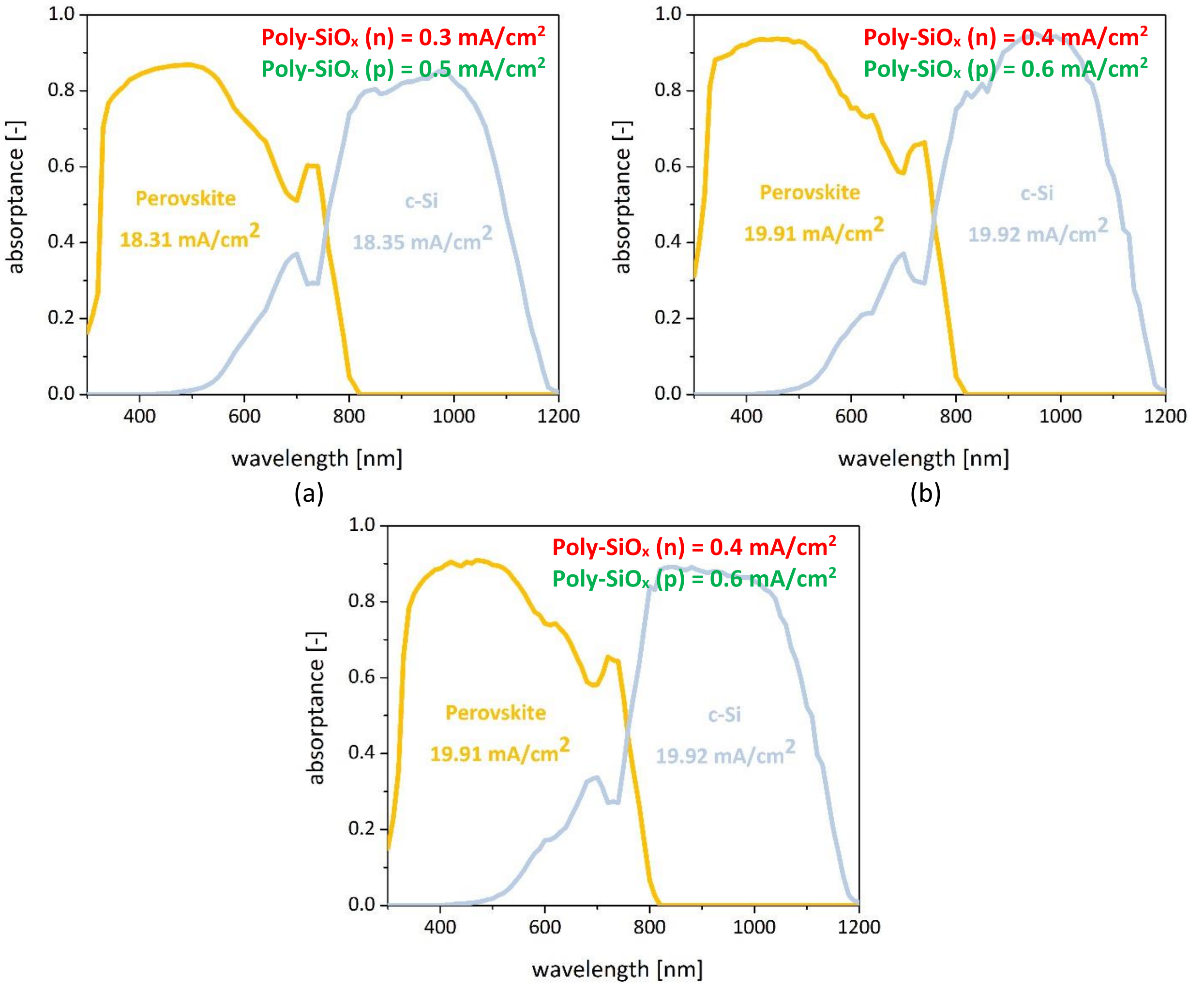

(a) (b)

(c)

Figure 2.7. Absorptance and reflectance of current matched 3T perovskite/c-Si tandem solar cells using poly-SiO_x as CSPCs. (a). before thickness optimization, (b) after thickness optimization and (c) encapsulated by the glass.

Figure 2.7 (a) shows the absorptance versus wavelength of the 3T tandem structure before thickness optimization. The implied photo current density of the perovskite and c-Si are 18.31 mA/cm^2 and 18.35 mA/cm^2, respectively. The J_{ph} of each absorber is obtained by multiply the J_{ph} of each absorber with the area of the contacts. As can be seen in Figure 2. 2, the area of the *p* and *n* contacts are 70% and 20%, respectively [80]. The perovskite layer thickness used in here is kept the same with the perovskite layer thickness in 2T tandem. The purpose of this is to know how much the implied photo-current density generated by the 3T tandem structure using the same absorber thickness as in 2T. The parasitic absorptance losses of the poly-SiO$_x$ layers (*n* and *p*) in Figure 2.7 (a) are 0.3 mA/cm^2 and 0.5 mA/cm^2, respectively.

Figure 2.7 (b) presents the optical simulations results of the 3T perovskite/c-Si tandem solar cells after thickness optimization. The implied photo-current density of the perovskite and c-Si are 19.91 mA/cm^2 and 19.92 mA/cm^2, respectively. The parasitic absorptance losses of the poly-SiO$_x$ layers (*n* and *p*) in this structure are 0.4 mA/cm^2 and 0.6 mA/cm^2, respectively. In the 3T tandem structure, there are two contacts in the rear side. These contacts allow the tandem cells to utilize the implied photo-current density optimally.

Figure 2.7 (c) shows the optical simulations results of the 3T tandem structure encapsulated by glass and EVA. The implied photo-current density of the perovskite and c-Si are 19.39 mA/cm^2 and 19.45 mA/cm^2, respectively. The J_{ph} of the absorbers are slightly lower than the result in Figure 2.7 (b), it is because the glass and EVA absorb the photons and lead to the additional parasitic absorption losses in the structure. Based on the optical simulations, for the same case, the total implied photo-current density of the absorbers in 3T is slightly higher than in 2T (0.14% higher for the non-optimized thickness structure, 0.45% higher for the optimized thickness structure and 0.23% higher for the encapsulated with glass).

2.4.3. 4T perovskite/c-Si tandem solar cells

In the previous two subsections, it has been explained how much J_{ph} can be produced in the 2T and 3T perovskite/c-Si tandem solar cells using poly-SiO$_x$ as carrier-selective passivating contacts. In this subsection, the optical simulation results of the 4T configuration using poly-SiO$_x$ as carrier-selective passivating contacts will be presented.

Before explaining further about the optical simulation results, the 4T tandem structure has a slight difference from the tandem structure. As can be seen in Figure 2. 3, the 4T tandem structure requires an additional ITO layer to the rear side of the top cells as well as the front side of the bottom cells. The ITO is necessary because in 4T configurations, the top cell and bottom cell are acting as individual cells, thus requiring additional TCO as the solar cell's electric contact. Apart from the ITO, the EVA (Ethylene Vinyl Acetate) layer is also added between the top and bottom cells. It acts as a glue to bind the top cell and bottom cell structures [69].

The tandem structure has a double side textured bottom cell. As shown in Figure 2. 8, the optical simulation results for the non-encapsulated structure is not presented. Normally, for the 4T tandem configuration, the tandem is encapsulated by glass [34] [75].

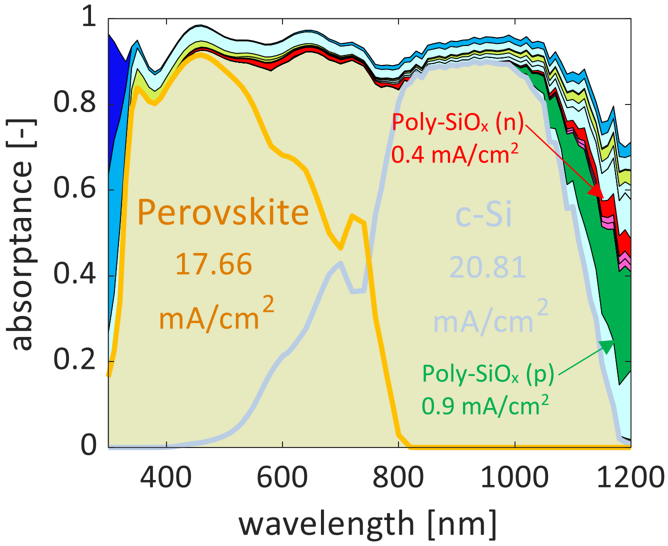

Figure 2. 8. Absorptance and reflectance of current matched 4T perovskite/c-Si tandem solar cells using poly-SiO$_x$ as CSPCs.

The implied photo-current density of the perovskite and c-Si are 17.66 mA/cm^2 and 20.81 mA/cm^2, respectively. The perovskite thickness is kept the same as the perovskite layer thickness in the 2T tandem structure i.e. 194 nm. The total reflection loss of this structure is 3.2 mA/cm^2 whereas the total parasitic absorption loss of this structure are 4.8 mA/cm^2. The parasitic absorption of the glass is 0.5 mA/cm^2, whereas the parasitic absorption of the EVA layer is so small (2.3E-4 mA/cm^2) so that the value is not showed up in the figure. The highest parasitic absorption is occurred in the SnO_2:F layer with the value of 1.1 mA/cm^2 (22.9% of the total parasitic absorption losses). Until know, the journal that has been published related to the 4T perovskite/c-Si tandem are using flat type for the top cell structure [72] [73] [74] [34] [75].

2.5. Discussion

In this section, all-optical simulation results of the 2T, 3T and 4T perovskite/c-Si tandem solar cells using different carrier-selective passivating contacts (poly-Si, poly-SiC$_x$ and poly-SiO$_x$) are shown.

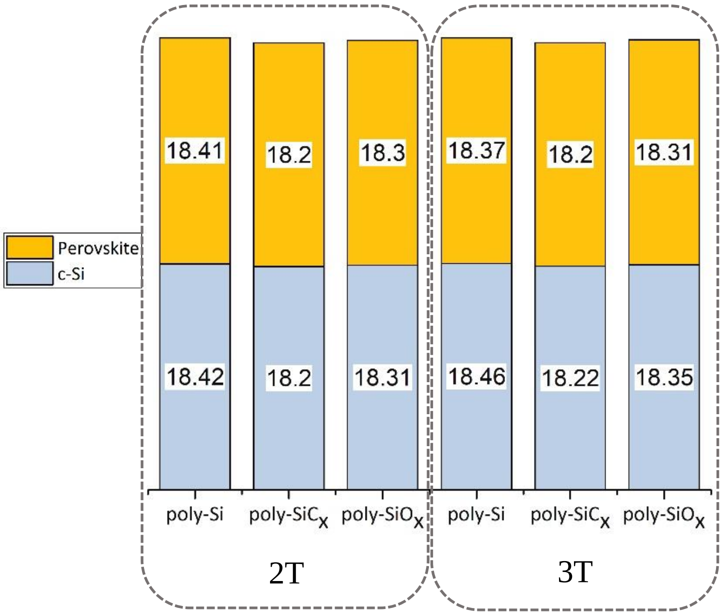

Figure 2.9. The J_{ph} (mA/cm^2) of fully textured 2T and 3T perovskite/c-Si tandem solar cells before thickness optimization.

Figure 2.9 shows the implied photo-current density of the 2T and 3T perovskite/c-Si tandem solar cells before thickness optimization using poly-Si, poly-SiC$_x$ and poly-SiO$_x$ as carrier-selective passivating contacts. For both configurations, the highest total implied photo-current density was achieved by using poly-Si as the carrier-selective passivating contacts. For the 2T configuration, the highest total implied photo-current density can be achieved is 36.78 mA/cm^2, but because the top cell and bottom cell are connected in series, so the implied photo-current density generated by the tandem structure is limited by the cell that produces lower implied photo-current density, i.e. 18.37 mA/cm^2. For the 3T configuration, the highest total implied photo-current density is slightly higher than the 2T configuration (0.14% higher), but in 3T, the current matching is not required. The subcells can be operated independently at their maximum power point (MPP) [39]. The second-highest total implied photo-current density was achieved by using poly-SiO$_x$ as carrier-selective passivating contacts. Comparing with the tandem structure using poly-Si as the carrier-selective passivating contacts, the difference was so small i.e. 0.60% for 2T and 0.46% for 3T. In terms of performance, the poly-SiO$_x$ has more advantages than poly-Si such as the crystallinity and the absorption coefficient can be adjusted by varying the oxygen content during material deposition and the bandgap also can be widened, so it can be transparent for longer wavelength [47]. Whereas, the poly-Si is not transparent, especially when it is doped heavily. It parasitically absorbs the amount of light in the form of free-carrier absorption [47].

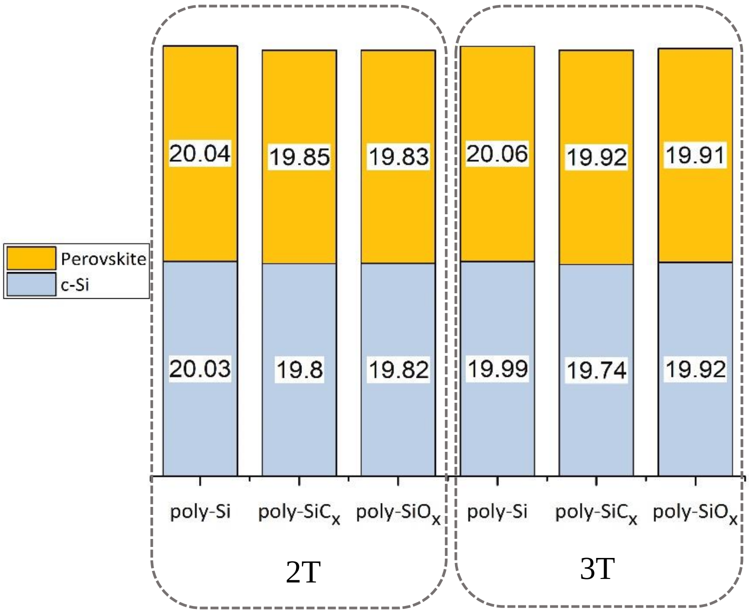

Figure 2.10. The J_{ph} (mA/cm^2) of fully textured 2T and 3T perovskite/c-Si tandem solar cells after thickness optimization.

Figure 2.10 shows the implied photo-current density of the 2T and 3T perovskite/c-Si tandem solar cells after optimizing layer thicknesses. As can be seen from the figure, the implied photo-current density of 2T perovskite/c-Si tandem using poly-Si, poly-SiC$_x$ and poly-SiO$_x$ are 20.03 mA/cm^2, 19.80 mA/cm^2 and 19.82 mA/cm^2, respectively. Comparing with Figure 2.9, the increase of the J_{ph} of the tandem using poly-Si, poly-SiC$_x$ and poly-SiO$_x$ after thickness optimization are 8.79%, 8.79% and 8.31%, respectively. Whereas for the 3T tandem configuration, after optimizing layer thicknesses, the increasing of the total implied photo-current density of the 3T tandem structure using poly-Si, poly-SiC$_x$ and poly-SiO$_x$ are 8.74%, 8.89%, 8.65%, respectively.

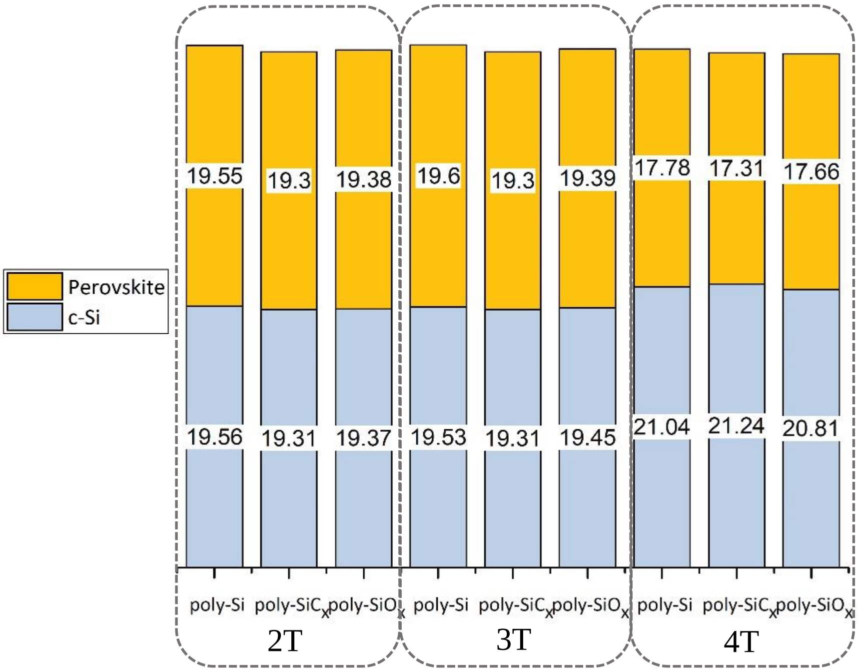

Figure 2.11. The J_{ph} (mA/cm^2) of 2T, 3T and 4T perovskite/c-Si tandem solar cells after encapsulated by glass.

After optimization, to make the tandem more realistic, the tandem should be encapsulated with glass and EVA. The optical simulation results of the 2T, 3T and 4T perovskite/c-Si tandem solar cells after encapsulation are shown in Figure 2.11. The implied photo-current density after current matching for 2T tandem using poly-Si, poly-SiC$_x$ and poly-SiO$_x$ are 19.55 mA/cm^2, 19.30 mA/cm^2 and 19.37 mA/cm^2, respectively. Comparing with the 2T results in Figure 2.10, the decreasing of the J_{ph} after adding the encapsulation materials is up to 2.5%.

For the 3T tandem, the total implied photo-current density of the tandem structure after encapsulation by using poly-Si, poly-SiC$_x$ and poly-SiO$_x$ are 39.13 mA/cm^2, 38.61 mA/cm^2 and 38.84 mA/cm^2, respectively. The difference between the J_{ph} results compared with Figure 2.10 is up to 2.6%.

The optical simulation results of the 4T perovskite/c-Si tandem solar cells using different carrier-selective passivating contacts are also shown in Figure 2.11. For the 4T configuration, the top cell structure is flat because considering the fabrication visibility [34]. It also uses glass and EVA to make it realistic. As can be seen in Figure 2.11, the 4T tandem has the lowest total implied photo-current density compared with the 2T and 3T. It clearly shows that the main difference is in the J_{ph} values produced by the perovskite. The absorption in perovskite is lesser because the structure of the top cell is flat, so the coupling of light is not as high as the textured surface. From the optical simulations using GenPro4, the total implied photo-current density of 4T perovskite/c-Si tandem solar cells using poly-Si, poly-SiC$_x$ and poly-SiO$_x$ are 38.82 mA/cm^2, 38.55mA/cm^2 and 38.47 mA/cm^2, respectively.

2.6. Conclusion

The purpose of this section is to answer the first research question about how much the optimum and realistic implied photo-current density (J_{ph}) can be produced by the 2T, 3T and 4T perovskite/c-Si tandem solar cells structure and also the optical losses of CSPCs in each optimum structure. To reach an optimum and realistic phase, the main research questions have been divided into three sub-questions as follow:

- How much the implied photo-current density produced of the 2T, 3T and 4T perovskite/c-Si tandem solar cells before thickness optimization?

- How much the implied photo-current density produced by the 2T, 3T and 4T perovskite/c-Si tandem solar cells after thickness optimization?
- How much the implied photo-current density of 2T, 3T and 4T perovskite/c-Si tandem solar cells after encapsulated by the glass?

The first sub-question has been answered and can be seen in Figure 2.9. The implied photo-current density for the 2T and 3T before thickness optimization and the optical losses in CSPCs are shown in Table 2. 3 below.

Table 2. 3. The summary of optical simulations of 2T and 3T perovskite/c-Si tandem solar cells before thickness optimization.

	Using poly-Si as CSPCs				Using poly-SiC$_x$ as CSPCs				Using poly-SiO$_x$ as CSPCs			
	J_{ph} (mA/cm^2)		Parasitic Absorption (mA/cm^2)		J_{ph} (mA/cm^2)		Parasitic Absorption (mA/cm^2)		J_{ph} (mA/cm^2)		Parasitic Absorption (mA/cm^2)	
	Perovskite	c-Si	Poly-Si (*n*)	Poly-Si (*p*)	Perovskite	c-Si	Poly-SiC$_x$ (*n*)	Poly-SiC$_x$ (*p*)	Perovskite	c-Si	Poly-SiO$_x$(*n*)	Poly-SiO$_x$ (*p*)
2T	18.41	18.42	0.2	0.1	18.20	18.20	0.5	0.2	18.30	18.31	0.3	0.7
3T	18.37	18.46	0.2	0.1	18.20	18.22	0.5	0.1	18.31	18.35	0.3	0.5

The answer to the second sub-question has been revealed in Figure 2.10. The summary of the optical simulation results can be seen in Table 2. 4 below.

Table 2. 4. The summary of optical simulations of 2T and 3T perovskite/c-Si tandem solar cells after thickness optimization.

	Using poly-Si as CSPCs				Using poly-SiC$_x$ as CSPCs				Using poly-SiO$_x$ as CSPCs			
	J_{ph} (mA/cm^2)		Parasitic Absorption (mA/cm^2)		J_{ph} (mA/cm^2)		Parasitic Absorption (mA/cm^2)		J_{ph} (mA/cm^2)		Parasitic Absorption (mA/cm^2)	
	Perovskite	c-Si	Poly-Si (*n*)	Poly-Si (*p*)	Perovskite	c-Si	Poly-SiC$_x$ (*n*)	Poly-SiC$_x$ (*p*)	Perovskite	c-Si	Poly-SiO$_x$(*n*)	Poly-SiO$_x$ (*p*)
2T	20.04	20.03	0.2	0.1	19.85	19.80	0.6	0.2	19.83	19.82	0.4	0.8
3T	20.06	19.99	0.2	0.1	19.92	19.74	0.6	0.1	19.91	19.92	0.4	0.6

The J_{ph} value for the 2T, 3T and 4T perovskite/c-Si tandem solar cells after encapsulation and also the optical losses in poly-Si, poly-SiC$_x$ and poly-SiO$_x$ as the answers for the third sub-question are shown in Table 2. 5 below.

Table 2. 5. The summary of optical simulations of 2T, 3T and 4T perovskite/c-Si tandem solar cells after thickness optimization and encapsulation.

	Using poly-Si as CSPCs				Using poly-SiC$_x$ as CSPCs				Using poly-SiO$_x$ as CSPCs			
	J_{ph} (mA/cm^2)		Parasitic Absorption (mA/cm^2)		J_{ph} (mA/cm^2)		Parasitic Absorption (mA/cm^2)		J_{ph} (mA/cm^2)		Parasitic Absorption (mA/cm^2)	
	Perovskite	c-Si	Poly-Si (*n*)	Poly-Si (*p*)	Perovskite	c-Si	Poly-SiC$_x$ (*n*)	Poly-SiC$_x$ (*p*)	Perovskite	c-Si	Poly-SiO$_x$(*n*)	Poly-SiO$_x$ (*p*)
2T	19.55	19.56	0.2	0.1	19.30	19.31	0.5	0.2	19.38	19.37	0.3	0.8
3T	19.60	19.53	0.2	0.1	19.30	19.31	0.5	0.1	19.39	19.45	0.4	0.6
4T	17.78	21.04	0.3	0.1	17.31	21.24	0.7	0.2	17.66	20.81	0.4	0.9

The main research question about finding the optimum and realistic J_{ph} of 2T, 3T and 4T perovskite/c-Si tandem and also the optical losses of CSPCs in each optimum structure can be known by referring to Table 2. 5. As can be seen in Table 2. 5, the optimum and realistic J_{ph} of 2T, 3T and 4T perovskite/c-Si tandem are obtained by using poly-Si as CSPCs. For the 2T tandem configuration, the J_{ph} after current matching is 19.55 mA/cm^2, whereas the optical losses in poly-Si (*n*) and (*p*) of that structure are 0.2 mA/cm^2 and 0.1 mA/cm^2, respectively. For the 3T tandem configuration, the J_{ph} of the perovskite and c-Si are 19.60 mA/cm^2 and 19.53 mA/cm^2, respectively. The optical losses in poly-Si (*n*) and (*p*) of the optimum 3T tandem are 0.2 mA/cm^2 and 0.1 mA/cm^2, respectively. For the 4T tandem configuration, the J_{ph} of the perovskite and c-Si are 17.78 mA/cm^2 and 21.04 mA/cm^2, respectively and the optical losses in poly-Si (*n*) and (*p*) of the optimum 4T tandem are 0.3 mA/cm^2 and 0.1 mA/cm^2, respectively.

3. Optimization of the perovskite solar cell

This chapter answers the second research question introduced in section 1.10 which is “How much is the efficiency of the top cell (perovskite solar cells) after optimization?” It also quantifies the value of the optimized parameters and shows the sensitivity analysis. The simulation parameters are explained in section 3.2, the comparison with experimental data is explained in section 3.3, the optimization parameters are presented in section 3.4, the results and discussion are shown in section 3.5 and the conclusions are present in section 3.6.

5.1. Introduction

In order to optimize the 2T perovskite/c-Si tandem solar cell, first, the bottom cell (c-Si solar cell in this case) and the top cell (perovskite solar cell in this case) are optimized separately. This optimization aims to produce optimized perovskite/c-Si tandem solar cells whose performance is close to optimal performance. This chapter focuses on top cell optimization. The optimized parameters of the bottom cell are present in the next chapter. To obtain a clear understanding of the optimization process, the optimization process flow is presented in Figure 3.1.

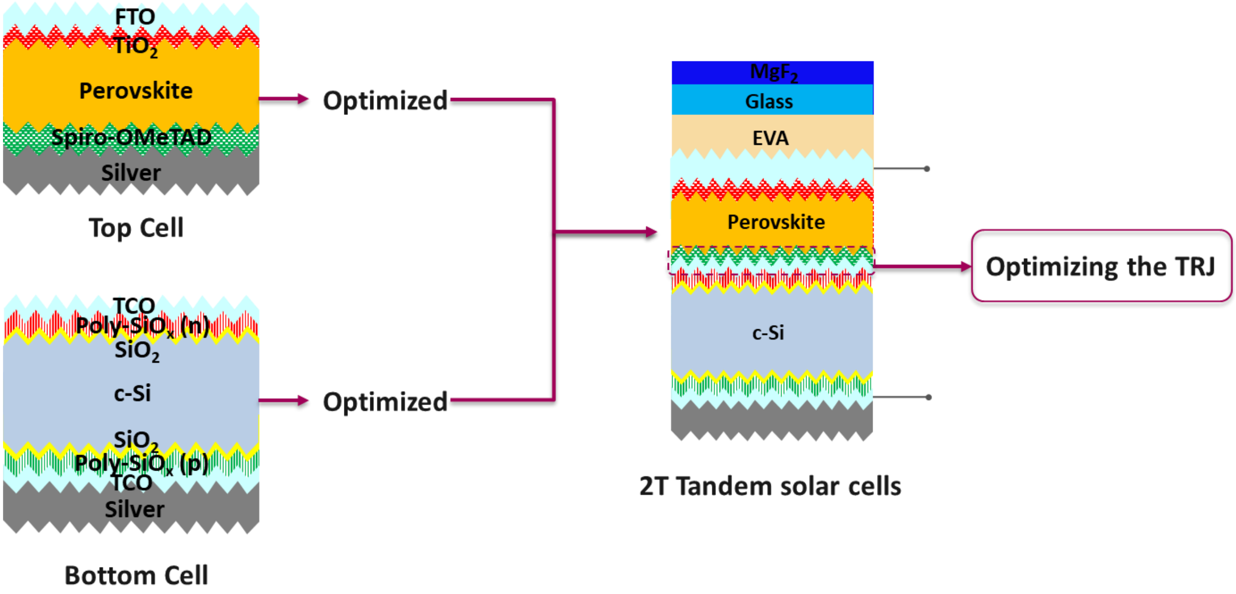

Figure 3.1. Optimization process flow of 2T perovskite/c-Si tandem solar cell

As shown in Figure 3.1, the first step is optimizing the top and bottom cells separately. These optimized parameters are used in a perovskite/c-Si 2T tandem configuration along with the anti-reflective and encapsulation materials. The final step of this work is optimizing the tunnel recombination junction of the 2T tandem by changing the doping of the (electron transporting layer) TCO and hole transporting layer (Spiro-OMeTAD). This has been explained in chapter 4.

The perovskite structure used as the top cell is taken from [67]. It has various advantages over the commonly used perovskite ($MAPbI_3$), including a better charge collection efficiency and reproducibility

[27] [66]. The perovskite has also been successfully manufactured in the lab, with 15.4% efficiency [67]. The perovskite structure used in the simulation is shown in Figure 3.2.

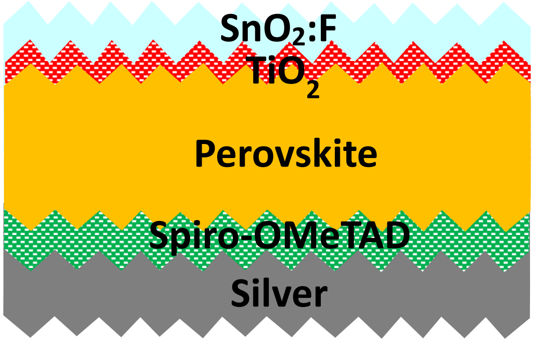

Figure 3.2 Simulated structure of the top cell

Figure 3.2 shows the simulated structure of the top cell that consists of 650 nm fluorine-doped tin oxide (FTO), 50 nm titanium dioxide (TiO_2) as the electron transporting layer, 330 nm methylammonium lead tri-iodide perovskite with a mixed halide ($CH_3NH_3PbI_{3-x}Cl_x$), 350 nm Spiro-OMeTAD as the hole transporting layer and 200 nm silver as the back metal.

3.2. Model and parameters

The material parameters of the top cell are obtained from [67]. The parameters are shown in Table 3.1. The complex refractive index (*n*) and the extinction coefficient (*k*) of each material are shown in Figure 2. 4 (a) and (b).

Table 3.1. Simulation parameters of the top cell [67]

Parameters	Unit	SnO_2:F (FTO)	TiO_2	$CH_3NH_3Pb_{3-x}Cl_x$	Spiro-OMeTAD
Thickness	nm	650	50	330	350
Doping	cm^{-3}	2×10^{19}	1×10^{16}	2×10^{16}	2×10^{18}
Mobility (μ_e/μ_h)	cm^2/Vs	20/10	20/10	1.62	$2 \times 10^{-4}/2 \times 10^{-4}$
Dielectric constant	-	9	9	6.5	3
Band gap	eV	3.5	3.2	1.55	3
Electron affinity	eV	4	4	3.9	2.45
Holes lifetime	s	1×10^{-6}	1×10^{-6}	2.88×10^{-7}	1×10^{-6}
Electron lifetime	s	1×10^{-5}	1×10^{-5}	2.88×10^{-7}	1×10^{-5}
Conduction density	cm^{-3}	2.2×10^{18}	2.2×10^{18}	4.42×10^{17}	2.2×10^{18}
Valence density	cm^{-3}	1.8×10^{19}	1.8×10^{19}	8.47×10^{18}	1.8×10^{19}
Radiative coefficient	$cm^3\ s^{-1}$	-	-	2×10^{-10}	-
Auger coefficient	$cm^6\ s^{-1}$	-	-	9.9×10^{-29}	-

The surface recombination velocity (SRV) for the interface between TiO_2 and $CH_3NH_3Pb_{3-x}Cl_x$ is 3500 cm/s whereas the SRV for the interface between $CH_3NH_3Pb_{3-x}Cl_x$ and Spiro-OMeTAD is 100 cm/s [67].

The optical and electrical simulation models from the literature [67] have been used in Sentaurus TCAD. The physics models used in the electrical simulations are shown in Table 3. 2 below.

Table 3. 2. Summary of the physics models used for electrical simulations

Device Modelling	
Model	**Description**
Carrier transport	Drift-diffusion model
The effect of interface defect	Surface recombination velocity
Recombination	SRH recombination
	Auger recombination
	Radiative recombination
Heterostructure device simulation	Thermionic emission
Doping	Phosphorous and boron constant profile

The simulations were performed under the one sun AM1.5G spectrum [67].

3.3. Comparison with experimental data

Before doing the optimization, all the material parameters, including the n and k data, were given as inputs and simulated in Sentaurus TCAD. The idea was to check the models used in simulation and to compare the simulated J-V with the experimental J-V [67].

The simulation result is shown in Figure 3.3. It shows the comparison of the experimental J-V obtained from [67] with simulated J-V. As can be seen in Figure 3.3, the simulated J-V is quite similar to the experimental J-V.

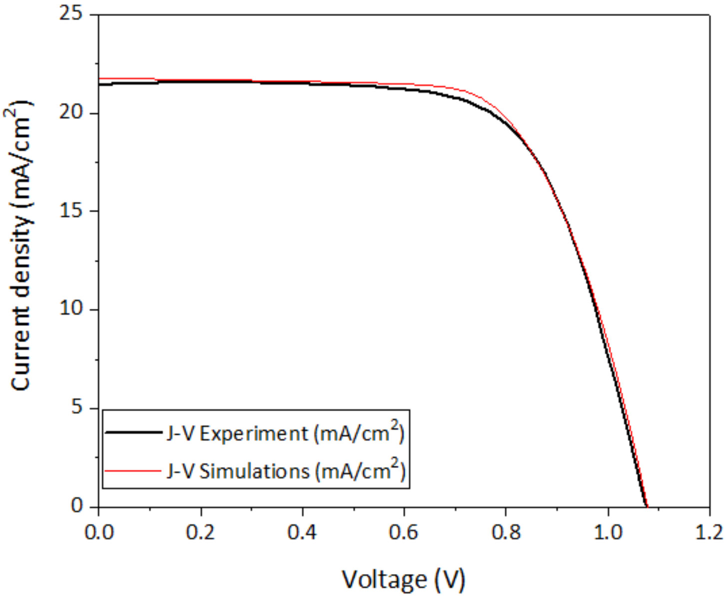

Figure 3.3. The comparison of experimental J-V with simulated J-V

The output parameters of the experiment [67] and simulations from Sentaurus TCAD are shown in Table 3.3 below. These simulation results were used as the starting point for the optimization of the top cell (perovskite solar cells).

Table 3.3. The comparison of top cell performance parameters from the experiment [67] and simulations

Top Cell	**Output**			
	J_{sc} (mA/cm^2)	V_{oc} (V)	FF (%)	η (%)
Experiment	21.5	1.07	67	15.41
Simulations	21.75	1.078	67.51	15.83

3.4. Optimized parameters

The parameters of the top cell that are optimized are the contact resistance, surface recombination velocity of the interface between TiO_2 and perovskite and thickness of each layer. These parameters were chosen to be optimized due to the following reasons:

1. The Fill factor is influenced by high series resistance. Therefore, the optimization of the contact resistance is needed to increase the efficiency of the top cells. The idea is to have the fill factor > 80%, similar to the second-highest efficiency of the perovskite solar cells reported in the world [81].
2. The SRV of the interface between TiO_2 and perovskite (front interface) is the second parameter to be optimized. The reason is due to the higher SRV value reported in the literature for this interface. Therefore the probability of the generated carriers to recombine in this interface is higher than in the back interface. The V_{oc} is highly affected by the recombination. Thus the SRV of the front interface needs to be optimized [67].
3. Thickness of each layer has also been optimized. This is essential as the thickness affects the parasitic absorption and the recombination in the solar cell. The optimum thickness is one of the requirements to achieve the high performance of the solar cell [82].

3.5. Result and discussion

In this section, the effect of optimizing the contact resistance, surface recombination velocity between the TiO_2 and perovskite interface and also the thickness of FTO, TiO_2, $CH_3NH_3Pb_{3-x}Cl_x$ and Spiro-OMeTAD on the J_{sc}, V_{oc}, FF and η are explained in detail.

3.5.1. Contact resistance optimization

Contact resistance is the first optimization parameter. In literature [67], the value of contact resistance has not been reported. The contact resistance value is obtained by comparing the simulated *J-V* from Sentaurus TCAD with the experimental *J-V* [67]. From the simulation, the contact resistance values of the front and back contacts obtained are 2.2 Ω. cm^2 and 2.2 Ω. cm^2, respectively. These values are further optimized to get a higher fill factor. The simulation results are shown in Figure 3.4.

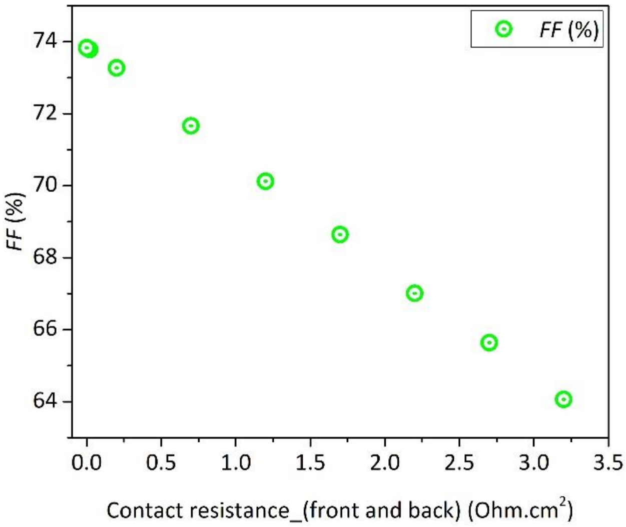

Figure 3.4. The effect of contact resistance on fill factor by varying the front and back contact resistance using the same value.

Figure 3.4 shows the effect of the front and back contact resistance on the fill factor. As expected, by increasing the contact resistance value, the fill factor is decreasing. By optimizing the contact resistance, the fill factor can be increased from 67.51% to 73.83%.

3.5.2. Surface recombination velocity optimization

The second parameter that is optimized is surface recombination velocity between TiO_2 and perovskite interface. In the simulations, the optimum value of contact resistance was used. The default value of the SRV between TiO_2 and $CH_3NH_3Pb_{3-x}Cl_x$ interface is 3500 cm/s. The SRV then varied from 100 cm/s to 3500 cm/s. The simulation results are shown in Figure 3. 5.

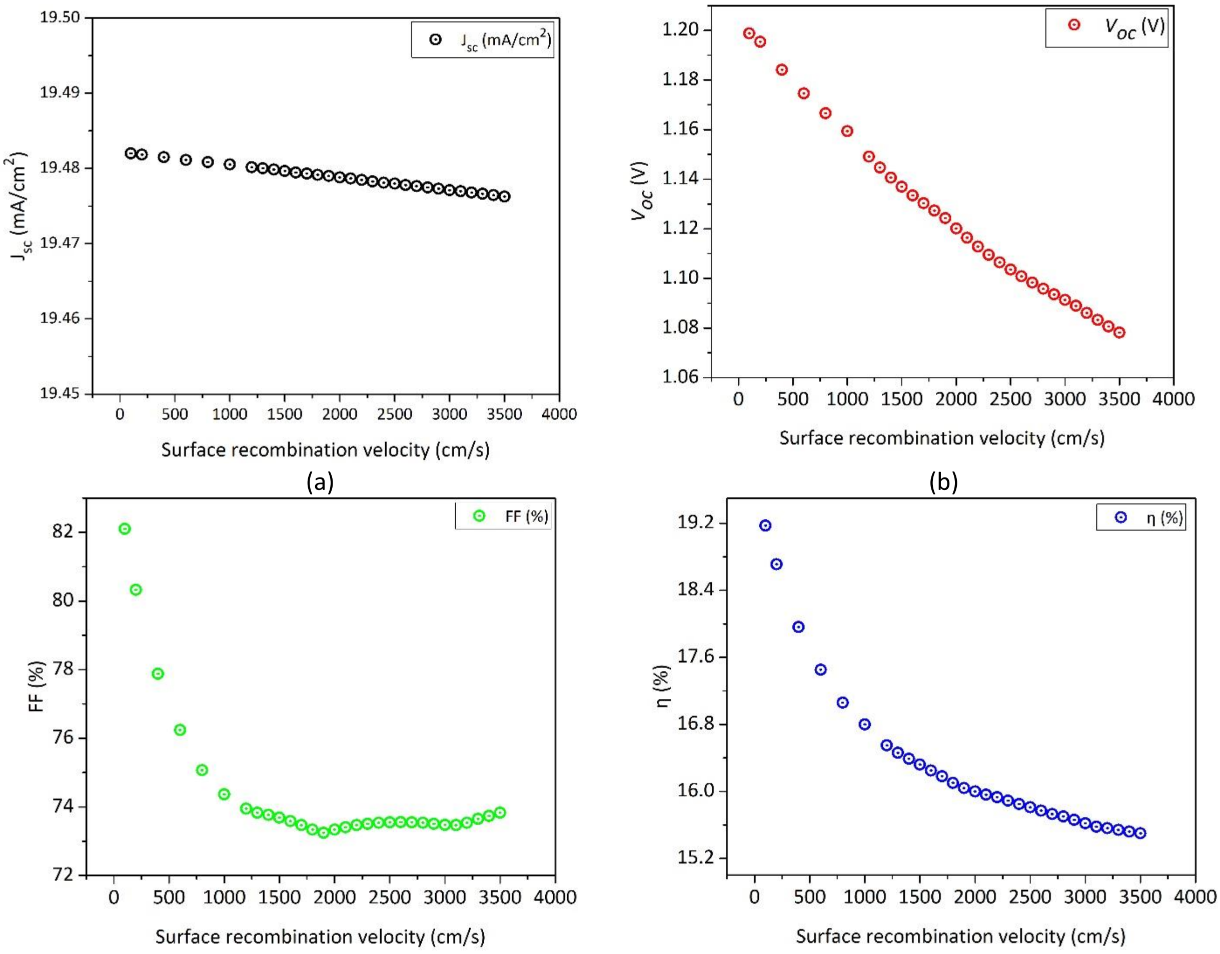

(a) (b)

(c) (d)

Figure 3. 5. The effect of surface recombination velocity on (a) J_{sc} (mA/cm^2), (b) V_{oc} (V), (c) FF (%) and (d) η (%)

Figure 3. 5 (a), (b), (c) and (d) show the effect of the surface recombination velocity on J_{sc}, V_{oc}, FF and η, respectively. J_{sc} of the perovskite solar cells is not significantly affected by the change in the SRV value. This can be seen in Figure 3. 5 (a). As expected in Figure 3. 5 (b), the V_{oc} is decreasing by increasing the SRV. Figure 3. 5 (c) shows the relationship between the SRV and FF values. As shown in this figure, by increasing the SRV value, the FF of the device decreases. If we refer to the V_{oc} value in Figure 3. 5 (b), it also shows that the V_{oc} value decreases with the increase in the SRV value. Referring to the solar energy book [83], it is stated that the decrease in the V_{oc} value will lead to the decreasing of FF, although the decrease is not significant.

Efficiency is a dependent parameter. The efficiency value will depend on the J_{sc}, V_{oc} and FF. As shown in Figure 3. 5 (d), by increasing the SRV, the top cell's efficiency is also decreasing. This trend is kind of expected, but from the simulation the optimum efficiency can be quantified. From the SRV optimization, the optimum SRV of 100 cm/s was chosen. The Fill factor is increasing from 73.83% to 82.1%. The efficiency can be increased from 15.5% to 19.17%. This value has been chosen as it can be implemented experimentally [67].

3.5.3. Thickness optimization

In this section, the result of the thickness optimization of each layer has been presented and explained in detail.

Perovskite thickness

In this subsection, perovskite thickness has been optimized. The optimum thickness will lead to the high performance of the solar cells, therefore it plays a crucial role [82]. The optimum value of the contact resistance and the optimum value of surface recombination velocity between TiO_2 and perovskite interface was used in the simulations. The perovskite thickness was also varied from 130 nm to 2030 nm. The default thickness of perovskite from the literature is 330 nm. The simulation results are shown in Figure 3. 6 below.

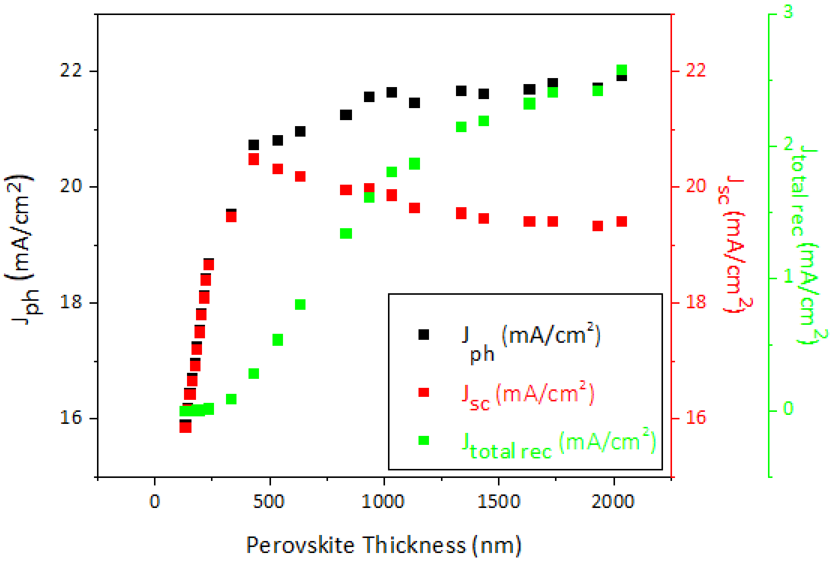

Figure 3. 6. The effect of perovskite thickness on J_{ph} (mA/cm^2), Jsc (mA/cm^2) and $J_{total\ recombination}$ (mA/cm^2)

Figure 3. 6 shows the effect of perovskite thickness of the implied photo-current density (J_{ph}), short circuit current density (J_{sc}) and total recombination current density ($J_{total\ recombination}$). The J_{ph}, J_{sc} and $J_{total\ recombination}$ are indicated by the black dots, red dots and green dots respectively. The green axis on the right-hand side is the axis for the $J_{total\ recombination}$. The relation of the J_{ph}, J_{sc} and $J_{total\ recombination}$ can be seen in the following formula:

$$J_{ph} = J_{sc} + J_{total\ recombination} \tag{29}$$

Total recombination current density is the sum of the recombination current densities associated with all the generation-recombination processes in the top cell.

$$J_{total\ recombination} = J_{SRH} + J_{Auger} + J_{radiative} + J_{surface\ recombination} \tag{30}$$

where J_{SRH}, J_{Auger}, $J_{radiative}$ and $J_{surface\ recombination}$ are Shockley-Read-Hall recombination current density, auger recombination current density, radiative recombination current density and surface recombination current density, respectively.

The current density J_{SRH} associated with the SRH recombination process can be calculated using this formula:

$$J_{SRH} = \frac{q}{w_{tot}} \int_R R_{SRH}(x,y)dA \tag{31}$$

where R_{SRH} is the SRH recombination rate, W_{tot} is the total width of the device and q is the elementary charge. Likewise, recombination current density from another generation-recombination processes such as auger, radiative and surface recombination can be computed using the spatial integration of the corresponding generation-recombination rates [60]. For the current density associated with the auger recombination, the formula is:

$$J_{Auger} = \frac{q}{w_{tot}} \int_R R_{Auger}(x,y)dA \quad \textbf{(32)}$$

where R_{Auger} is the auger recombination rate. For the $J_{radiative,}$ the formula is the following:

$$J_{radiative} = \frac{q}{w_{tot}} \int_R R_{Radiative}(x,y)dA \quad \textbf{(33)}$$

where $R_{radiative}$ is the radiative recombination rate. The current density associated with the surface recombination was calculated using the following formula:

$$J_{surface\ recombination} = \frac{q}{w_{tot}} \int_R R_{Surface\ recombination}(x,y)dA \quad \textbf{(34)}$$

where $R_{surface}$ recombination is the surface recombination rate. As shown in Figure 3. 6, perovskite thickness is a limiting parameter for top cell performance. By increasing the thickness, the J_{ph} is getting increase because more photons are absorbed. Until 430 nm, the J_{sc} is also increasing with the increase in perovskite thickness. After 430 nm, the J_{sc} is decreasing. This is due to the increase in the total recombination current densities in the perovskite. From the simulations, the highest J_{sc} was obtained for the perovskite thickness of 430 nm.

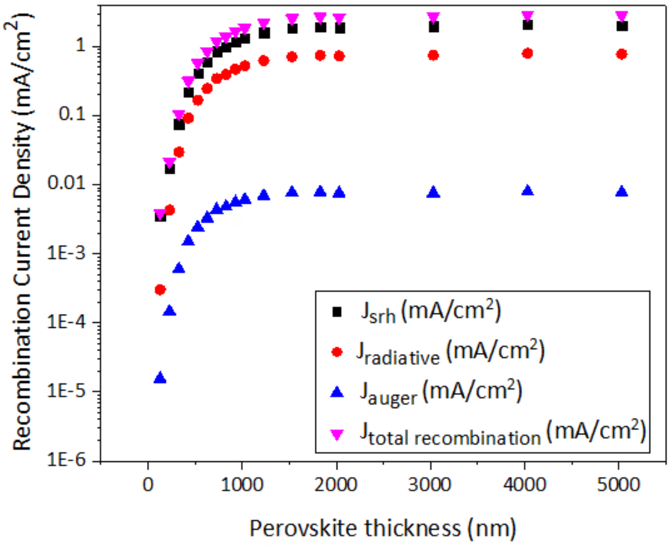

Figure 3. 7. The influence of perovskite thickness on recombination current densities.

Figure 3. 7 shows the relation of the perovskite thickness and the recombination current densities. From the simulations, it can be concluded that by increasing the perovskite thickness, the recombination current density of each recombination process also getting higher. The highest recombination current density value is the SRH recombination. This means that the amount of defects in the perovskite lattice are high so that the electrons are trapped at such a defect and thus recombine with the holes that are attracted by the trapped electrons [84]. The SRH is also known as the dominant generation-recombination process in semiconductor at most operational conditions [84].

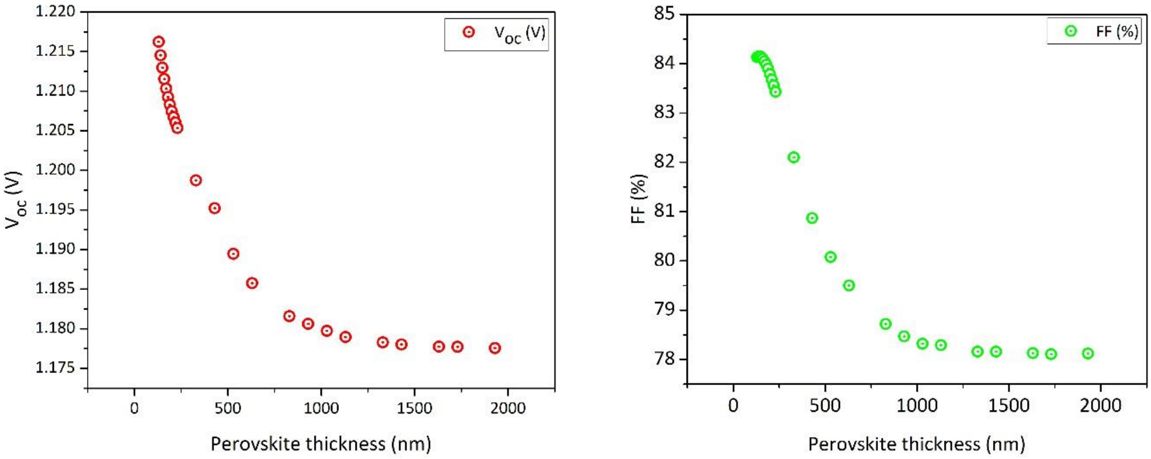

(a) (b)

Figure 3. 8. The effect of perovskite thickness on (a) V_{oc} (V), and (b) FF (%)

Figure 3. 8 (a) shows the effect of the perovskite thickness on V_{oc}. When a thin absorber layer of 130 nm was simulated, the photo current density and the short circuit current density are low. Nevertheless, the V_{oc} is high as can be seen in Figure 3. 8 (a). This relation is because at this value, the recombination is less as shown in Figure 3. 6. From the electrical simulations, by increasing the perovskite thickness, its open circuit voltage is decreasing. This is due to the higher recombination. The relation of the V_{oc} and the recombination can be known by using the following formula:

$$V_{oc} = \frac{K_B T}{q} \ln \left(\frac{J_{ph}}{J_o} + 1\right) \qquad \textbf{(35)}$$

where K_B is Boltzmann constant, q is elementary charge, J_{ph} is the photo-current density and Jo is saturation current density. Equation (35) shows that the V_{oc} is depending on J_{ph} and J_o. The photo-current density has a small variation whereas the saturation current density may differ by orders of magnitude. J_o depends on the recombination in the solar cells [85]. Hence, the recombination in the device will affect the V_{oc}. Figure 3. 8 (b) shows the results of the *FF* by varying the perovskite thickness. As shown in that figure, by increasing the thickness of the perovskite, the *FF* is decreasing. The decreasing of the *FF* is due to the increase in series resistance across the cell [86]. By using the optimum perovskite thickness of 430 nm, the *FF* is slightly decreasing from 82.1% to 80.87%, but the efficiency is increasing from 19.17% to 19.78%.

FTO Thickness

The second thickness optimization was done for fluorine-doped tin oxide (FTO). FTO is well known for its chemical and thermal stability [87]. It is also inexpensive material and can be a possible alternative to ITO [87]. In the simulation, the optimized thickness of the perovskite was used and the FTO thickness was varied from 100 nm to 700 nm. Figure 3. 9 (a) shows the influence of the FTO thickness on J_{ph} and J_{sc}. The J_{ph} and J_{sc} are indicated by black dots and blue dots, respectively. As can be seen from Figure 3. 9 (a), by increasing the FTO thickness, the J_{ph} and J_{sc} of the top cell were decreasing. It is due to the increase of the parasitic absorption in FTO layer [88]. Consequently, this loss decreases the number of photons taking part in the photo-electronic conversion process in the absorber which leads to the lower J_{ph} and J_{sc}.

Figure 3. 9 (b) and (c) show the effect of the FTO thickness on V_{oc} and *FF*. As you can see in the figure, the V_{oc} and *FF* values tend to be constant. The change in the thickness of the FTO does not really have an impact on the V_{oc} and *FF* values. Therefore, in this case, the perovskite efficiency value will depend more on the J_{sc} value. As shown in Figure 3. 9 (d), the efficiency trend is very similar to the trend of J_{sc} in Figure 3. 9 (a).

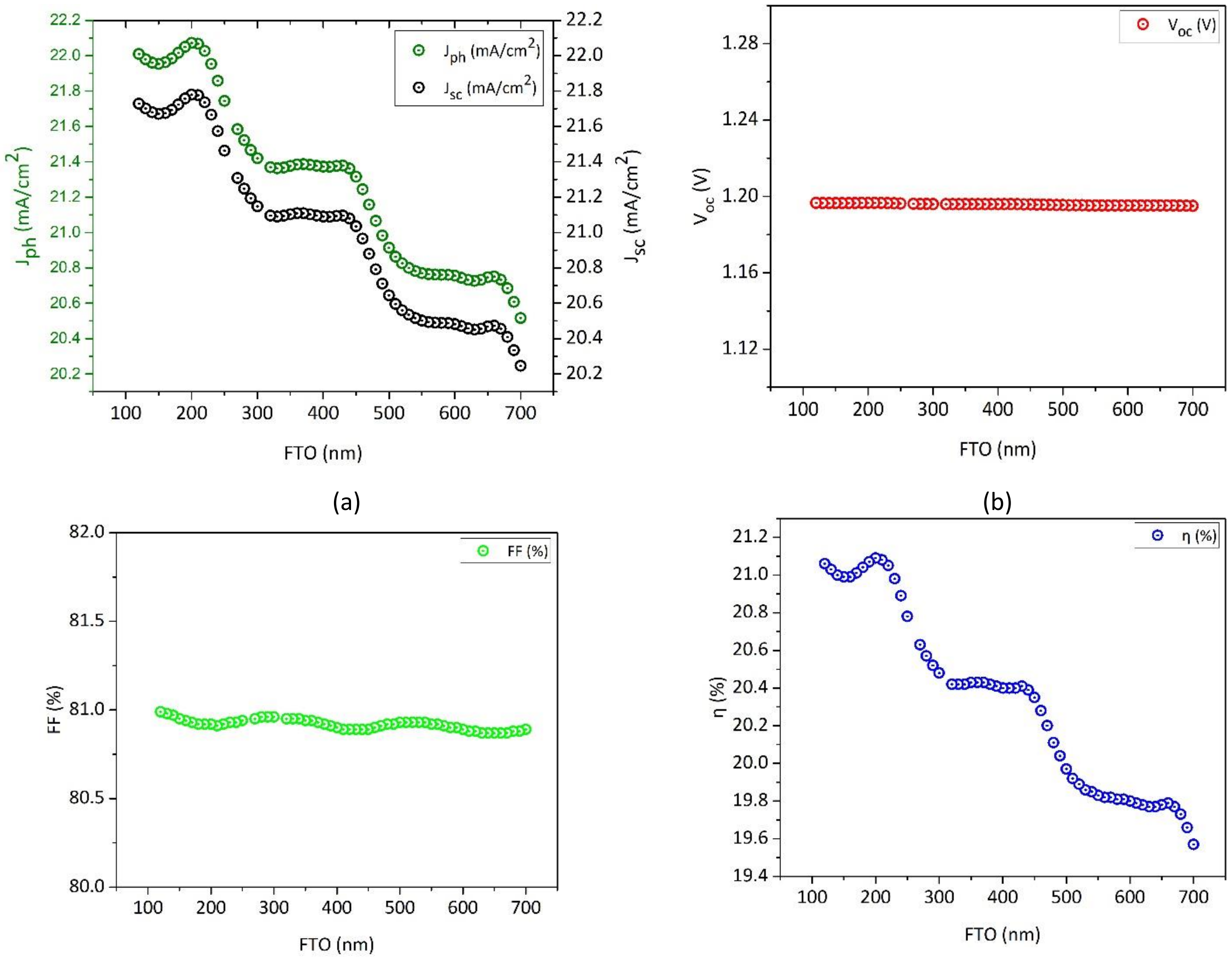

(a) (b)

(c) (d)

Figure 3. 9. The effect of FTO thickness on (a) J_{sc} (mA/cm^2), (b) V_{oc} (V), (c) FF (%) and (d) η (%)

Figure 3. 9 (d) shows the influence of the FTO thickness on efficiency. The increasing of FTO thickness deteriorates the top cell performance as indicated by the decrease in efficiency. The highest achievable efficiency by varying the FTO thickness was 21.04%. It was obtained by using the 200 nm thickness of FTO. Based on the literature, the 200 nm for the FTO thickness is experimentally possible [87].

ETL thickness

The third thickness optimization was done for TiO_2. TiO_2 acts as the electron transporting layer (ETL) in the top cell. The ETL plays an important role in the extraction and transportation of photogenerated electrons in the top cell [89]. It also contributes to achieving high-efficiency cells [90]. The optimum thickness of ETL is needed for highly efficient solar cells [90]. ETL's optimum thickness will lead to high transmittance, low leakage current between perovskite and ETL and low charge transfer resistance [90]. In the simulations, the optimum perovskite thickness of 430 nm, the optimum FTO thickness of 200 nm and HTL thickness of 350 nm were used [67]. The ETL thickness was varied from 25 nm to 100 nm. The simulation was not run below the 25 nm because considering the realistic aspect in the fabrication. The simulation results are shown in Figure 3. 10.

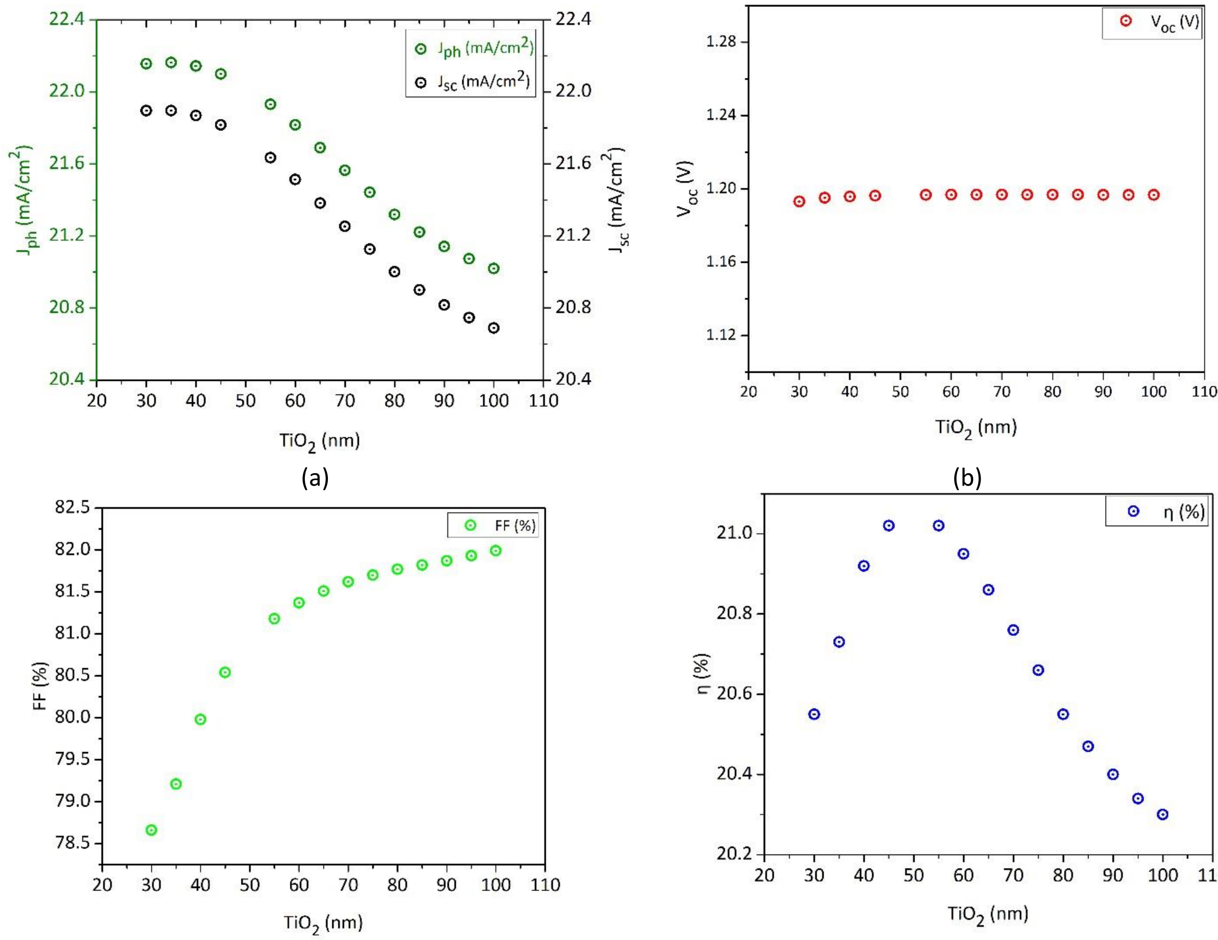

(a) (b)

(c) (d)

Figure 3. 10. The effect of ETL thickness on (a) J_{sc} (mA/cm^2), (b) V_{oc} (V), (c) FF (%) and (d) η (%)

Figure 3. 10 (a) and (b) shows the influence of ETL thickness on J_{ph} and J_{sc} and V_{oc}, respectively. As shown in Figure 3. 10 (a), the J_{ph} and J_{sc} are decreasing by increasing the ETL thickness. Based on the simulations, it shows that the varying of the ETL thickness is not significantly affect the V_{oc}. Its value is remain constant. The FF of the solar cell is increasing by increasing the ETL thickness. The highest efficiency of was obtained by using the ETL thickness of 45 nm.

HTL thickness

The last thickness optimization was done for Spiro-OMeTAD. Spiro-OMeTAD acts as the hole transporting layer (HTL) in the perovskite solar cell. In this simulation, the optimum thicknesses of FTO, perovskite and ETL were used. The thickness of HTL was varied from 40 nm to 175 nm.

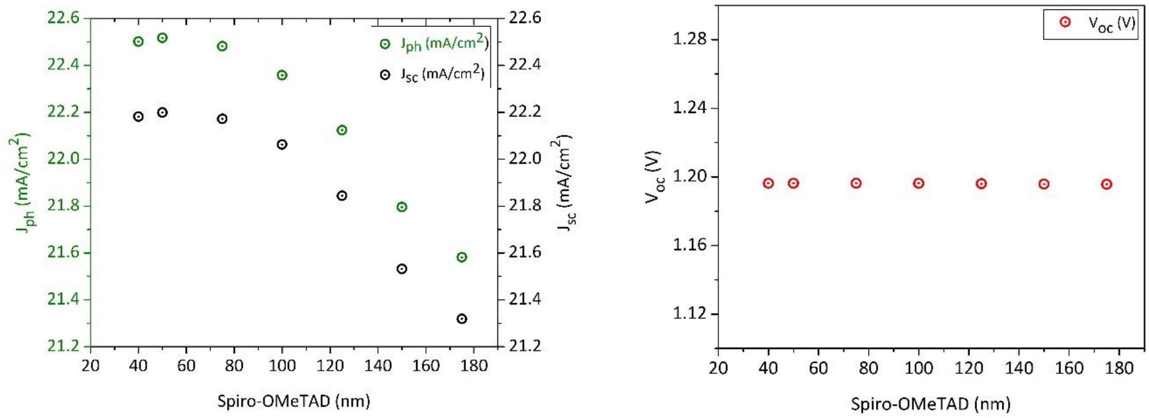

(a) (b)

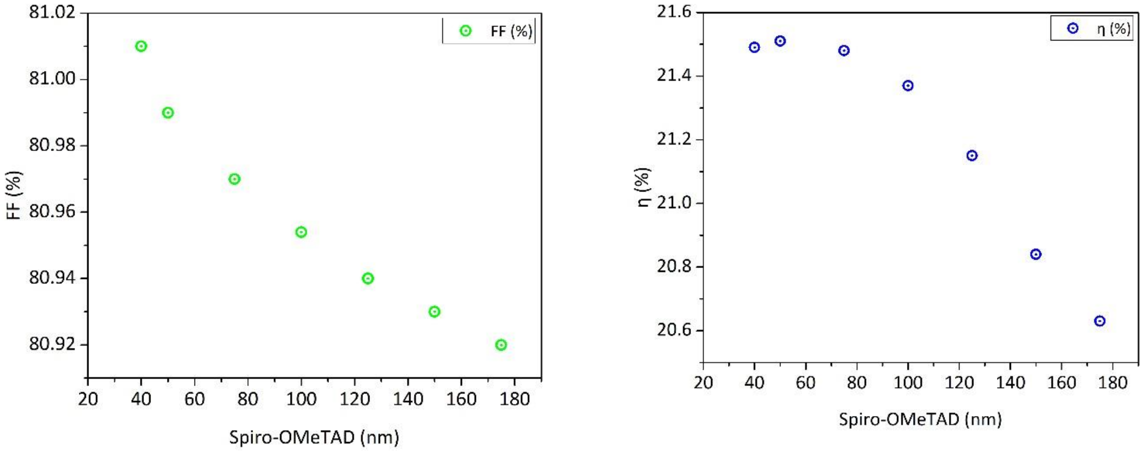

(c) (d)

Figure 3. 11. The effect of HTL thickness on (a) J_{sc} (mA/cm^2), (b) V_{oc} (V), (c) FF (%) and (d) η (%)

Figure 3. 11 (a) shows the effect of the HTL thickness on J_{ph} and J_{sc} , respectively. As shown in Figure 3. 11 (a), starting from 50 nm, the increase of HTL thickness will lead to low J_{ph} and J_{sc}. The reason is by increasing the HTL thickness, the distance travelled by holes to reach the electrode is getting larger, hence the probability of the recombination event is getting higher [91]. Figure 3. 11 (b) and (d) show the influence of the HTL thickness on V_{oc} and FF. As shown in Figure 3. 11 (b), the V_{oc} remains constant. The variation of the HTL thickness did not affect the V_{oc} value of the device. For the *FF*, by increasing the thickness of the spiro-OMeTAD, the FF value is decreasing. It is due to an increase in series resistance [86].

Figure 3. 11(d) shows the effect of the HTL thickness on efficiency. The optimum efficiency of 21.51% was achieved by using the HTL thickness of 50 nm. After that, efficiency is decreasing. This is due to the decreasing of the J_{sc}.

3.6. Conclusion

The purpose of this section is to answer the second research question introduced in section 1.10, which is "How much is the optimum efficiency of the top cell after optimization?". To answer that question, the summary of the optimized parameters of the top cell are shown below.

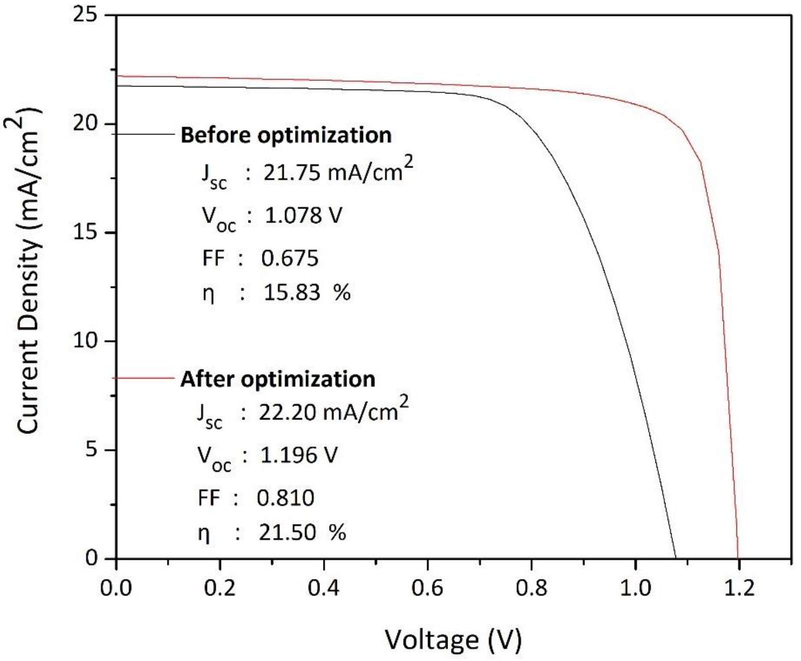

Figure 3. 12. Summary of the parameters of the top cell before optimization and after optimization

Figure 3. 12 shows the *J-V* curves and the summary of the output parameters of the top cell before optimization and after optimization. From the figure, it can be concluded that the optimization has improved the top cell efficiency from 15.83% into 21.50%.

4. Optimization of the tunnel recombination junction

In this chapter, the optimization of the tunnel recombination junction will be presented. Firstly, the optimized output of the individual (top and bottom) cells is shown. Secondly, the tandem cell output with the optimized top and bottom cell parameters are presented. Thirdly, the tandem was further optimized by optimizing the tunnel recombination junction. This chapter is aimed to answer the third research question introduced in section 1.10 which is "How much is the efficiency of the 2T perovskite/c-Si tandem after optimizing the tunnel recombination junction?" The parameters of the tunnel recombination junction optimized are Spiro-OMeTAD and ITO doping. To answer the main research questions, the main research questions were divided into two sub-research questions, i.e., "How much is the optimum ITO doping concentration?" and "How much is the optimum Spiro-OMeTAD doping concentration?"

4.1. Summary of the perovskite and c-Si after optimization

Table 4. 1 shows the output parameters of the perovskite solar cell and c-Si solar cell after having optimized them individually. The optimization of the perovskite as the top cell of the 2T tandem has been explained in Chapter 3. The optimization of the c-Si to be used as the bottom cell has been done in other work (the publication is in the process).

Table 4. 1. The output parameters of the optimized perovskite and c-Si

Individual Cell	Output parameters			
	J_{sc} (mA/cm^2)	V_{oc} (V)	FF (%)	η (%)
Perovskite	22.20	1.196	80.99	21.50
c-Si	41.13	0.72	84.52	25.03

As shown in Table 4. 1, after optimization, the efficiency of the perovskite and c-Si solar cells are 21.50% and 25.03%, respectively. The next step is building a 2T perovskite/c-Si modelling framework using the optimum optical and electrical parameters of the perovskite and c-Si solar cells in Sentaurus TCAD.

4.2. Modelling framework of the 2T perovskite/c-Si tandem solar cells

In this section, the modelling framework of the 2T perovskite/c-Si tandem solar cells is explained in detail.

First, the optical simulations of the 2T perovskite/c-Si using the optimum thickness were conducted. The optical generation profile from GenPro4 will be used in Sentaurus TCAD. Second, the 2T perovskite/c-Si tandem structure was built in the Sentaurus structure editor. The perovskite solar cells' rear metal was removed and then the structure was stacked on the top of the textured bottom cells. Spiro-OMeTAD from the perovskite solar cells and the front ITO of the bottom cells act as the tunnel recombination junction. The Glass and EVA, as encapsulated materials, are also added to the structure. Other parameters such as metal contacts, doping, meshing strategy and optical generation profile were added in this phase. Third, the device structure then generated using the Sentaurus mesh from within the Sentaurus structure editor and used as the grid file in the Sentaurus device. The material parameters of the tandem cells are created in MatPar. The physical models of the 2T perovskite/c-Si tandem were inputted in the Sentaurus Device. The Sentaurus device then simulates the 2T perovskite/c-Si tandem by referring to the grid and parameter files. Finally, the output parameters such as J_{sc}, V_{oc}, FF and η are then extracted by using Sentaurus Visual. The modelling framework of the 2T perovskite/c-Si is shown in Figure 4. 1.

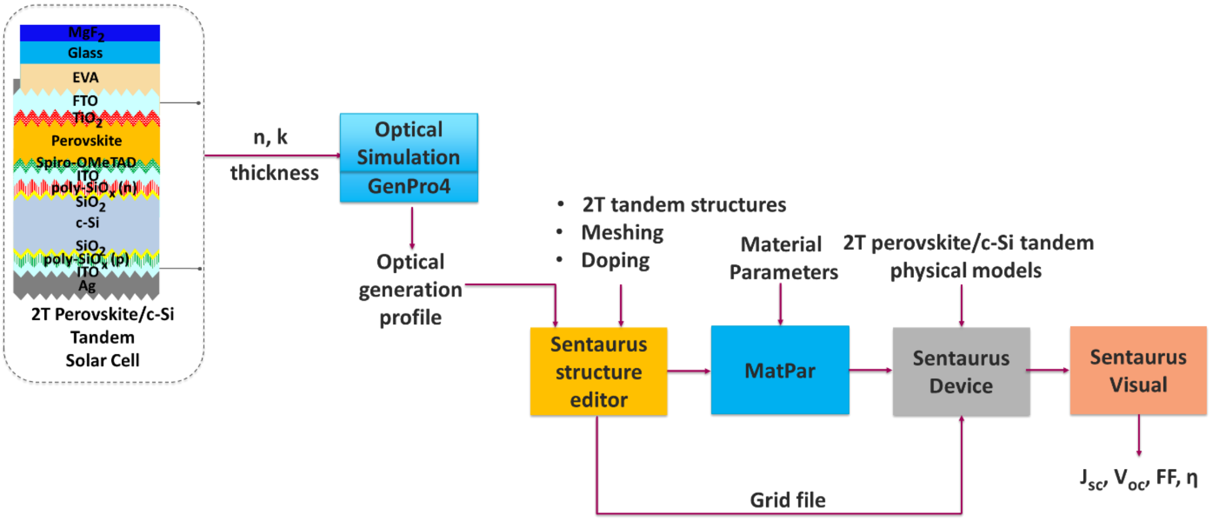

Figure 4. 1. Simulation steps of the 2T perovskite/c-Si tandem solar cells

The physical modelling used for the 2T perovskite/c-Si tandem solar cells are shown in Table 4. 2 below.

Table 4. 2. Simulation parameters of the 2T perovskite/c-Si tandem solar cells

Device Modelling	
Model	**Description**
Carrier transport	Drift-diffusion model
The effect of interface defect	Surface recombination velocity
Recombination	SRH recombination
	Auger recombination
	Radiative recombination
Heterostructure device simulation	Thermionic emission
Doping	Phosphorous and boron constant profile
Non-local tunneling	Band to band tunneling

4.3. The result of 2T tandem (before optimizing the TRJ)

After the perovskite and c-Si are stacked together, the 2T tandem structure is simulated. The simulation results are shown in Table 4. 3.

Table 4. 3. The output parameters of the 2T tandem before optimizing the TRJ

	Output parameters			
	J_{sc} (mA/cm^2)	V_{oc} (V)	FF (%)	η (%)
2T Tandem Cells	19.84	1.929	87.99	33.67

As shown in Table 4. 3, the 2T tandem efficiency of 33.67% can be obtained using the optimized parameters of the top cell and bottom cell. In the simulations, the current matching was achieved by varying the perovskite thickness. It is a good sign that from the simulations, our new bottom cell structure combined with the chosen perovskite structure can generate the 2T tandem solar cells efficiency of more than 30%. It has surpassed the current record efficiency of 2T tandem, which is 29.15% from HZB.

The tandem device's performance can be further optimized by optimizing the tunnel recombination junction [52]. It plays an important role in the performance of the tandem cells [51]. The band diagram of the 2T perovskite/c-Si before optimizing the TRJ are shown below.

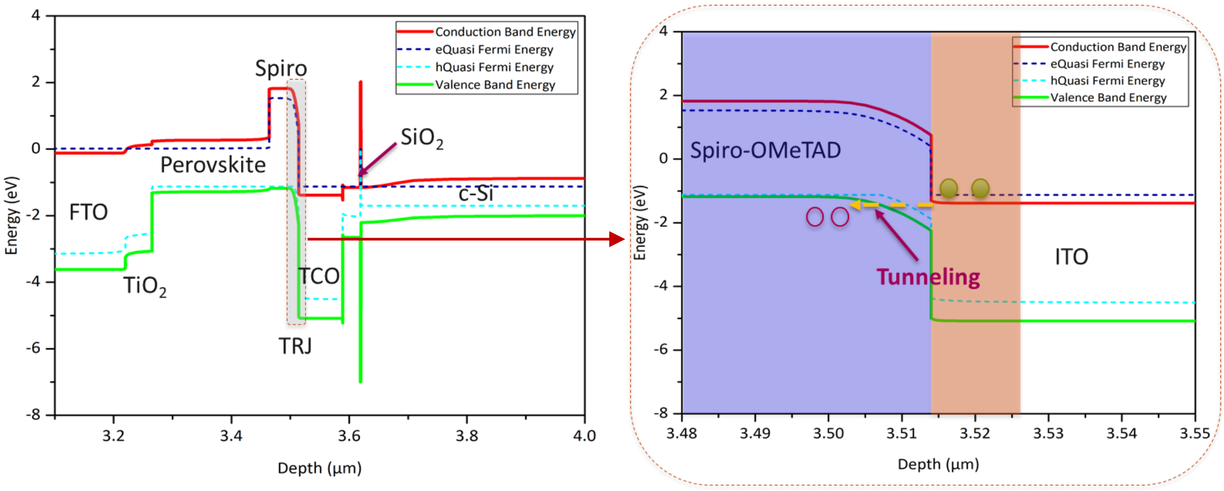

(a) (b)

Figure 4. 2 (a) Band diagram of the 2T perovskite/c-Si tandem solar cells before optimizing the TRJ; (b) A closer view of the TRJ area

Figure 4. 2 (a) shows the band diagram of the 2T perovskite/c-Si tandem solar cells before optimizing the TRJ. The doping concentration used of the Spiro-OMeTAD and ITO are 2.10^{18} cm^{-3} and 1.10^{20} cm^{-3}, respectively. The red line and green line are the conduction band and valence band energy, respectively. The dashed dark blue and light blue are the quasi-Fermi level of the electrons and holes, respectively. When the photons enter the device, the photon with the energy > bandgap energy of the perovskite will be absorbed by the top cell, the remaining photons will be transmitted to tunnel junction layers and the ones that are not absorbed by these layers reach c-Si and are absorbed by the c-Si according to its bandgap. The electron-hole pair will be generated in the absorbers and supporting layers. As shown in Figure 4. 2 (a), the electron in the perovskite will be going to the FTO and collected in the front contact and the holes will be going to the Spiro-OMeTAD (HTL). In the bottom cell, the electron-hole pair will be generated in the c-Si. The electron will be going to the ITO (TCO) and holes will be going to the bottom poly-SiO_x and get collected by the back contact. The electron from ITO and holes from the Spiro-OMeTAD will recombine in the tunnel recombination junction. Figure 4. 2 (b) shows the closer view of the tunnel recombination junctions. The electrons can tunnel and recombine with holes if the depleted region becomes thin enough [92]. The depleted region is influenced by the doping of the two sides of the recombination junction, i.e., Spiro-OMeTAD and ITO [93].

4.4. Optimization parameters

The tunnel recombination junction occurred between the Spiro-OMeTAD and ITO layers. The tunneling process is highly affected by doping concentration [94]. Therefore, the parameters need to be optimized are the doping concentration of the TRJ. In this case, is the doping concentration of the Spiro-OMeTAD and ITO.

4.5. Results and discussions

This section is divided into two parts; first, optimizing the TRJ by changing the TCO doping concentration. Second, the further optimization of the TRJ by keeping the optimum doping concentration of the TCO and varying the doping concentration of HTL.

4.5.1. Optimization the TRJ by changing the TCO doping

Here, the effect of the doping concentration of TCO to the J_{sc}, V_{oc}, *FF* and η are shown in Figure 4. 3.

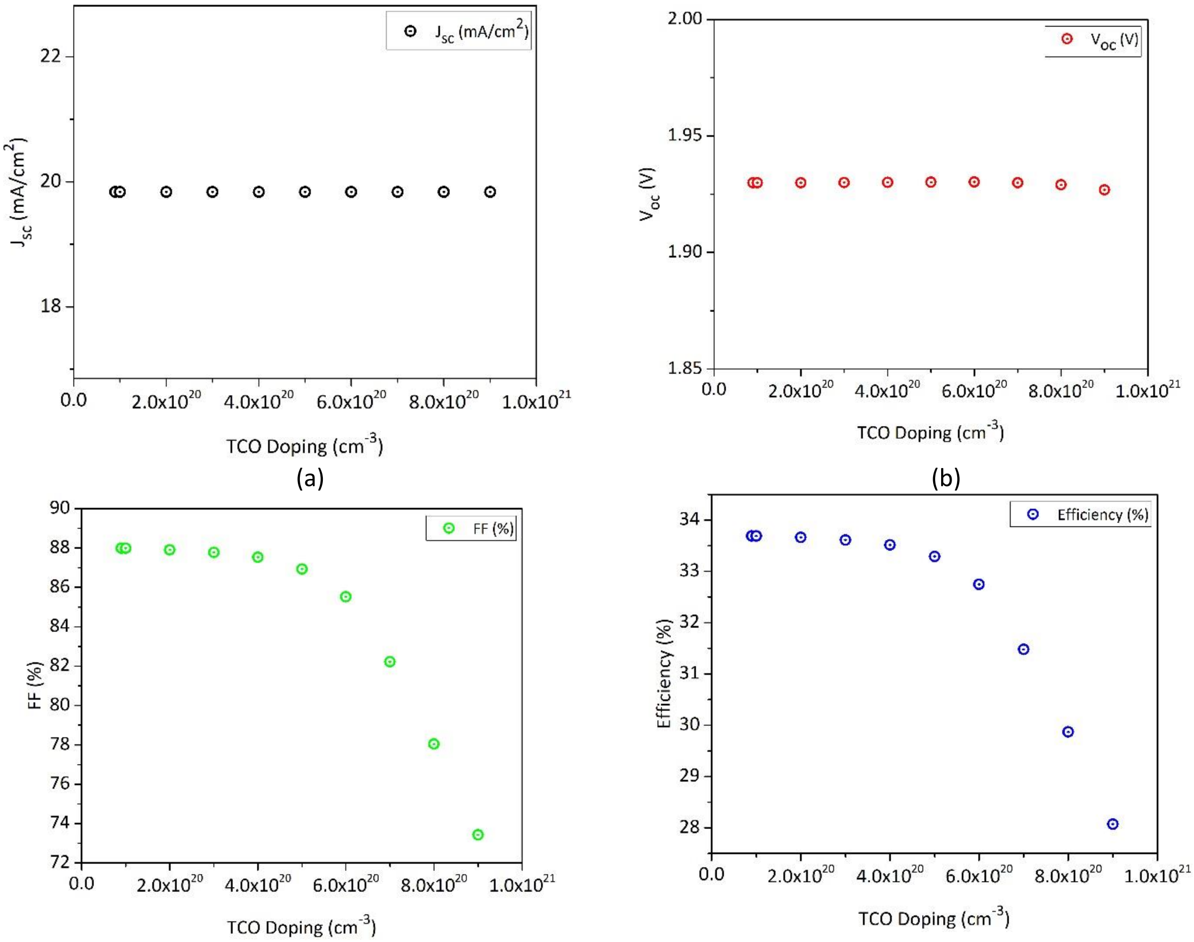

(a) (b) (c) (d)

Figure 4. 3. Effect of the TCO doping to the PV parameters; (a) on J_{sc}, (b), on V_{oc}, (c) on *FF* and (d) on η

The TCO doping was varied from 9.10^{19} cm^{-3} to 9.10^{20} cm^{-3}. The default doping of the TCO before the optimization is 1.10^{20} cm^{-3}. This value is obtained from the bottom cell parameters. As shown in Figure 4. 3, the J_{sc} and V_{oc} values remain constant. The V_{oc} of the highest and lowest TCO doping only has a small difference, i.e., 0.003 V. From the simulations, the highest performance of the 2T tandem cell was achieved by using the TCO doping concentration of 9.10^{19} cm^{-3}. The optimization of the TRJ by changing the TCO doping leads to increased efficiency from 33.689% to 33.691%. Apparently, the 1.10^{20} cm^{-3} as the default doping has approached the optimum doping concentration for TCO. When the doping value is lower than 9.10^{20} cm^{-3}, the convergence issue was happening in the simulation. The variation in doping is affecting the *FF* and efficiency in tandem. The *FF* is decreasing as the doping concentration increases. The increase of doping concentration leads to the misalignment of the quasi-Fermi level of the electrons and holes. The misalignment will reduce the carrier transport and leads to the decreasing of *FF*. The decreasing of η is due to the decreasing of the *FF*. To get clearer about the carrier transport in the TRJ, the comparison of the band diagram of the tandem with the highest and lowest efficiency is shown below in Figure 4. 4 and Figure 4.5.

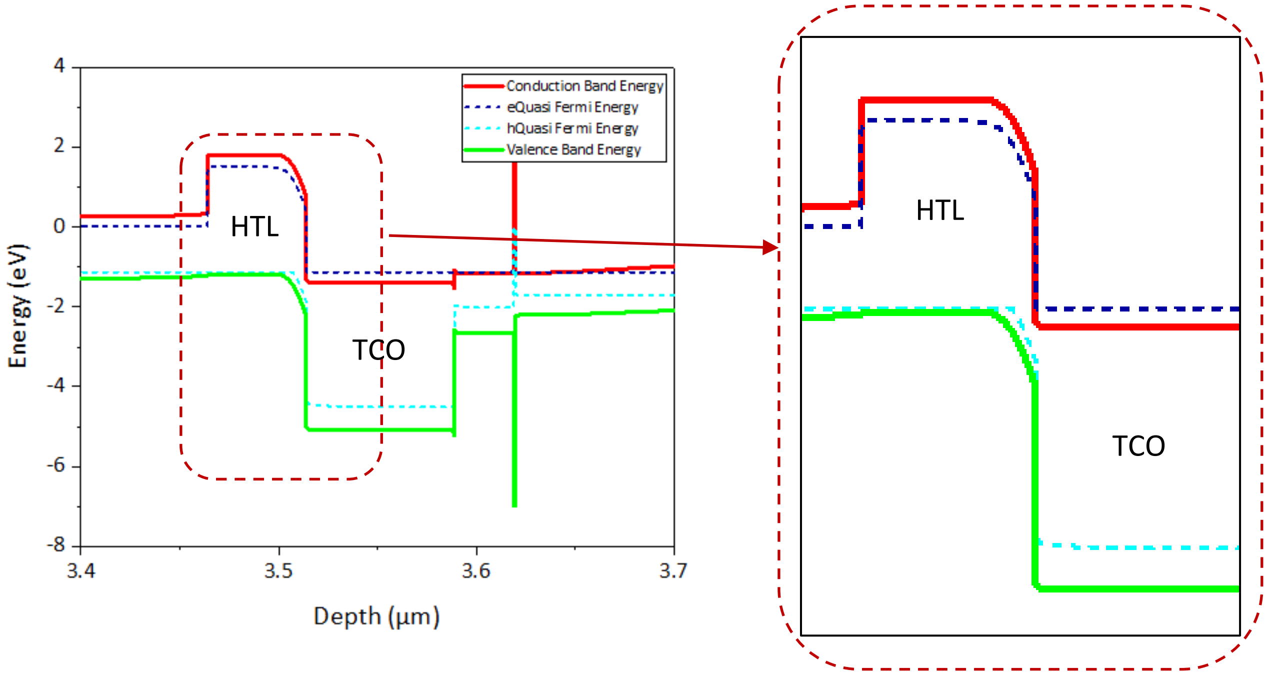

(a) (b)

Figure 4. 4. (a) Band diagram of the 2T perovskite/c-Si tandem with TCO doping concentration of 9.10^{19} cm^{-3}; (b) Showing perfect band alignment between E_{fn} and E_{fp}

Figure 4. 4 (a) shows the band diagram of the 2T perovskite/c-Si tandem with the optimum TCO doping concentration i.e. 9.10^{19} cm^{-3} whereas

Figure 4. 4 (b) shows the closer view of the TRJ. As can be seen in

Figure 4. 4 (b), the quasi-Fermi level of the electrons and holes are aligned, hence this makes a good carrier transport and leads to the high *FF*.

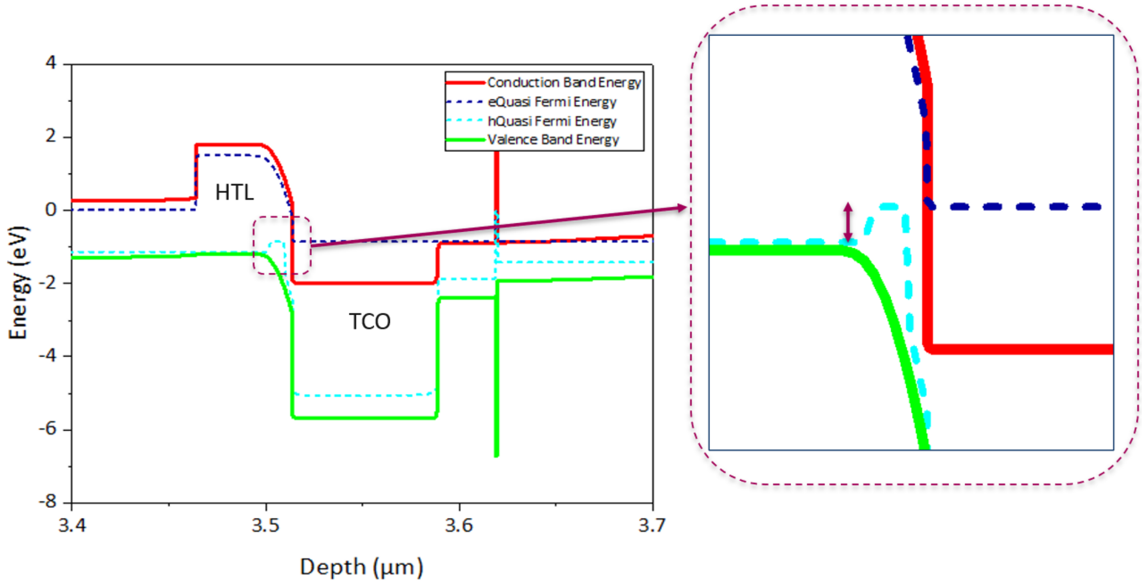

(a) (b)

Figure 4.5. Band diagram of the 2T perovskite/c-Si tandem with TCO doping concentration of 9E20 cm^{-3}; (b) Showing misalignment indicated by purple arrow

From the band diagram, we see that the decreasing of the *FF* was due to the misalignment of the quasi fermi energy of electrons (E_{fn}) and holes (E_{fp}).

4.5.2. Optimization the TRJ by changing the HTL doping

After obtaining the optimum doping of the TCO, the next aim was to get the optimum doping concentration of the HTL. By keeping the optimum TCO doping concentration of 9.10^{19} cm^{-3}, the doping of the HTL was varied from 2.10^{18} cm^{-3} to 1.10^{20} cm^{-3}. The simulation results are shown below.

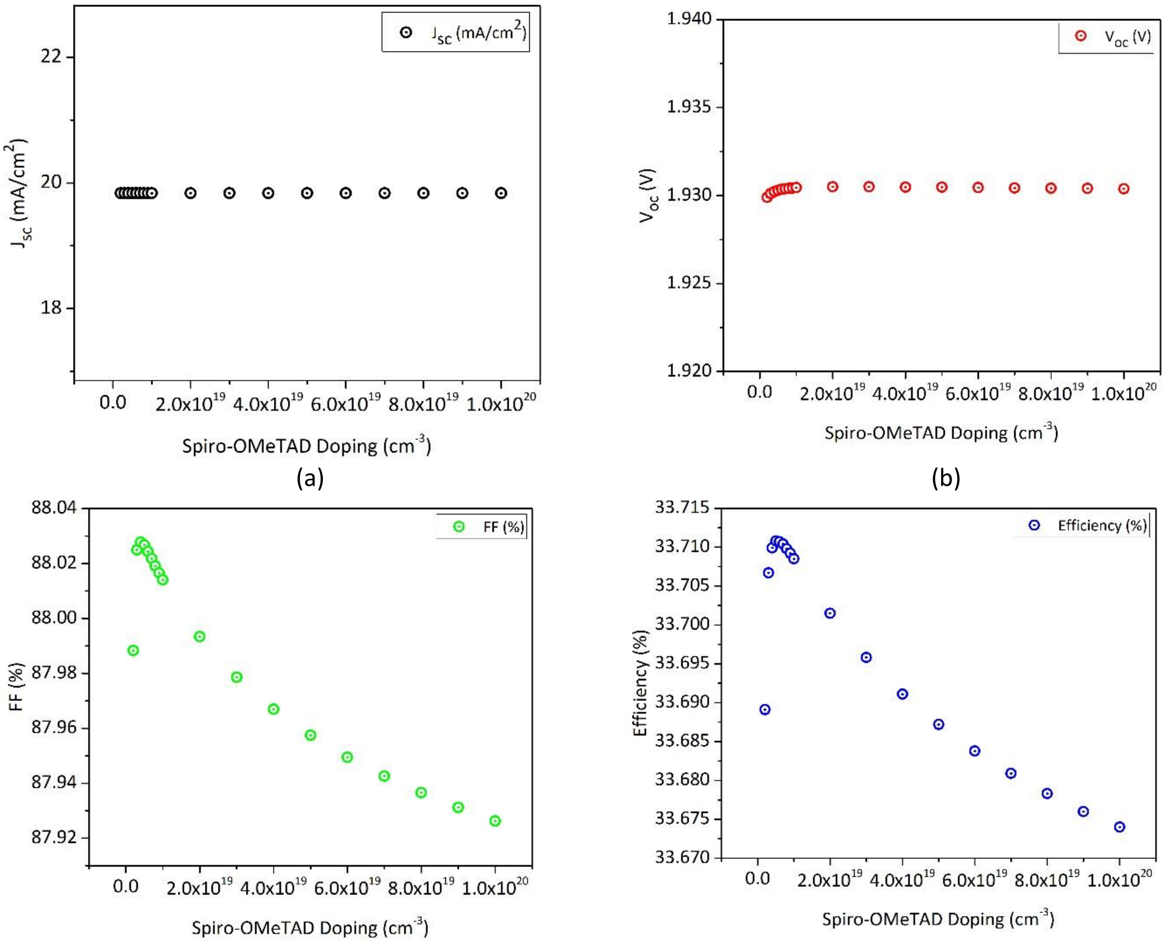

(a)

(b)

(c)

(d)

Figure 4. 6. Effect of the HTL doping to the PV parameters; (a) on J_{sc}, (b), on V_{oc}, (c) on *FF* and (d) on η

Figure 4. 6 shows the effect of the HTL doping on the J_{sc}, V_{oc}, *FF* and η. Spiro-OMeTAD is used as the hole transporting material. From the simulations, when the doping concentration of ITO is optimum, the changing in doping concentration of Spiro-OMeTAD has no significant effect in J_{sc}, V_{oc}, *FF* and η. The J_{sc} values are constant. The different of *Voc* for the highest and lowest Spiro-OMeTAD doping concentration was only 0.0006 V. For the *FF*, by changing the doping concentration of Spiro-OMeTAD from 2.10^{18} cm^{-3} to 1.10^{20} cm^{-3}, the FF was slightly decreasing from 87.9883% to 87.9263%. Because the J_{sc} and V_{oc} are mostly constant, the η of the tandem is mostly affected by the change in FF. From the simulations, it was found that the optimum doping concentration of Spiro-OMeTAD is 5.10^{18}cm^{-3}. It leads to the increasing of the 2T tandem efficiency from 33.689% to 33.702%. The summary of the optimum doping concentration of TCO and HTL are shown below.

Table 4. 4. Summary of the optimum doping concentration of the TCO and HTL

Layer	Doping Concentration
TCO	9.10^{19} cm^{-3}
HTL	5.10^{18} cm^{-3}

4.5.3. 2T perovskite/c-Si tandem output

Figure 4. 7 shows the J-V curves of the tandem and the output parameters of the 2T tandem before and after optimizing the TRJ, respectively.

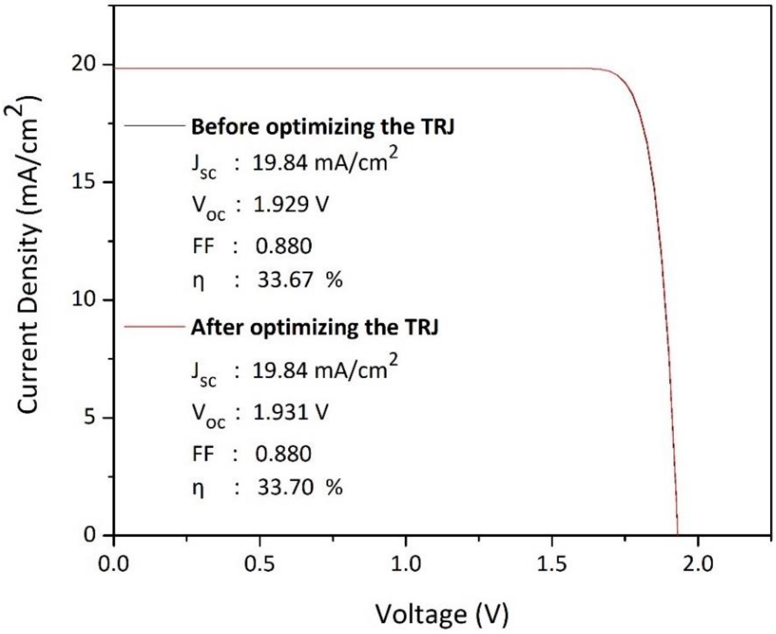

Figure 4. 7. The J-V curves and optimum output parameters of the 2T perovskite/c-Si

As can be seen on Figure 4. 7, by optimizing the doping concentration of the TCO and HTL, there is a slight increase in V_{oc} from 1.929 V to 1.931 V. The *FF* remains constant The efficiency increases slightly from 33.67% to 33.70%.

4.6. Conclusions

In this chapter, the optimum output parameters of the perovskite and c-Si solar cells are presented. The output parameter of the 2T tandem perovskite/c-Si before optimizing the TRJ are also shown. Afterwards, the optimization of the tunnel recombination junction by varying the HTL and TCO doping concentration also have been conducted.
In order to answer the main research question: "How much is the efficiency of the 2T perovskite/c-Si tandem after optimizing the tunnel recombination junction?"

The following sub questions are arise:

- "How much is the optimum TCO doping concentration?"
- "How much is the optimum HTL doping concentration?"

From the simulations, the optimum TCO and HTL doping concentrations have been obtained. The optimum doping concentration of TCO and HTL are 9.10^{19} cm^{-3} and $5.^{18}$ cm^{-3}, respectively. An efficiency of 33.70% is achieved after optimizing the doping parameters of TRJ. It is also concluded that when the doping concentration of TCO is optimum, changes in Spiro-OMeTAD's doping concentration do not significantly impact the value of the tandem efficiency, but when the TCO doping is not optimum, the changing in spiro doping has a significant impact on efficiency.

5. Conclusions and Outlook

5.1. Conclusions

In this chapter, the final conclusions of this thesis work are summarized. The main research questions presented in 1.10 will be answered.

The implied photo current density produced by the 2T and 3T perovskite/c-Si tandem solar cells after thickness optimization are shown in Table 5. 1.

Table 5. 1. The summary of the J_{ph} of 2T and 3T perovskite/c-Si tandem after thickness optimization.

CSPCs	Fully Textured		Fully Textured	
	2T		3T	
	J_{ph} (mA/cm^2)		J_{ph} (mA/cm^2)	
	Perovskite	c-Si	Perovskite	c-Si
poly-Si	19.54	19.53	19.51	19.56
poly-SiC$_x$	19.31	19.30	19.31	19.31
poly-SiO$_x$	19.43	19.42	19.48	19.50

Table 5. 2 shows the 2T, 3T and 4T perovskite/c-Si tandem after encapsulation.

Table 5. 2. The summary of the J_{ph} of 2T, 3T and 4T perovskite/c-Si tandem after encapsulation.

CSPCs	Fully Textured		Fully Textured		Flat Textured	
	2T		3T		4T	
	J_{ph} (mA/cm^2)		J_{ph} (mA/cm^2)		J_{ph} (mA/cm^2)	
	Perovskite	c-Si	Perovskite	c-Si	Perovskite	c-Si
poly-Si	19.54	19.53	19.51	19.56	17.95	18.9
poly-SiC$_x$	19.31	19.30	19.31	19.31	17.58	18.9
poly-SiO$_x$	19.43	19.42	19.48	19.50	17.91	18.95

Based on the two tables above, the use of poly-Si as CSPCs resulted in the highest J_{ph} value compared to poly-SiO$_x$ and poly-SiC$_x$. This is because the poly-Si has the lowest free carrier absorption coefficient than the poly-SiC$_x$ and poly-SiO$_x$.

From the optimization of the contact resistance, surface recombination velocity and the thickness of top cell (perovskite solar cell), the efficiency can be improved from 15.83% to 21.50%.

From the tunnel recombination junction optimization, by varying the doping concentration of TCO and HTL, the efficiency of the two-terminal (2T) perovskite/c-Si tandem of 33.7% can be achieved. In this thesis work, it was found that ITO (TCO) and Spiro-OMeTAD (HTL) doping level are important for TRJ band alignment.

5.2. Outlook

After several achievements, as explained in conclusion, some further work can still be done, which is:

- Simulate an electrical tandem structure with other CSPCs such as poly-Si and poly-SiC$_x$.
- Comparing the results of this thesis work with perovskite/SHJ solar cells because SHJ is the most common bottom cell structure used in tandem.
- Optimization of the c-Si thickness in the tandem because generally, the industry uses a c-Si thickness of 180 µm for higher V_{oc}.

References

[1] H. A. Rypkema, "Environmental Chemistry, Renewable Energy, and Global Policy," in *Green Chemistry: An Inclusive Approach*, Elsevier Inc., 2018, pp. 19-47.

[2] N. Kannan and D. Vakeesan, *Solar energy for future world: - A review,* vol. 62, Elsevier Ltd, 2016, pp. 1092-1105.

[3] O. Ellabban, H. Abu-Rub and F. Blaabjerg, *Renewable energy resources: Current status, future prospects and their enabling technology,* vol. 39, Elsevier Ltd, 2014, pp. 748-764.

[4] J. M. Zepter, A. Lüth, P. Crespo del Granado and R. Egging, "Prosumer integration in wholesale electricity markets: Synergies of peer-to-peer trade and residential storage," *Energy and Buildings,* vol. 184, pp. 163-176, 1 2 2019.

[5] "Framework Contract EAHC/2013/CP/04," 2017.

[6] G. Kavlak, J. McNerney and J. E. Trancik, "Evaluating the causes of cost reduction in photovoltaic modules," *Energy Policy,* vol. 123, pp. 700-710, 1 12 2018.

[7] A. Smets, K. Jager, O. Isabella, R. Van Swaaij and M. Zeman, "Surface Recombination," in *Solar Energy*, Delft, UIT Cambridge, 2016, p. 78.

[8] M. Z. Jacobson and M. A. Delucchi, "Providing all global energy with wind, water, and solar power, Part I: Technologies, energy resources, quantities and areas of infrastructure, and materials," *Energy Policy,* vol. 39, no. 3, pp. 1154-1169, 3 2011.

[9] "Hybrid tandem solar cells A route towards high efficiency solar cells," 2017.

[10] T. Todorov, O. Gunawan and S. Guha, "A road towards 25% efficiency and beyond: Perovskite tandem solar cells," *Molecular Systems Design and Engineering,* vol. 1, no. 4, pp. 370-376, 2016.

[11] R. &. K. R. Garrison, "Higher efficiency tandem solar cells through composite-cell current matching," *Optics express,* vol. 27, no. 8, pp. A543-A571, 2019.

[12] E. Köhnen, M. Jošt, A. B. Morales-Vilches, P. Tockhorn, A. Al-Ashouri, B. Macco, L. Kegelmann, L. Korte, B. Rech, R. Schlatmann, B. Stannowski and S. Albrecht, "Highly efficient monolithic perovskite silicon tandem solar cells: Analyzing the influence of current mismatch on device performance," *Sustainable Energy and Fuels,* vol. 3, no. 8, pp. 1995-2005, 2019.

[13] M. I. Hossain, W. Qarony, S. Ma, L. Zeng, D. Knipp and Y. H. Tsang, *Perovskite/Silicon Tandem Solar Cells: From Detailed Balance Limit Calculations to Photon Management,* vol. 11, SpringerOpen, 2019.

[14] E. L. D. M. G. S. P. &. T. A. C. Warren, "Modeling three-terminal III-V lSi tandem solar cells," *IEEE 44th Photovoltaic Specialist Conference (PVSC),* pp. 2488-2491, 2017.

[15] M. W. E. L. S. M. S. H. N. R. B. R. .. &. P. R. Rienäcker, "Back-contacted bottom cells with three terminals: Maximizing power extraction from current-mismatched tandem cells," *Progress in Photovoltaics: Research and Applications,* vol. 27, no. 5, pp. 410-423, 2019.

[16] E. L. D. M. G. R. M. P. R. T. A. C. &. S. P. Warren, "Maximizing tandem solar cell power extraction using a three-terminal design," *Sustainable Energy & Fuels,* vol. 2, no. 6, pp. 1141-1147, 2018.

[17] D. A. Neamen, Semiconductor Physics and Devices, New York: McGraw-Hill, 2012.

[18] M. G.Mauk, "Chapter I-2-D - Thin Crystalline and Polycrystalline Silicon Solar Cells," *McEvoy's Handbook of Photovoltaics (Third Edition),* pp. 159-231, 2018.

[19] I. Fraunhofer Institute for Solar Energy Systems, "Photovoltaics report," Fraunhofer, Munchen, 2020.

[20] M. Bhati and R. Rai, "Commercialization of large-scale perovskite solar energy technology and scaling-up issues," in *Perovskite Photovoltaics: Basic to Advanced Concepts and Implementation*, Elsevier, 2018, pp. 387-445.

[21] S. C. Watthage, Z. Song, A. B. Phillips and M. J. Heben, "Evolution of perovskite solar cells," in *Perovskite Photovoltaics: Basic to Advanced Concepts and Implementation*, Elsevier, 2018, pp. 43-88.

[22] P. Mathan Kumar, A. Das, L. Seban and R. G. Nair, "Fabrication and life time of perovskite solar cells," in *Perovskite Photovoltaics: Basic to Advanced Concepts and Implementation*, Elsevier, 2018, pp. 231-287.

[23] S. A. Olaleru, J. K. Kirui, D. Wamwangi, K. T. Roro and B. Mwakikunga, *Perovskite solar cells: The new epoch in photovoltaics,* vol. 196, Elsevier Ltd, 2020, pp. 295-309.

[24] P. C. Reshmi Varma, "Low-dimensional perovskites," in *Perovskite Photovoltaics: Basic to Advanced Concepts and Implementation*, Elsevier, 2018, pp. 197-229.

[25] D. Wang, M. Wright, N. K. Elumalai and A. Uddin, *Stability of perovskite solar cells,* vol. 147, Elsevier, 2016, pp. 255-275.

[26] Q. Xu, D. Yang, J. Lv, Y.-Y. Sun and L. Zhang, "Perovskite Solar Absorbers: Materials by Design," *Small Methods,* vol. 2, no. 5, p. 1700316, 5 2018.

[27] J. H. Heo, M. H. Lee, M. H. Jang and S. H. Im, "Highly efficient CH3NH3PbI3−xClx mixed halide perovskite solar cells prepared by re-dissolution and crystal grain growth via spray coating," *Journal of Materials Chemistry A,* vol. 4, no. 45, pp. 17636-17642, 2016.

[28] M. S. a. G. T. M. Hamed, "Mixed Halide Perovskite Solar Cells: Progress and Challenges," *Critical Reviews in Solid State and Materials Sciences,* vol. 45, no. 2, pp. 85-112., 2020.

[29] N. G. Park, *Perovskite solar cells: An emerging photovoltaic technology,* vol. 18, Elsevier, 2015, pp. 65-72.

[30] Z. L. Z. M. L. L. S. Y. &. G. P. Zhang, "Perovskite-Based Tandem Solar Cells: Get the Most Out of the Sun," *Advanced Functional Materials,* vol. 30, no. 38, p. 2001904, 2020.

[31] K. K. H. Y. W. I. T. K. K. N. K. .. &. Y. K. Yoshikawa, "Silicon heterojunction solar cell with interdigitated back contacts for a photoconversion efficiency over 26%," *Nature energy,* vol. 2, no. 5, p. 17032, 2017.

[32] J. D. A. F. M. S. F. T. M. C. H. Z. .. &. B. C. Peter Seif, "Amorphous silicon oxide window layers for high-efficiency silicon heterojunction solar cells.," *Journal of Applied Physics,* vol. 115, no. 2, p. 024502, 2014.

[33] A. A. C. B. N. B. L. C. J. D. F. .. &. S. L. Descoeudres, "Silicon heterojunction solar cells: towards low-cost high-efficiency industrial devices and application to low-concentration PV," *Energy Procedia,* vol. 77, pp. 508-514, 2015.

[34] A. Rohatgi, K. Zhu, J. Tong, D. H. Kim, E. Reichmanis, B. Rounsaville, V. Prakash and Y. W. Ok, "26.7% Efficient 4-Terminal Perovskite-Silicon Tandem Solar Cell Composed of a High-Performance Semitransparent Perovskite Cell and a Doped Poly-Si/SiOx Passivating Contact Silicon Cell," *IEEE Journal of Photovoltaics,* vol. 10, no. 2, pp. 417-422, 1 3 2020.

[35] L. L. Yan, C. Han, B. Shi, Y. Zhao and X. D. Zhang, *A review on the crystalline silicon bottom cell for monolithic perovskite/silicon tandem solar cells,* vol. 7, Elsevier Ltd, 2019.

[36] S. L. Z. D. W. Y. G. L. J. V. W. J. H. &. V. S. C. Luxembourg, "Evaluation of bottom cell concepts for perovskite/crystalline silicon tandems," *Solar Energy,* 2017.

[37] M. H. Futscher and B. Ehrler, *Efficiency Limit of Perovskite/Si Tandem Solar Cells,* vol. 1, American Chemical Society, 2016, pp. 863-868.

[38] N. N. Lal, Y. Dkhissi, W. Li, Q. Hou, Y. B. Cheng and U. Bach, "Perovskite Tandem Solar Cells," *Advanced Energy Materials,* vol. 7, no. 18, 20 9 2017.

[39] P. Tockhorn, P. Wagner, L. Kegelmann, J. C. Stang, M. Mews, S. Albrecht and L. Korte, "Three-Terminal Perovskite/Silicon Tandem Solar Cells with Top and Interdigitated Rear Contacts," *ACS Applied Energy Materials,* vol. 3, no. 2, pp. 1381-1392, 24 2 2020.

[40] T. Duong, H. Pham, T. C. Kho, P. Phang, K. C. Fong, D. Yan, Y. Yin, J. Peng, M. A. Mahmud, S. Gharibzadeh, B. A. Nejand, I. M. Hossain, M. R. Khan, N. Mozaffari, Y. L. Wu, H. Shen, J. Zheng, H.

Mai, W. Liang, C. Samundsett, M. Stocks, K. McIntosh, G. G. Andersson, U. Lemmer, B. S. Richards, U. W. Paetzold, A. Ho-Ballie, Y. Liu, D. Macdonald, A. Blakers, J. Wong-Leung, T. White, K. Weber and K. Catchpole, "High Efficiency Perovskite-Silicon Tandem Solar Cells: Effect of Surface Coating versus Bulk Incorporation of 2D Perovskite," *Advanced Energy Materials,* vol. 10, no. 9, 1 3 2020.

[41] S. W. Glunz and F. Feldmann, "SiO2 surface passivation layers – a key technology for silicon solar cells," *Solar Energy Materials and Solar Cells,* 2018.

[42] M. Almontazer, "Passivation Techniques and Mechanism for Crystalline Silicon Solar Cells," Karadeniz Technical University, Trabzon, Turkey, 2019.

[43] J. s. Wim J, H. C. R. and A. W. Weeber, "Bulk and surface passivation of silicon solar cells accomplished by silicon nitride deposited on industrial scale by microwave PECVD," *Progress in Photovoltaics: Research and Applications,* Vols. 551-569, p. 13(7), 2005.

[44] G. I. A. v. H. N. I. O. &. Z. M. Yang, "Design and application of ion-implanted polySi passivating contacts for interdigitated back contact c-Si solar cells," *Applied Physics Letters,* no. 033903, p. 108(3), 2016.

[45] G. Yang, A. Ingenito, O. Isabella and M. Zeman, "IBC c-Si solar cells based on ion-implanted poly-silicon passivating contacts," *Solar Energy Materials and Solar Cells,* 2016.

[46] F. Feldmann, C. Reichel, R. Müller and M. Hermle, "The application of poly-Si/SiOx contacts as passivated top/rear contacts in Si solar cells," *Solar Energy Materials and Solar Cells,* 2017.

[47] G. Yang, P. Guo, P. Procel, A. Weeber, O. Isabella and M. Zeman, "Poly-crystalline silicon-oxide films as carrier-selective passivating contacts for c-Si solar cells," *Applied Physics Letters,* vol. 112, no. 19, 7 5 2018.

[48] M. Singh, R. Santbergen, L. Mazzarella, A. Madrampazakis, G. Yang, R. Vismara, Z. Remes, A. Weeber, M. Zeman and O. Isabella, "Optical characterization of poly-SiOx and poly-SiCx carrier-selective passivating contacts," *Solar Energy Materials and Solar Cells,* vol. 210, 15 6 2020.

[49] A. Mandrampazakis, "Development of Silicon-rich poly-Silicon Carbide passivating contacts for solar cells," TU Delft, Delft, 2019.

[50] Z. Xu, K. Tao, S. Jiang, R. Jia, W. Li, Y. Zhou, Z. Jin and X. Liu, "Application of polycrystalline silicon carbide thin films as the passivating contacts for silicon solar cells," *Solar Energy Materials and Solar Cells,* 2020.

[51] Y. Lee, D. V. Ai, S. Kim, S. Han, H. Kim and J. Yi, "A study of tunnel recombination junction on a-Si:H/HIT tandem structure solar cell," in *Conference Record of the IEEE Photovoltaic Specialists Conference*, 2013.

[52] B. Bills, X. Liao, D. W. Galipeau and Q. H. Fan, "Effect of tunnel recombination junction on crossover between the dark and illuminated current-voltage curves of tandem solar cells," *IEEE Transactions on Electron Devices,* vol. 59, no. 9, pp. 2327-2330, 2012.

[53] A. P. L. E. J. A. S. R. C. C. C. .. &. R. P. Rolland, "Design of a lattice-matched III–V–N/Si photovoltaic tandem cell monolithically integrated on silicon substrate," *Optical and Quantum Electronics,* vol. 46, no. 10, pp. 1397-1403, 2014.

[54] M. L. G. P. S. P. &. B. A. W. Hermle, "Numerical simulation of tunnel diodes for multi-junction solar cells," *Progress in Photovoltaics: Research and Applications,* vol. 16, no. 5, pp. 409-418, 2008.

[55] Synopsys, "Guide, S. D. U., & Version, G.," San Jose, CA, 2008.

[56] O. Isabella and A. Smets, "Auger recombination," in *Solar energy*, Cambridge, UIT Cambridge, 2015, p. 76.

[57] M. T. Janez Krc, Optical Modelling and Simulation of Thin-Film Photovoltaic Devices, CRC Press, 2016.

[58] R. Santbergen, T. Meguro, T. Suezaki, G. Koizumi, K. Yamamoto and M. Zeman, "GenPro4 Optical Model for Solar Cell Simulation and Its Application to Multijunction Solar Cells," *IEEE Journal of Photovoltaics,* vol. 7, no. 3, pp. 919-926, 1 5 2017.

[59] N. E. I. Boukortt and B. Hadri, "Simulation of Electrical Characteristics of PERC Solar Cells," *Journal of Electronic Materials,* vol. 47, no. 10, pp. 5825-5832, 1 10 2018.

[60] Synopsys, "Sentaurus TCAD," [Online]. Available: https://www.synopsys.com/content/dam/synopsys/silicon/datasheets/sentaurus_ds.pdf. [Accessed 29 03 2020].

[61] Synopsys, "Sentaurus Workbench user guide," CA, USA, 2015.

[62] Synopsys, "Sentaurus Structure Editor user guide," CA, USA, 2015.

[63] Synopsys, "Sentaurus Mesh user guide," CA, USA, 2015.

[64] Synopsys, "MatPAr user guide," CA, USA, 2015.

[65] Synopsys, "Sentaurus Visual user guide," CA, USA, 2015.

[66] M. Liu, M. B. Johnston and H. J. Snaith, "Efficient planar heterojunction perovskite solar cells by vapour deposition," *Nature,* vol. 501, no. September 11th, 2013, 2013.

[67] A. Alnuaimi, I. Almansouri and A. Nayfeh, "Effect of mobility and band structure of hole transport layer in planar heterojunction perovskite solar cells using 2D TCAD simulation," *Journal of Computational Electronics,* vol. 15, no. 3, pp. 1110-1118, 1 9 2016.

[68] R. Bakari, R. J. A. Minja and K. N. Njau, "Effect of Glass Thickness on Performance of Flat Plate Solar Collectors for Fruits Drying," *Journal of Energy,* vol. 2014, pp. 1-8, 2014.

[69] A. Badiee, I. A. Ashcroft and R. D. Wildman, "The thermo-mechanical degradation of ethylene vinyl acetate used as a solar panel adhesive and encapsulant," *International Journal of Adhesion and Adhesives,* vol. 68, pp. 212-218, 1 7 2016.

[70] E. L. Warren, M. G. Deceglie, P. Stradins and A. C. Tamboli, "Modeling Three-Terminal III-V/Si Tandem Solar Cells Preprint Modeling three-terminal III-V/Si tandem solar cells".

[71] Z. Wang, C. Chen, K. Wu, H. Chong and H. Ye, *Transparent Conductive Oxides and Their Applications in Near Infrared Plasmonics,* vol. 216, Wiley-VCH Verlag, 2019.

[72] H. A. Dewi, H. Wang, J. Li, M. Thway, F. Lin, A. G. Aberle, N. Mathews, S. Mhaisalkar and A. Bruno, "Four-Terminal Perovskite on Silicon Tandem Solar Cells Optimal Measurement Schemes," *Energy Technology,* vol. 8, no. 4, 1 4 2020.

[73] M. Jaysankar, M. Filipič, B. Zielinski, R. Schmager, W. Song, W. Qiu, U. W. Paetzold, T. Aernouts, M. Debucquoy, R. Gehlhaar and J. Poortmans, "Perovskite-silicon tandem solar modules with optimised light harvesting," *Energy and Environmental Science,* vol. 11, no. 6, pp. 1489-1498, 1 6 2018.

[74] M. Jaysankar, W. Qiu, M. van Eerden, T. Aernouts, R. Gehlhaar, M. Debucquoy, U. W. Paetzold and J. Poortmans, "Four-Terminal Perovskite/Silicon Multijunction Solar Modules," *Advanced Energy Materials,* vol. 7, no. 15, 9 8 2017.

[75] D. Zhang, W. Verhees, M. Dörenkämper, W. Qiu, K. Bakker, A. Gutjahr, S. Veenstra, R. Gehlhaar, U. W. Paetzold, W. Soppe, I. Romijn, L. J. Geerligs, T. Aernouts and A. Weeber, "Combination of Advanced Optical Modelling with Electrical Simulation for Performance Evaluation of Practical 4-terminal Perovskite/c-Si Tandem Modules," in *Energy Procedia*, 2016.

[76] P. Spinelli, F. Lenzmann, A. Weeber and A. Polman, "Effect of EVA encapsulation on antireflection properties of mie nanoscatterers for c-Si solar cells," *IEEE Journal of Photovoltaics,* vol. 5, no. 2, pp. 559-564, 1 3 2015.

[77] Y. Jiang, I. Almansouri, S. Huang, T. Young, Y. Li, Y. Peng, Q. Hou, L. Spiccia, U. Bach, Y. B. Cheng, M. A. Green and A. Ho-Baillie, "Optical analysis of perovskite/silicon tandem solar cells," *Journal of Materials Chemistry C,* vol. 4, no. 24, pp. 5679-5689, 2016.

[78] R. Santbergen, R. Mishima, T. Meguro, M. Hino, H. Uzu, J. Blanker, K. Yamamoto and M. Zeman, "Minimizing optical losses in monolithic perovskite/c-Si tandem solar cells with a flat top cell," *Optics Express,* vol. 24, no. 18, p. A1288, 5 9 2016.

[79] F. Sahli, J. Werner, B. A. Kamino, M. Bräuninger, R. Monnard, B. Paviet-Salomon, L. Barraud, L. Ding, J. J. Diaz Leon, D. Sacchetto, G. Cattaneo, M. Despeisse, M. Boccard, S. Nicolay, Q. Jeangros, B.

Niesen and C. Ballif, "Fully textured monolithic perovskite/silicon tandem solar cells with 25.2% power conversion efficiency," *Nature Materials,* vol. 17, no. 9, pp. 820-826, 1 9 2018.

[80] R. Pandey and R. Chaujar, "Numerical simulations of novel SiGe-based IBC-HJ solar cell for standalone and mechanically stacked tandem applications," *Materials Research Bulletin,* vol. 93, pp. 282-289, 1 9 2017.

[81] W. S. e. a. Yang, "Iodide management in formamidinium-lead-halide–based perovskite layers for efficient solar cells.," *Science,* pp. 1376-1379, 2017.

[82] D. M. K. G. a. T. L. K. Liu, "Effect of CH 3 NH 3 PbI 3 thickness on device efficiency in planar heterojunction perovskite solar cells," *Journal of Materials Chemistry A,* pp. 19873-19881, 2014.

[83] O. Isabella and A. Smets, "Fill Factor," in *Solar Energy*, Cambridge, UIT Cambridge, 2015, p. 113.

[84] A. Smets, k. jager, O. Isabella, R. Van Swaaij and M. Zeman, "Shockley-Read-Hall Recombination," in *solar energy* , UIT Cambridge, 2015, p. 72.

[85] A. smets, K. jager and O. Isabella, "Open circuit voltage," in *Solar energy*, UIT Cambridge, 2015, p. 112.

[86] A. R. R. N. R. &. J. R. Bag, " Effect of absorber layer, hole transport layer thicknesses, and its doping density on the performance of perovskite solar cells by device simulation," *Solar Energy,* vol. 196, pp. 177-182, 2020.

[87] H. e. a. Kim, "Optimization of F-doped SnO 2 electrodes for organic photovoltaic devices," *Applied Physics A,* pp. 521-526, 2008.

[88] M. e. a. Chadel, "Thickness optimization of the ZnO based TCO layer in a CZTSSe solar cell. Evolution of its performance with thickness when external temperature changes," *J. Phys,* p. 879, 2017.

[89] D. e. a. Prochowicz, "Suppressing recombination in perovskite solar cells via surface engineering of TiO2 ETL," *Solar Energy,* vol. 197, pp. 50-57, 2020.

[90] H. e. a. Lu, "Identifying the optimum thickness of electron transport layers for highly efficient perovskite planar solar cells," *Journal of Materials Chemistry A,* Vols. 16445-16452, 2015.

[91] G.-W. D. V. S. a. T. P. Kim, "Thickness of the hole transport layer in perovskite solar cells: performance versus reproducibility," *RSC advances 5,* vol. 120, pp. 99356-99360, 2015.

[92] N. S. Xu, "The physical origin of prebreakdown electron "pin-holes," *High Voltage Vacuum Insulation. Academic Press,* pp. 115-164, 1995.

[93] K. Jager and A. Smets, "Ohmic contacts," in *Solar energy*, Cambridge, UIT Cambridge, 2015, p. 104.

[94] N. e. a. Moulin, "Tunnel junction I (V) characteristics: Review and a new model for pn homojunctions," *Journal of Applied Physics,* vol. 033105, p. 126.3, 2019.

[95] N. A. Lee, G. E. Gilligan and J. Rochford, "Solar Energy Conversion," in *Green Chemistry: An Inclusive Approach*, Elsevier Inc., 2018, pp. 881-918.

[96] K. Hudon, "Solar Energy - Water Heating," in *Future Energy: Improved, Sustainable and Clean Options for our Planet*, Elsevier Inc., 2013, pp. 433-451.

[97] A. Uruena, Advanced Rear-Side Contact Schemes on i-PERC (industrial Passivated Emitter and Rear Cell) solar cells, 2013.

[98] G. E. Eperon, M. T. Hörantner and H. J. Snaith, "Metal halide perovskite tandem and multiple-junction photovoltaics," *Nature Reviews Chemistry,* vol. 1, no. 12, 12 2017.

[99] M. Petrović, V. Chellappan and S. Ramakrishna, *Perovskites: Solar cells & engineering applications - materials and device developments,* vol. 122, Elsevier Ltd, 2015, pp. 678-699.

[100] R. D. S.W.Glunz, " Crystalline Silicon Solar Cells: State-of-the-Art and Future Developments," *Comprehensive renewable energy,* vol. 1, pp. 353-387, 2012.

[101] S. Luxembourg, D. Zhang, Y. Wu, W. Verhees, S. Veenstra and B. Geerligs, "Workshop on Crystalline Silicon Solar Cells and Modules: Materials and Processes Evaluation of bottom cell concepts for perovskite / crystalline silicon tandems".

[102] O. K. Simya, P. Radhakrishnan, A. Ashok, K. Kavitha and R. Althaf, "Engineered nanomaterials for energy applications," in *Handbook of Nanomaterials for Industrial Applications*, Elsevier, 2018, pp. 751-767.

[103] S. Qazi, "Fundamentals of Standalone Photovoltaic Systems," in *Standalone Photovoltaic (PV) Systems for Disaster Relief and Remote Areas*, Elsevier, 2017, pp. 31-82.

[104] D. S. Kim, A. Gabor, A. Upadhyaya, D. S. Kim, A. M. Gabor, V. Yelundur, A. D. Upadhyaya, V. Meemongkolkiat and A. Rohatgi, "String Ribbon silicon solar cells with 17.8 % efficiency STRING RIBBON SILICON SOLAR CELLS WITH 17.8% EFFICIENCY," 2003.

[105] L. Mingzhen, M. B. J. and H. J. S. , "Efficient planar heterojunction perovskite solar cells by vapour deposition," *Nature,* vol. 501, pp. 395-398, 2013.

[106] N. e. a. Rai, "Analysis of various ETL materials for an efficient perovskite solar cell by numerical simulation," *Journal of Materials Science: Materials in Electronics,* pp. 1-12, 2020.

[107] A. Z. K. T. J. K. D. H. R. E. R. B. .. &. O. Y. W. Rohatgi, "26.7% Efficient 4-Terminal Perovskite–Silicon Tandem Solar Cell Composed of a High-Performance Semitransparent Perovskite Cell and a Doped Poly-Si/SiO x Passivating Contact Silicon Cell," *IEEE Journal of Photovoltaics,* vol. 10, no. 2, pp. 417-422, 2020.

[108] L. L. e. a. Yan, "A review on the crystalline silicon bottom cell for monolithic perovskite/silicon tandem solar cells," *Materials Today Nano,* vol. 7, 2019.